A view on possible regime shifts in the North Atlantic subpolar gyre in the mid 1920s and 1990s

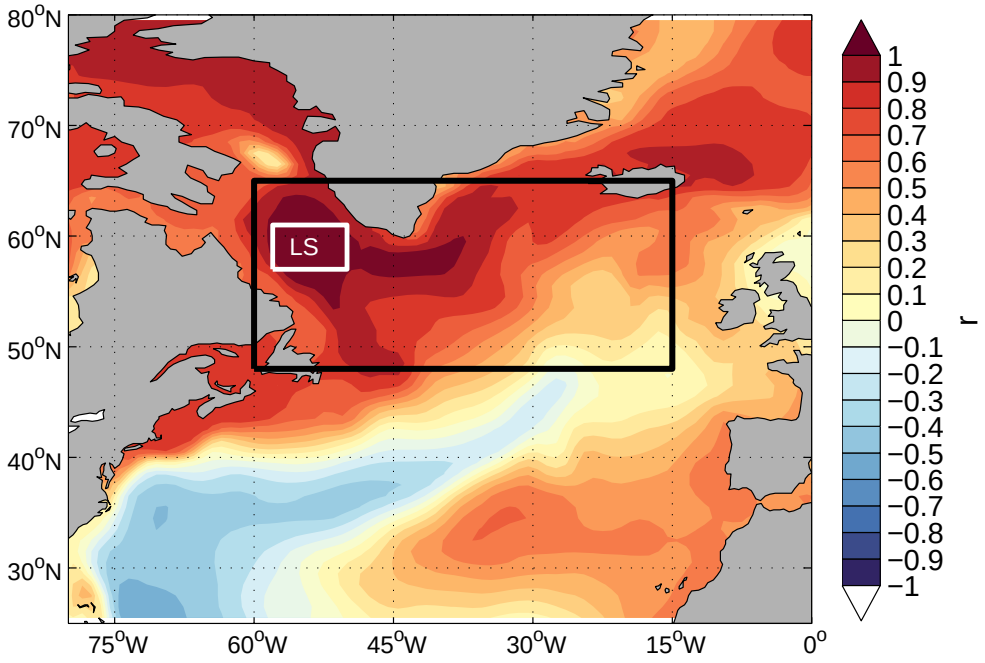

Master's thesis in climate dynamics

Emilie Otilde Lotsberg

October 2014

UNIVERSITY OF BERGEN
GEOPHYSICAL INSTITUTE

Acknowledgements

I want to thank Helge Drange for being an inspiring supervisor guiding me through this master project. Thanks for all help, interesting discussions, encouragement and proofreading. I would also like to thank my co-supervisor, Aleksi Nummelin, for guidance with programming issues as well as proofreading. Thanks to He Yanchun for performing the model simulation, to Mats Bentsen for performing the sensitivity experiments, and to Ingo Bethke for technical guidance. A big thanks to Erlend Elde for creating illustrations to the theory chapter and to Lars Lotsberg for Matlab advices. I also would like to thank Linda Green at Jan Mayen for proofreading and Mads Hvid Ribergaard for providing time series of observed temperature South-West of Greenland. Last but not least, thanks to my fellow students for making the student time memorable and fun.

Abstract

There is strong observational support for two significant warming episodes of the North Atlantic Subpolar Gyre (SPG), one starting in the mid 1920s the other in the mid 1990s. Possible mechanisms responsible for the two warming events are investigated and compared using hind cast simulations with a state-of-the-art global Ocean General Circulation Model (OGCM). The OGCM was forced by an adjusted variant of the Twentieth Century Reanalysis version 2 (20CRv2) for the period 1871–2009. It is found that the preconditioning of the ocean was an essential component for the observed warming and the decline in the SPG circulation in the mid 1920s and the mid 1990s. Both preconditioning phases are characterised by positive North Atlantic Oscillation (NAO) forcing and subsequent enhanced production of intermediate to deep water masses in the SPG region. The latter causes a lagged intensification of the Atlantic Meridional Overturning Circulation (AMOC) and by that, increased poleward transport of warm, saline waters of subtropical origin. In addition, a reduction in the NAO forcing following the mid 1920s and mid 1990s contributed to the warming. The preconditioning of the 1990s warming was stronger than that for the 1920s warming. As a consequence, the shift in the marine climate in the 1990s was more abrupt and stronger than the 1920s counterpart. Sensitivity experiments have been run in order to examine the role of the atmospheric forcing for the two warming events. From and including 1920 and 1990, the ocean was in these cases forced by a constructed atmospheric field dominated by winters with negative NAO forcing. It is found that negative NAO forcing is important for the onset of the warming, but that the ocean preconditioning determines the magnitude of the shift in the ocean climate in the SPG region. The conducted sensitivity experiments suggest that the preconditioning of the ocean prior to 1990 could have been sufficient to initiate a comparable collapse of the gyre as the one in 1995, if nature had presented a negative NAO that year. Obviously, the latter conclusion is based on a single model system and needs confirmation from other models and additional model simulations before a more robust conclusion can be drawn.

Contents

Chapter 1

Introduction

The Atlantic ocean has experienced two periods of rapid warming since the late 19th century (Levitus et al., 2000). The first warming started in the 1920s and is comparable in magnitude with the second and more recent warming occurring in the mid 1990s (Müller et al., 2014). Variations in the climate system in the North Atlantic are linked to changes of a number of coupled sub-systems (Marzeion et al., 2010), for instance the strength and extent of the subpolar gyre (SPG), the North Atlantic Oscillation (NAO; Visbeck et al., 2003; Brauch and Gerdes, 2005), buoyancy forced deep mixing (Lohmann et al., 2008; Yashayaev and Clarke, 2008) and the Atlantic Meridional Overturning Circulation (AMOC; Bentsen et al., 2004; Schmittner et al., 2007). These variations in the North Atlantic climate are considered to be part of the Atlantic Multidecadal Variability (Zhang et al., 2007).

I this thesis, possible mechanisms of the two warming events will be analysed and compared. Special emphasis is put on the SPG region (48°–65° N and from 15°–60° W), due to the far-reached consequences for the climate and ecosystems in the North Atlantic region (Lu et al., 2007). The 1990s warming of the North Atlantic SPG has achieved substantial attention in recent years (e.g. Fu et al., 1999; Häkkinen and Rhines, 2004; Lohmann et al., 2008, 2009). It is therefore of particular interest to study the mechanisms of the 1920s warming, and compare its major features to the more recent warming event.

The North Atlantic SPG is a region of intense interaction between the ocean and the atmosphere (Häkkinen and Rhines, 2004), characterised by a strong, upper-layer cyclonic circulation (Yashayaev and Clarke, 2008). The North Atlantic oscillation (NAO) explains large parts of the atmospheric variability in the North Atlantic-Europe domain (Hurrell, 1995), and several observational and modelling studies relate the variability in the North Atlantic SPG to changes

in the NAO forcing (e.g., Curry and McCartney, 2001; Visbeck et al., 2003; Barrier et al., 2013). Cooling and release of buoyancy associated with positive NAO forcing result in formation of intermediate to deep water masses in the region through intense vertical mixing. This leads to an upward doming structure of the isopycnals towards the center of the gyre and to a strengthening of the gyre circulation itself (Lohmann et al., 2009). These dens and cold water masses formed in the SPG region combine with subsurface water masses of polar origin, forming the southward flowing portion of the AMOC (Bentsen et al., 2004). With a time scale of a few years to a decade, the newly formed water masses in the SPG lead to a spin-up of the AMOC (Lohmann et al., 2008; Robson et al., 2012). Therefore, changes in the SPG will have an impact far beyond the subpolar basins of the North Atlantic, making the region so critical for variations in the Atlantic climate (Lu et al., 2007).

The rapid warming in the North Atlantic starting in the early 1920s and lasting for almost two decades, is considered to initiate the most significant regime shift of the 20th century (Drinkwater, 2006). Observational records of the 1920s show an increase in mean surface air temperature (SAT) of approximately 0.5–1 °C north of 20° N (Brönnimann et al., 2012). The largest changes occurred at high latitudes north of 60° N (Rogers, 1985). During the warmest period (1930–1940), winter temperature anomalies for the area 60°–90° N exceeded 2.2 °C relative to the temperature of the 1910s (Bengtsson et al., 2004). The warming had a broad geographic extent, but the onset of the warming varied geographically (Rogers, 1985). Drinkwater (2006) also states that large and significant changes in the marine ecosystem accompanied the warming. This change included a general northward migration of fish, and it was documented that the Atlantic cod (*Gadus morhua*) spread approximately 1200 km northward along the coast off West Greenland.

During this early 20th century warming, both observations (e.g., Rogers, 1985; Fu et al., 1999) and modelling studies (e.g., Bengtsson et al., 2004; Müller et al., 2014) reveal a remarkable change from relatively cold and fresh to warm and saline North Atlantic water masses. Due to the lack of observational records, a full description of the dynamics of this early warming episode is limited (Polyakov et al., 2005). However, as will be presented below, available observations and modelling studies suggest that the warming is largely associated with atmospheric changes.

By using observational data, Rogers (1985) investigated variations in sea level

pressure and the associated circulation changes that took place before and during the warming event. He states that the warming in the North Atlantic was related to a strengthening of the westerlies, causing increased south-westerly winds and advection of heat over Europe and the Northern North Atlantic. He also argues that the warming in the northwest Atlantic occurred somewhat later than in Europe, due to a shift in the position of the Icelandic low. Bengtsson et al. (2004) used data from a coupled ocean-atmosphere model (ECHAM4/OPYC3; Roeckner and Arpe, 1996) and examined the 1920s temperature change in the Arctic region. They found that the enhanced wind-driven oceanic inflow into the Barents sea and the associated sea ice retreat, accompanied the warming. Müller et al. (2014) used the Max-Planck Institute Ocean General Circulation Model (OGCM) forced with an ensemble of the atmospheric twentieth century (20CR) reanalysis (Compo et al., 2011), and investigated the North Atlantic multi-decadal variability. Müller et al. had a special focus on the 1920s, and argue that from the 1910s, an increased sea level pressure gradient over the North Atlantic strengthened the North Atlantic Current and the SPG circulation. Enhanced winter mixing and a subsequent strengthening of the AMOC lead to a redistribution of subtropical waters into the North Atlantic and Nordic Seas, thus increasing the temperature and salinity during the 1920s. The temperatures in the North Atlantic remained relatively high into the 1940s and 1950s, and was followed by a rapid cooling (Drinkwater, 2006). The decline in temperature started somewhat earlier in the North-East Atlantic than in the more northwestern parts, where warm conditions remained into the 1960s.

The more recent warming event starting in the mid 1990s was accompanied by raised sea level heights (Häkkinen and Rhines, 2004), a retreat of the subpolar front to the west (Brauch and Gerdes, 2005), and increased melting of the Greenland ice sheet (Holland et al., 2008). The North Atlantic SPG warmed significantly, with an SST increase of about 1 °C in just two years (Robson et al., 2012). The 1990s warming event and the associated weakening of the SPG have been related to a prolonged positive phase of the NAO and a sudden drop occurring in the winter of 1995/96 (Häkkinen and Rhines, 2004). From the 1970s until the mid 1990s, a positive trend of the NAO was observed (Hurrell, 1995), consistent with a strengthening of the westerlies and a cooling of the surface waters in the SPG region (Robson et al., 2012).

In the wake of the recent, strong and rapid change of the SPG circulation, several studies have given attention to the response of the SPG to atmospheric

forcing that resembles the NAO pattern. For example, Robson et al. (2012), using both ocean observations and OGCM experiments, investigated if the warming and weakening of the SPG was an instant response of the negative NAO index in 1995/96, or if the warming was a delayed response to the persisting positive NAO forcing prior to the warming. Lohmann et al. (2009) also investigated the impact of the preconditioning of the SPG, using an OGCM driven by the National Centers for Environmental Prediction/National Center for Atmospheric Research (NCEP/NCAR) reanalysis fields. Their analysis indicate that the rapid warming was primarily a result of the prolonged NAO forcing, resulting in a strengthening of the AMOC and enhanced advection of warm and saline waters from the subtropical gyre (STG). They argue that this preconditioning, accompanied by the sudden drop in the NAO index in 1995/96, caused the strong weakening and warming of the gyre. Häkkinen and Rhines (2004) conclude similarly, that the weakening followed winters of intense convection (1989–1994) resulting in a de-stratification of the water column. They also state that local wind-stress changes associated with the NAO could not alone explain the observed weakening. However, studies also suggest that variations in the wind forcing dominates changes in the SPG, especially in the eastern part (e.g. Herbaut and Houssais, 2009; Häkkinen et al., 2011).

Here we investigate and compare the two mentioned warming events based on output from the Bergen version of the Miami Isopycnic Coordinate Ocean Model (MICOM; Bleck et al., 1992). The model is forced by the calibrated atmospheric fields of the *Twentieth Century Reanalysis* product (20CRv2; Yanchun et al., 2014) covering the time period 1871–2009. The reliability of the revised dataset is evidenced through comparison with the *Coordinated Oceanic Reference Experiments* phase-II (COREv2; 1948–2007) for the overlapping period 1948–2009 (Yanchun et al., 2014). To further investigate the importance of the atmospheric forcing during the two events, sensitivity experiments are performed where the ocean is forced by a constructed atmosphere, dominated by NAO^- forcing.

The thesis is organised as follows: In the following chapter, relevant theories of atmospheric forcing mechanisms and the ocean response to these forcings are summarised (Chapter 2). Chapter 3 includes a description of the model and statistical analysis. Chapter 4 presents the results, where particular focus will be given to the atmosphere and the ocean states prior to the mid 1920s and 1990s warming events. The motivation for this is to examine whether the atmospheric states share similarities prior to the two warming events, causing

similarities in the ocean response. In contrast to the preconditioning phases, similarities during the subsequent warming periods can only be expected if the ocean forcing on the atmosphere is sufficiently strong, overrunning the inherent chaotic nature of the atmosphere. In the subsequent chapter, the results are discussed (Chapter 5). In the first part of this chapter, the preconditioning phases will again be in focus. In the second part, the mid 1920s and mid 1990s warming and decline in the SPG circulation are discussed and compared. This part includes model sensitivity experiments to examine the relevance of the atmospheric forcing prior to and during the two warming events. A summary is given in Chapter 6.

Chapter 2

Theory

2.1 The subpolar gyre

The North Atlantic subpolar gyre (SPG) is a region of complex dynamics, playing an important role in the climate variability in the North Atlantic Region and beyond (Bentsen et al., 2004; Tréguier et al., 2005; Hátún et al., 2005). There are intense interactions between ocean and atmosphere (e.g. Talley et al., 2011), resulting in excessive formation of intermediate and deep waters during winter (see Section 2.3.7). The cold and dense water masses produced in the region will combine with overflow waters of polar origin, constituting the southward branch of the Atlantic meridional overturning circulation (AMOC; see Section 2.3.8). The gyre circulates cyclonically between approximately 50°–65° N (Häkkinen and Rhines, 2004), and it is surrounded by vigorous boundary currents. Because of the low temperature compared to the neighboring relatively warm North Atlantic subtropical gyre (STG), it's climatological sea surface height (SSH) is the lowest on the Northern Hemisphere (Marshall and Plumb, 2008).

Variations in the strength of the gyre is governed by anomalous wind stress patterns associated with the NAO (Bellucci et al., 2008), as well as the ocean state itself (Lohmann et al., 2009). Positive (negative) NAO forcing (see Section 2.2.2) results in an anti-cyclonic (cyclonic) wind stress curl anomaly at mid-latitudes, causing an anti-cyclonic (cyclonic) circulation anomaly in the SPG. This will ultimately lead to a gyre equilibrium response, which can be explained by Sverdrup dynamics (see Section 2.3.5).

The subpolar gyre index, commonly derived from analysis of the sea surface height (SSH), can be used as an indicator of the intensity of the subpolar North

Atlantic cyclonic circulation (Häkkinen and Rhines, 2004). Low values of the index, consistent with anomalous low SSH, indicates a strong gyre and vice versa. The index also acts as a potential indicator of variations in the strength of the AMOC, the latter with a few years delay compared to variations in the SPG index (Gao and Yu, 2008; Lohmann et al., 2009, see Section 2.3.8). An alternative index for the gyre circulation strength is the barotropic streamfunction (BSF; ψ, unit is Sverdrup, where 1 Sv = 10^6 m^3 s^{-1}) of the vertically integrated transport. Large negative values of this index is consistent with a strong gyre.

As already mentioned, changes in the hydrography and circulation dynamics in the SPG region is tightly linked to changes in the atmospheric forcing. In the following sections, theories of the atmospheric forcing mechanisms influencing the gyre will be presented (Section 2.2), followed by the response of the ocean (Section 2.3).

2.2 Atmospheric forcing

2.2.1 Geostrophic flow

The large-scale motion in the free atmosphere and ocean are close to balance in the horizontal plane, where the Coriolis force is balanced by horizontal pressure gradients (Marshall and Plumb, 2008). This is known as geostrophic balance or geostrophic flow:

$$f\hat{\mathbf{z}} \times \mathbf{u} + \frac{1}{\rho}\nabla p = 0 \tag{2.1}$$

The first term in Equation 2.1 represents the Coriolis force per unit mass and the second term is the pressure gradient force per unit mass. The Coriolis parameter $f = 2\Omega \sin\phi$, where Ω (s^{-1}) is the Earth's rotation rate and φ (rad) is latitude. $\hat{\mathbf{z}}$ is the vertical unit vector, $\mathbf{u}$ (m s^{-1}) is velocity, ρ (kg m^{-3}) is density, and p (Pa) is pressure. This balance is satisfied in flows with a low Rossby number; i.e., $R_0 = \frac{\mathcal{U}}{f\mathcal{L}} \ll 1$, where $\mathcal{U}$ is a typical velocity and $\mathcal{L}$ is a characteristic length scale for the flow. Equation 2.1 gives the geostrophic velocity $\mathbf{u}_g$ with eastward (u_g) and northward (v_g) velocity components given by:

$$(u_g, v_g) = \left(-\frac{1}{f\rho}\frac{\partial p}{\partial y}, \frac{1}{f\rho}\frac{\partial p}{\partial x}\right) \tag{2.2}$$

2.2.2 The North Atlantic Oscillation

On inter-annual to decadal timescales, the North Atlantic Oscillation (NAO) is the dominant mode of atmospheric variability over the North Atlantic (Hurrell, 1995). The NAO was first identified by Sir Gilbert Walker in the 1920's, who analysed the spatial patterns of seasonal weather and identified a surface pressure correlation pattern withing the Atlantic sector (Walker, 1924; Walker and Bliss, 1932). The corresponding NAO index is defined by Hurrell (1995) as the normalised mean winter (December to March) sea level pressure (SLP) difference between Lisbon, Portugal and Stykkisholmur, Iceland. Several other definitions of the NAO index exist, all being essentially equivalent (Greatbatch, 2000). As the NAO is less dominant during warmer seasons (Rogers, 1990), most attention has been given to the winter NAO.

During a positive phase of the NAO, the typical situation is that the Icelandic (polar) low is anomalously low and usually, but not always, the Azores (subtropical) high is anomalously high (Visbeck et al., 2003). Irrespective of the actual configuration, winters with high NAO index are associated with stronger than normal westerly winds at mid, northern latitudes. These winters are therefore characterised by colder than normal conditions in the eastern Canadian Arctic and warmer than normal conditions over the Eurasian continent (Hurrell, 1995). The SPG region experiences therefore cooling in years with positive NAO forcing. The strength of the easterly surface winds in the Atlantic trade wind belt are also typically enhanced during positive NAO winters (Visbeck et al., 2003). Years dominated by positive NAO forcing, will hereafter be referred to as NAO^{+} years. The negative NAO phase reflects an opposite pattern of sea level difference between Iceland and the Azores. In this case the westerlies and trade winds are weaker than normal, often in combination with a southward shift in the position of the westerlies. This situation is referred to as NAO^{-} years in the following. Hurrell (1996) showed that the NAO alone can account for 31% of the winter surface temperature variance over the Northern Hemisphere (north of 20° N), indicating the importance of NAO variability.

2.2.3 Heat flux

Variations in the NAO index and the associated changes in the wind fields, will lead to strong variations in the air-sea fluxes of, in particular, heat and momentum (Visbeck et al., 2003). The heat flux is divided into four components: The net short wave and the net long wave radiation, and the sensible

and latent turbulent heat fluxes. As explained in Visbeck et al. (2003), the short wave radiation variability depends on the cloud cover and changes in the sea-ice albedo. Variations in the long wave radiation is associated with temperature changes in the lower atmosphere, as well as cloudiness and the sea surface temperature (SST). Sensible and latent heat flux anomalies result from temperature/water vapor pressure gradients between the sea surface and the lower atmosphere, and are both largely dependent on the surface wind speed. In the SPG, sensible heat loss is the largest flux anomaly, closely followed by evaporative heat loss.

2.3 Ocean response

2.3.1 Near-surface geostrophic flow

Free, large-scale flow is governed by the same dynamics in the ocean and the atmosphere (Marshall and Plumb, 2008). Fluids in motion tend to be in equilibrium, the large-scale flows in the ocean is therefore often geostrophic, or nearly so (Brown et al., 2001).

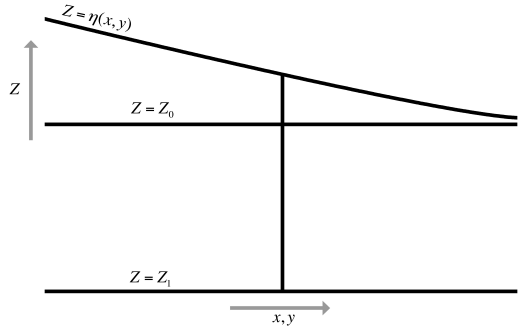

Figure 2.1: Illustration of the heigth of the free surface of the ocean, $z = \eta(x, y)$. The depths of two horizontal reference surfaces are given by $z = z_0$ and $z = z_1$. Figure is based on Marshall and Plumb (2008), p. 183.

For the surface currents to be in geostrophic balance, a pressure gradient force must balance the Coriolis force. For example, in the north-eastward flowing Gulf Stream, a south-eastward directed Coriolis force acts on the current, balanced by a north-westward oriented pressure gradient force. The latter force arises from the surface tilt (η) of the free surface, being higher towards south-east (STG region) than north-west (SPG region). Assuming the density to be constant ($\rho = \rho_{\text{ref}}$), the geostrophic flow just beneath the surface is

$$\mathbf{u}_g = \frac{g}{f}\hat{\mathbf{z}} \times \nabla\eta, \tag{2.3}$$

where horizontal components of the near-surface pressure gradient is replaced by gradients in surface elevation (see Figure 2.1).

2.3.2 The Taylor-Proudman theorem

For geostrophic flow on an f-plane ($f = f_0$) with constant density ρ_0, the flow is two-dimensional (barotropic) and the vertical derivative of the horizontal velocity components vanish. This relationship is known as the Taylor-Proudman theorem (Marshall and Plumb, 2008). The Taylor-Proudman theorem can be shown by taking the z derivative of Equation 2.2, and using the continuity equation for incompressible fluids $\left(\frac{\partial u}{\partial x} + \frac{\partial v}{\partial y} + \frac{\partial w}{\partial z} = 0\right)$, yielding:

$$\frac{\partial u}{\partial z} = \frac{\partial v}{\partial z} = 0 \tag{2.4}$$

A consequence of this relationship is obtained by eliminating the pressure terms from Equation 2.2, by summing $\frac{\partial u}{\partial x} + \frac{\partial v}{\partial y}$, and inserting $f = f_0$, thus: $\frac{\partial u}{\partial x} + \frac{\partial v}{\partial y} = 0$. Using the continuity equation again, it follows that:

$$\frac{\partial w}{\partial z} = 0 \tag{2.5}$$

Since $w = 0$ at the sea surface/bottom, there can be no vertical velocity on an f-plane. This puts large constraints on the flow: Vertical columns of fluid has to remain vertical, or, on a rotating sphere, fluid columns have to remain aligned in the direction of the rotation axis. Irrespective of the configuration, rotation greatly stiffens the flow. The resulting columns — that can be readily demonstrated on a rotating table — are named *Taylor columns* (after the British physicist and mathematician Sir Geoffrey Ingram Taylor, 1886–1975).

2.3.3 Ekman theory

Ekman Transport

The large-scale surface wind stress field drives the ocean circulation (Visbeck et al., 2003). Surface wind stress causes an immediate response at the ocean surface, which is communicated downwards within a near-surface layer of the ocean known as the *Ekman Layer* (named after the Sweedish oceanographer Vagn Walfrid Ekman, 1874–1954). As a consequence of the Coriolis effect, a spiral occurs in the Ekman layer (Figure 2.2). The surface layer move by

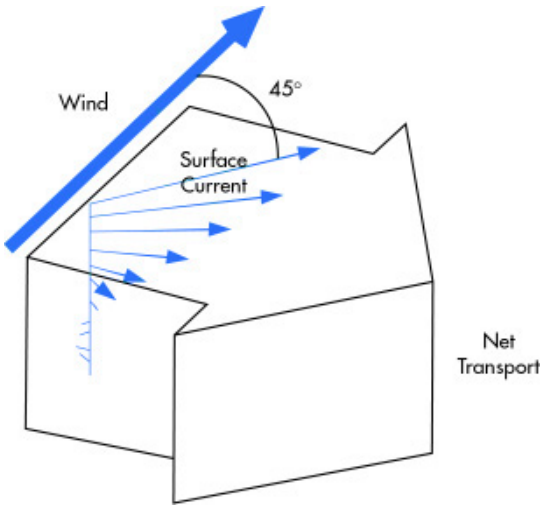

Figure 2.2: Illustration of the Ekman spiral. Each successive layer in a water column move more slowly than the layer above, and is deflected by the Coriolis effect. This causes a spiral to form in the Ekman layer, and the net Ekman transport is directed 90° to the right (on the Northern Hemisphere; to the left on the Southern Hemisphere)

the friction force of the wind stress, dragging deeper layers of water below. Each successive layer moves slower than the layer above and is deflected by the Coriolis effect (to the right in the Northern Hemisphere and to the left in the Southern Hemisphere). These effects create an *Ekman spiral*, where the net water transport (Ekman transport) in this layer is directed exactly 90° to the right (Figure 2.2) of the wind stress (on the Northern Hemisphere).

Since this Ekman transport adjusts on a short time scale (several days), it will be in phase with the NAO forcing (Visbeck et al., 2003). As illustrated in Figure 2.3, a positive phase of the NAO with anomalously strong westerlies and trade winds (black arrows), causes anomalous meridional Ekman transport (blue arrows), leading to a fast dipolar circulation anomaly pattern (Eden and Willebrand, 2001). Strong westerly winds result in southward Ekman transport anomalies in the $\sim$ 30°–60° N latitudinal band, while a northward transport is generated to the south, the latter caused by the strengthening of the trade winds. This rapid communication with the deeper layers in the ocean results in a fast Ekman induced contribution to the AMOC (Section 2.3.8), with maximum flow below the Ekman layer depth (at $\sim$ 300 m; Visbeck et al., 2003). The convergence at $\sim$30° N causes a weakening of the AMOC north of $\sim$30° N and a strengthening to the south (Barrier et al., 2013; Visbeck et al., 2003).

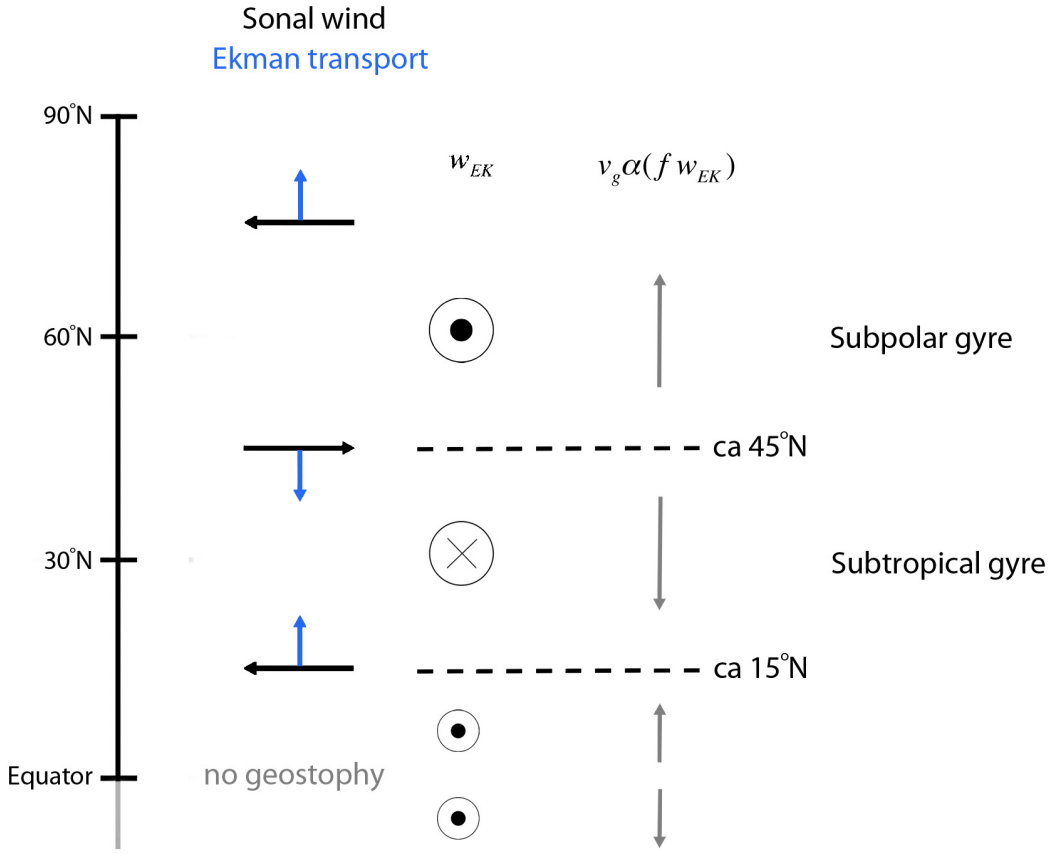

Figure 2.3: Schematic overview of the North Atlantic Ocean, where the zonal wind stress (black arrows) causes Ekman transport (blue arrows) perpendicular (to the right) to the wind stress. This leads to divergence in the SPG and convergence in the STG, resulting in vertical Ekman lifting and pumping, respectively. The direction of these Ekman-induced velocities, (w_{EK}), are indicated in the figure. Because of the stiffness of the Taylor columns, the Ekman pumping drives a sub-surface meridional flow (Equation 2.9) towards north (south) in the SPG (STG) as indicated by the grey arrows.

Ekman Pumping

Convergence and divergence must be balanced by a vertical flow at the bottom of the surface boundary layer, causing downwelling in the area of the STG and upwelling in the SPG (Figure 2.3 and 2.4). This process of vertical movement, generating flow into and out of the Ekman layer, is known as Ekman pumping (Tomczak and Godfrey, 2001). As illustrated in Figure 2.4, a positive phase of the NAO will lower the isopycnals in the STG region and raise the isopycnals in the SPG region. Enhanced sloping structure of the isopycnals in the SPG/STG region, causes a strengthening of the respective gyre circulations (Lohmann et al., 2008).

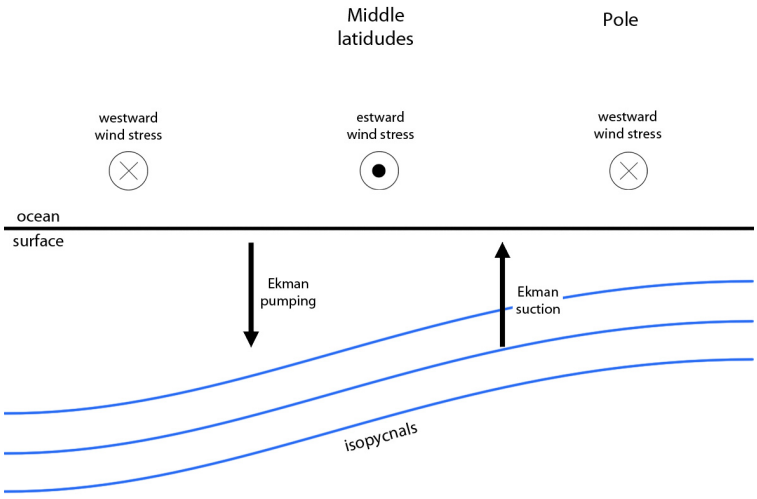

Figure 2.4: Illustration of the mechanism maintaining a large-scale sub-surface horizontal density gradient in the mid-latitude ocean. Ekman pumping/lifting causes the isopycnals (blue lines) to be raised in the SPG region and lowered in the STG region. The direction of the wind stress is indicated. Figure is based on Marshall and Plumb (2008) p. 219.

An expression for the Ekman pumping can be obtained by vertically integrating the continuity equation over the Ekman layer of thickness $-\delta$ (m) (Marshall and Plumb, 2008). Assuming that the geostrophic flow is non-divergent, the continuity equation can be written:

$$\Delta_h \cdot \mathbf{u}_{ag} + \frac{\partial w}{\partial z} = 0 \tag{2.6}$$

where $\mathbf{u}_{ag}$ is the agiostrophic component of the flow. Noting that $w = 0$ at the surface, the magnitude of the vertical velocity at the bottom of the Ekman layer (w_{EK}) can be found:

$$w_{EK} = \frac{1}{\rho_{ref}} \Delta_h \cdot \mathbf{M}_{Ek} = \frac{1}{\rho_{ref}} \hat{\mathbf{z}} \cdot \Delta \times \left(\frac{\tau_{\text{wind}}}{f} \right) \tag{2.7}$$

Here, Δ_h is the horizontal gradient, $\mathbf{M}_{EK}$ is the mass transport over the Ekman layer: $\mathbf{M}_{Ek} = \int_{-\delta}^{0} \rho_{ref} \mathbf{u}_{ag}\, dz$, and τ_{wind} (N m^{-2}) is the surface wind stress vector.

w_{EK} can now be written:

$$w_{EK} = \frac{1}{\rho_{ref}} \left(\frac{\partial}{\partial x} \frac{\tau_{\text{wind } y}}{f} - \frac{\partial}{\partial y} \frac{\tau_{\text{wind } x}}{f} \right). \tag{2.8}$$

Note that typically τ_{wind} varies much more than f (Marshall and Plumb, 2008), and the pattern of w_{EK} is mostly dependent on variations in τ_{wind}. Therefore, f is kept as a constant in the calculations in Chapter 4.

2.3.4 Interior ocean circulation

The ocean is in geostrophic balance beneath the Ekman layer (Marshall and Plumb, 2008). From the Taylor-Proudman theorem (within the limits of the underlying assumptions), the flow is mainly two-dimensional. However, Ekman transport causes convergence/divergence leading to the development of a vertical flow. On the planetary scale, variations in f cannot be ignored. To allow for a water column to stretch or compress, f must vary with latitude: $f = f_0 + \beta f$. Now, summing up $\frac{\partial u}{\partial x} + \frac{\partial v}{\partial y}$, and using $\beta y \ll f_0$, it is found that

$$f_0 \frac{\partial w_g}{\partial z} = \beta v_g, \tag{2.9}$$

which relates the horizontal and vertical velocities (the subscript g is used to emphasize that this applies to geostrophic flow). Thus, vertical gradients in the flow are allowed to develop in the presence of variations in the Coriolis force with latitude. If the Ekman pumping velocities (w_{EK}) are assumed to be much larger than vertical velocities in the abyss, Equation 2.9 implies that in regions of upwelling (SPG region: $W_{Ek} > 0$), there will be a northward flow, and in regions of downwelling (STG: $W_{Ek} < 0$), a southward flow. This is how the wind, through the convergent and divergent Ekman transports, drives the interior ocean circulation (Marshall and Plumb, 2008). The resulting meridional flow as a consequence of stretching/compression of water columns are illustrated with grey arrows in Figure 2.3. Thorough derivations of Equation 2.4–2.9 are found in Stewart (2004).

2.3.5 Sverdrup theory and the Gulf Stream

Ekman explained, by assuming that the ocean was unlimited, that the net flow in the Ekman layer is perpendicular to the wind stress. Harald Ulrik Sverdrup (1888–1957) also investigated the relationship between wind and ocean circulation, and his aim was to determine how currents respond to both wind stress and pressure gradient forces. He showed that the net meridional transport by a given wind stress is determined by the curl of the wind stress and the change of f with latitude (Brown et al., 2001). Therefore, in areas of weak wind stress curl (∼45° and 15° N in Figure 2.3), the flow will be almost entirely zonal, whereas in areas of larger wind stress curl (∼30° N) the southward motion will be greatest.

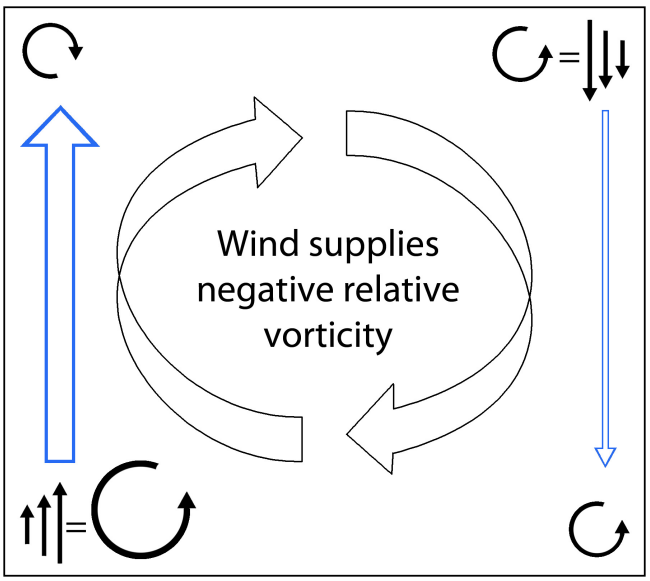

Figure 2.5: Representation of the various vorticity contributions in the STG with an intensified western boundary current. A vorticity balance is attained, so that the gyre rotation does not accelerate.

Sverdrup could not, however, include a western boundary in his calculations, and his theory could therefore not explain the existence of a strong western boundary current like the Gulf Stream (Brown et al., 2001). This was solved by Henry Stommel (1920–1992), who included friction in his calculations (Stommel, 1948). He discovered intense western boundary currents as a result of variations in the Coriolis parameter with latitude. He also showed this in the sense of vorticity balance (Figure 2.5). By assuming that the depth of the flow is constant and that the wind supplies negative (clockwise) relative vorticity ($\zeta = \frac{\delta v}{\delta x} - \frac{\delta u}{\delta y} < 0$), a strong western boundary current is necessary to avoid an acceleration of the negative vorticity. As illustrated in Figure 2.5, flow moving

southward on the eastern boundary will move into regions of lower positive planetary vorticity (f) and will thus gain positive relative vorticity (or lose negative relative vorticity). Friction with the boundary also leads to a gain in positive relative vorticity, which will nearly balance the negative relative vorticity supplied by the wind stress. On the western side, however, currents flowing northward will gain negative relative vorticity which adds to the negative relative vorticity supplied by the wind. To avoid acceleration, the flow must be sufficiently strong and narrow in order for the friction to cause a large gain in positive relative vorticity balancing the large gain in negative relative vorticity.

2.3.6 Thermal and haline contribution to steric height

The density of sea water varies rather little, only by a few percent, but these variations are essential to the ocean dynamics (Marshall and Plumb, 2008). The density depends on temperature T, salinity S and pressure p (in a nonlinear way). Increased temperatures will decrease the density, whereas increased salinity will increase the density. Seawater is almost incompressible, but in the interior ocean, compressibility effects are not always negligible. For the typical temperature and salinity range found in the ocean (0–30 °C and 33–36 psu), temperature is typically influencing the density more than the salinity (Marshall and Plumb, 2008).

The dependence of density by temperature and salinity can be approximated by a simplified equation of state (Equation 2.10), giving the steric contribution to a change in density:

$$\delta\rho \approx \rho_{ref}(-\alpha_T[T - T_0] + \beta_S[S - S_0]), \tag{2.10}$$

Here $\delta\rho$ is the density change and T_0 and S_0 are reference values for temperature and salinity, respectively. Furthermore, ρ_{ref} is a reference density with a typical value of $\sim$ 1024 $kg\ m^{-3}$ and α_T (K^{-1}) is the thermal expansion coefficient of water defined by $\alpha_T = -\frac{1}{\rho_{\text{ref}}}\frac{\partial\rho}{\partial T}$ (with S and p kept constant). A typical value of α_T is $1 \times 10^{-4}C^{-1}$, with increasing values for increasing temperatures. The density change by salinity is dependent on β_S (psu^{-1}) defined by $\beta_S = \frac{1}{\rho_{ref}}\frac{\partial\rho}{\partial S}$. This coefficient varies rather little, and has a value close to $7.6 \times 10^{-4}psu^{-1}$.

By using conservation of mass (Equation 2.11), the change in density can be used to calculate an approximate value of the change in sea surface height δh (m):

$$A_0\,\rho_0\,h_0 = A_0(\rho_0 + \delta\rho)(h_0 + \delta h) \tag{2.11}$$

Here A_0 (m^2) is the horizontal area of the volume, and ρ_0 and h_0 are the density and height of the volume, respectively, before the change. Thus, the left hand side represents the mass M_0 (kg) of a volume before the change, and the right hand side equals the mass (M_1) after the change.

The net expansion and contraction of a water column due to variations in T and S, are called the steric effect or the steric height. To investigate the thermal contribution to a change in the steric height, only the first term in Equation 2.10 is included. This is the thermosteric effect. The haline contribution is obtained by including only the second term in Equation 2.10, the halosteric effect.

2.3.7 Formation of intermediate and deep water masses

The subpolar portion of the North Atlantic Ocean is the region where warm, saline waters from the tropical and subtropical areas meet the cold and less-saline outflows and overflows from the high, polar latitudes. These water masses interact and, with the surface buoyancy forcing induced by the atmospheric state, the major intermediate and deep water masses of the North Atlantic are created in winter(Yashayaev and Clarke, 2008). The SPG's circulation carries the initially warm, salty surface and subsurface waters counterclockwise around the northern and western boundaries of the deep basins of the SPG (the Iceland Basin, the Irminger Sea, and the Labrador Sea). Before entering the Labrador Sea in west, it experiences a net annual heat loss and freshening which may result in deep convectively mixed layers extending to depths of 2 km and more (Yashayaev and Clarke, 2008).

Labrador Sea winter mixing

As stated by Visbeck et al. (2003), the Labrador Sea (LS) is a key location for the North Atlantic climate system. Variations in the production rate of convectively formed Labrador Sea Water (LSW) directly determine the rate of the SPG circulation, which again is a driving component of the AMOC (Section 2.3.8). The LS is the coldest and freshest basin of the North Atlantic (Yashayaev and Clarke, 2008), and winter cooling in the region produces LSW.

Three conditions can explain why the LS is favourable for deep convection (Yashayaev and Clarke, 2008): First, the water entering the LS comes from the Irminger Sea (IS) where it has already been cooled and made denser. The second condition is the strong cyclonic circulation in the LS, causing Ekman-induced upwelling of mid-depth waters in the interior of the LS. The density difference between the surface and the LSW layer will therefore be reduced, favouring mixing to great depths. The third condition is outbreaks of air masses from the Arctic and the North American continent over the western LS, leading to an intense cooling of the ocean surface waters, further reducing the surface buoyancy and increasing the water mass density. The surface waters then become dense enough to convectively mix to intermediate depths (1500–2200m).

As further explained in Yashayaev and Clarke (2008), deep mixing relates to the NAO state. Periods of sustained, high positive NAO will, in the LS, result in anomalously cold northwesterly winds and intense ocean heat loss, leading to strong and deep vertical mixing. Years dominated by negative NAO index values are characterised by reduced heat loss, leading to reduced formation of LSW. But, as argued by Yashayaev and Clarke (2008), it may take several cold winters to overcome stable density conditions established after a period without convection, whereas a moderately cold winter might be enough to trigger deep mixing if it follows a period of stormy winters. The LS may also be influenced by local wind field anomalies, and is not always directly linked to the strength of the westerlies.

2.3.8 The Atlantic Meridional Overturning Circulation

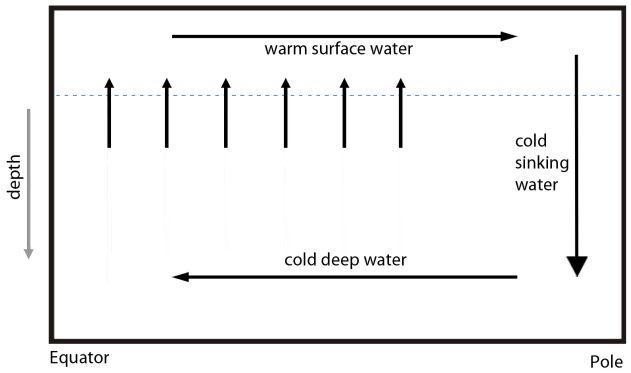

Figure 2.6: Simple model of the AMOC system. Arrows indicate the currents; the warm surface waters flowing poleward, the sinking of dens water in the subpolar region, and the southward flowing deep branch of the AMOC. Figure is based on Marshall and Plumb (2008) p. 253.

The AMOC is a major current system characterised by a northward flow of warm, relatively saline surface waters originating from the tropical-subropical region, and a southward flow of colder, dense waters in the deep Atlantic (Balmaseda et al., 2007). Figure 2.6 is a simple illustration of this flow system and Figure 4.20 illustrates the current system in a topographic map of the Nordic Seas and subpolar basins. Solid arrows in the latter figure represent surface currents, whereas dashed arrows illustrate the deep currents.

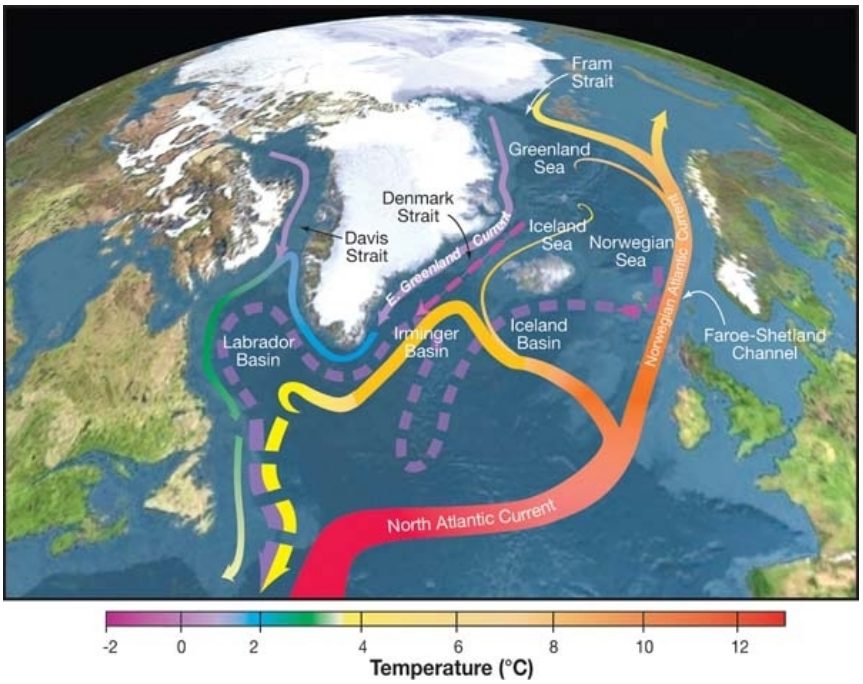

Figure 2.7: Topographic map of the North Atlantic, the Nordic Seas and subpolar basins, illustrating the northern branch of the AMOC. Solid arrows indicate the surface currents and dashed lines illustrate the location of the deep currents. The color of the lines indicate the temperature of the water masses. The figure is provided from http://www.eoearth.org/view/article/150290/

The AMOC plays an important role in regulating the Earth's climate (Cheng et al., 2013). The upper layer currents transport a significant amount of heat from the tropics and Southern Hemisphere toward the northern North Atlantic, contributing to the mild climate predominant in northwestern Europe (Balmaseda et al., 2007). Poleward of 25° N, the AMOC carries up to 20–30% of the global atmosphere–ocean heat transport in the Northern Hemisphere (Bentsen et al., 2004). Variations in the AMOC are highly correlated with variations of intermediate and deep water masses in the SPG (Balmaseda et al., 2007). Enhanced surface mixing will, generally, cause a spin-up of the AMOC (Lohmann et al., 2008).

2.4 Empirical Orthogonal Functions

Climate variations are the result of complex, nonlinear interactions between numerous degrees of freedom or modes, and is characterised by high dimensionality (Hannachi, 2004). It is therefore challenging to extract the governing patterns consistent with the main variations in observed or simulated fields. Empirical Orthogonal Functions (EOFs) is a statistical technique used to identify leading spatial patterns from any temporally and spatially varying quantity. The time series associated with the spatial EOF pattern is called the Principal Component (PC, see Section 3.2.1). Originally, EOF analysis was used to reduce the number of variables in large datasets, maintaining the majority of the explained variance in the full data set (Hannachi, 2004). Later, as shown by Thompson and Wallace (1998), EOFs have been used as a tool to extract and investigate physical modes, such as the NAO and the Arctic Oscillation (AO). Section 3.2.1 provides methodology of performing EOF analysis.

It should be noted that in interpreting the EOFs, empirical modes do not necessarily correspond to true dynamical modes with physical behaviour (Emery and Thomson, 2001). For example, one physical process may be spread over more than one EOF, or several physical processes can be captured in only one EOF pattern. Additionally, the different EOF modes are always orthogonal, which is not always true for physical modes (Simmons et al., 1983). The EOFs should therefore always be analysed together with its respective PC time series, in addition to being paired with theoretical knowledge (i.e., physical interpretation) and, ideally, additional scientific analysis methods.

Chapter 3

Methods

3.1 The ocean model

The model used in this study is the ocean component of the Norwegian Earth System Model (NorESM; Bentsen et al., 2013; Iversen et al., 2013). The OGCM originates from the Miami Isopycnic Coordinate Ocean Model (MICOM; Bleck et al., 1992), but is extensively modified by Mats Bentsen at Uni-Research, Bergen (Bentsen et al., 2013; Danabasoglu et al., 2014*a*). The ocean model is coupled to the Los Alamos Sea Ice Model version 4 (CICE4; Hunke and Lipscomb, 2008; Holland et al., 2012).

The scalar quantities in the model is integrated forward in time by means of the leapfrog scheme (Shampine, 2009), whereas the forward-backward time stepping is used for the baroclinic and the barotropic mode. The leapfrog scheme is a second order accurate scheme, centred in time and space (illustrated in Figure 3.1). An advantage of this scheme is that there is no amplitude dissipation if it is Courant stable, that is, the *Courant-Friedrichs-Lewy* (CFL) condition is satisfied (Equation 3.1):

$$C = v\frac{\Delta t}{\Delta x} \leq 1 \tag{3.1}$$

C is the dimensionles CFL number. It depends on the size of the grid cell Δx (m), the magnitude of the advection velocity of the models variables v (m s^{-1}) and the time step Δt (s). When solving for the advection term, this is a necessary condition for stability and it provides a limit for the maximum allowed time step for a given spatial resolution: $\Delta t \leq \Delta x/|v|$. A disadvantage of the leapfrog scheme is that it has one computational (false or parasitic) mode in addition to the physical (correct) mode. The first represents a model error that decouple odd and even time steps with, typically, increasing amplitudes,

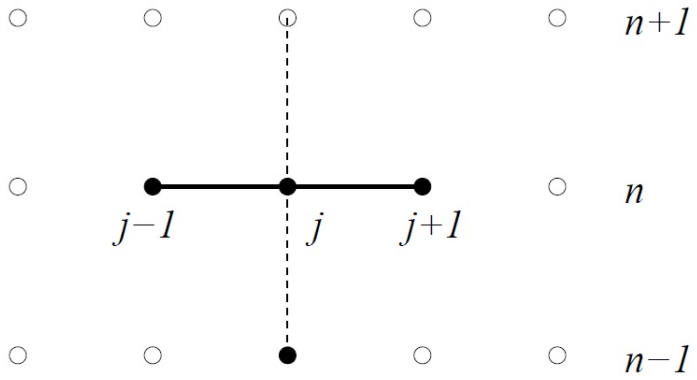

Figure 3.1: Illustration of the Leapfrog scheme, centered in time and space. n is the time index ($t = n\Delta t$) and j is the spacial index ($x = j\Delta x$).

requiring filtering at each time step to be kept under control. The effect of the time integration filtering is a weak smoothing of the advected quantity.

3.1.1 Horizontal resolution

The model version used in this study has an intermediate resolution of nominal 1° for the ocean and ice components (Yanchun et al., 2014). In the meridional direction in the tropics (between 20° N–20° S), the grids are enhanced in the meridional direction (Yanchun et al., 2014), yielding a total of 385 × 360 grid cells (latitude-by-longitude) covering the globe. The grid is tripolar (two Northern Hemisphere grid singularities) and is adapted for NorESM from a standard grid (tx1v1) of CCSM4 (Yanchun et al., 2014). To avoid numerical problems/divergence in the ocean areas, these Northern Hemisphere singularities are placed over North America and the Eurasia continents. Due to the spherical grid, the longitudinal resolution (Δx) decreases when approaching these singularities.

The model variables are staggered in space, adopting an Arakawa C grid configuration (Figure 3.2). Different variables are defined at different points, giving various advantages, i.e. the pressure gradient force and mass convergence and divergence terms can be calculated without averaging. As illustrated in Figure 3.2, the velocity components in the x- and y-directions, u and v, are located at different points in the grid cell. Scalar values (here marked as p) are located in the centre of the cell, whereas vectors are placed at the q-position. dx and dy denote the east-west and north-south grid spacing, respectively.

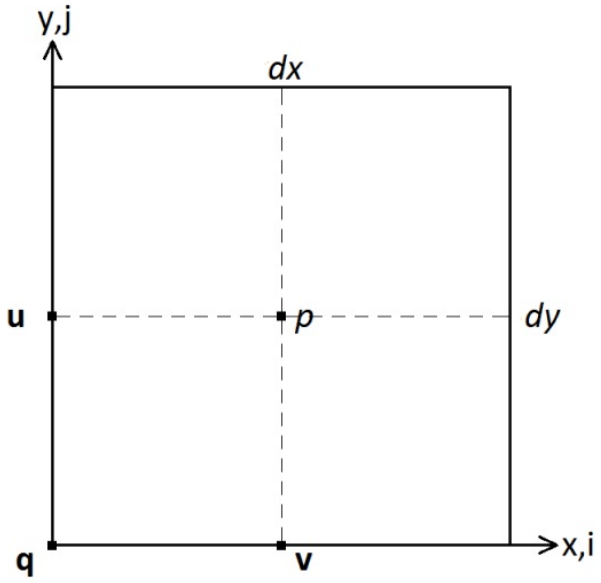

Figure 3.2: Illustration of the staggered Arakawa C-grid. dx and dy denote the east-west and north-south grid spacing, respectively, p represent scalar values, and **q** refers to vectors. **u** and **v** are the velocities in x- and y-direction, respectively.

3.1.2 Vertical resolution

The ocean component in NorESM is based on isopycnic coordinates in the vertical. Isopycnic coordinate OGCMs seek to eliminate numerical errors in the vertical direction by replacing the traditional representation of depth z by isopycnic levels or levels of constant (prescribed) potential density (Chassignet et al., 1996). A total of 53 model layers are used; an uppermost mixed layer and 52 isopycnic layers underneath, with reference potential densities relative to 2000 dbar (about 2000 m) in the range 28.202–37.800 kg m^{-3} (Bentsen et al., 2013). The potential density (σ_θ, kg m^{-3}) of a water parcel is the density the parcel would have if it was adiabatically raised or lowered to a reference pressure P_0 (Pa). It is also dependent on the salinity and temperature of the parcel:

$$\sigma_\theta = \rho_\theta(P_0, T, S) - 1000, \tag{3.2}$$

where P_0 is the reference pressure, T (K) is the temperature and S (psu) is the salinity.

In turbulent stratified fluids influenced by buoyancy effects, mixing will primarily take place along isopycnic surfaces (Schiller and Brassington, 2011). Thus, the motivation for using potential density as the vertical coordinate is,

as argued by Chassignet et al. (1996), to reduce numerically induced diapycnal mixing that may overshadow the diapycnal processes that occur in nature. The dynamic equations are discretized on an x, y, σ_2 model grid, where σ_2 is the potential density relative to 2000 dbar. Transport in the horizontal x-, y-direction then takes place on isopycnic surfaces, and the associated numerical diffusion has no diapycnal component.

The original set-up of MICOM adopted potential density with a reference pressure of 0 dbar, but the definition may deteriorate the density structure at intermediate and great depths, particularly in cold waters (Assmann et al., 2010). When potential density is referred to a reference pressure of about 2000–4000 dbar, it satisfactorily represent the density stratification in deep water (Lynn, 1971) with, in general, limited deterioration of the surface density structure. Therefore, the NorESM ocean component uses a reference pressure of 2000 dbar. Potential density with a 2000 dbar reference pressure is now widely used as the vertical coordinate in isopycnal ocean models (Assmann et al., 2010).

3.1.3 Spin up

Initially, the ocean model starts with prescribed, vanishing velocities, and the temperature and salinity fields are taken from the January mean temperature and salinity of the World Ocean Atlas climatology (WOA98; Boyer et al., 1998; Antonov et al., 1998). In the Arctic region, improved data from the Polar Science Center Hydrographic Climatology (PHC3.0; updated from Steele et al., 2001) is used in stead of the WOA98 climatology.

To spin up the model from the prescribed initial state, the model was integrated for five full cycles (Figure 3.3), each one running from 1871–2009 (Yanchun et al., 2014), yielding a total integration time of 695 years. The model is forced by the modified 20CRv2 dataset, described in the following section. As illustrated in Figure 3.3, the initial ocean state of all cycles but the first one, is the end state of the previous cycle. Consequently, at the start of each cycle (except for the first cycle), the full ocean state by the end of 2009 will suddenly be forced with the atmospheric state at the start of 1871. This mismatch will inevitably impose an inconsistency to the system, requiring some time for adjustment. For this reason, the first decade or so is typically not being accounted for. In the forthcoming analysis, the fifth (and last) cycle is used.

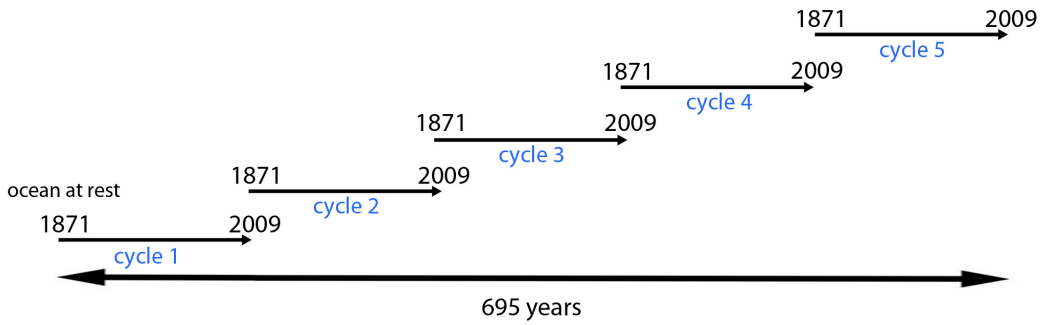

Figure 3.3: Illustration of the spin up procedure of the model. The model is integrated for five full cycles, each spanning the time period 1871–2009. Each cycle is initialised by the ocean state at the previous cycle (except the first one, starting from prescribed initial conditions as outlined in the text). The total integration time is 695 years, and the model is forced by the modified 20CRv2 dataset.

3.1.4 The adjusted 20CRv2 reanalysis data set

The following is provided from Yanchun et al. (2014), if nothing else is stated.

The global hindcast simulations for the 20th century are based on the 20CRv2 reanalysis set (Compo et al., 2011), providing momentum, heat and fresh water forcing fields for the ocean model for 1871–2009. An adjusted version of the 20CRv2 is used in this study as outlined in Yanchun et al. (2014). As a 'quality check' of the adjusted 20CRv2 reanalysis, the latter has been compared with the extensively used COREv2 air-sea flux dataset for the period 1948–2009. A conclusion from this comparison is that the adjusted 20CRv2 reanalysis is as realistic as the COREv2 reanalysis during the time period of satellite observations.

3.2 Statistical analysis

3.2.1 EOF analysis

One of the statistical methods used on this study is the so-called Empirical Orthogonal Function (EOF) analysis. The EOF analysis is a singular value decomposition (SVD) that splits a data matrix D into three linearly independent matrices (Equation 3.3). In a typical situation, climate data from observations or a model are provided in three dimensions (two spacial dimensions and one temporal dimension). Prior to decomposition, the data set is reshaped into a 2-dimensional (time $\times$ space) matrix and the data points should be presented

as area weighted anomaly values. The following expression explains the decomposition

$$D = USV^T \tag{3.3}$$

Here the data matrix D is a two dimensional $p \times n$ rectangular matrix, containing all measurements (in time and space). The U and V matrices are both orthonormal, and when $p > n$, the EOFs are provided by the columns of U and the principal components (PCs) by the the columns of V. S is a diagonal matrix containing the variance explained by the different EOF components. The data is now split into a stationary part (a spatial pattern, the EOFs) and a time dependent part (a time series, the PCs). Each PC time series corresponds to a particular EOF mode, providing the sign and amplitude of that EOF.

3.2.2 Variance, covariance and standard deviation

The variance (S_x^2) of a variable x is a measure of the variability of x about its mean, $\bar{x}$ (Emery and Thomson, 2001).

$$S_x^2 = \frac{1}{N-1}\sum_{i=1}^{N}(x_i - \bar{x})^2 \tag{3.4}$$

The standard deviation S_x is the positive square root of the variance. The covariance C_{xy} is found by:

$$C_{xy} = \frac{1}{N-1}\sum_{i=1}^{N}(x_i - \bar{x})(y_i - \bar{y}) \tag{3.5}$$

where N is the number of measurements/observations and a bar indicates the mean of the given quantity.

3.2.3 Correlation

The correlation coefficient (r) is a measure of the strength of the linear relationship between two variables (Mendenhall et al., 2012), defined as

$$r = \frac{1}{N-1}\sum_{i=1}^{N}\frac{(x_i - \bar{x})(y_i - \bar{y})}{S_x S_y}, \tag{3.6}$$

for $-1 \leq r \geq 1$. S_x and S_y are the standard deviations of the variables x

and y, respectively, and N is the number of measurements/observations. When $r = 0$, there is no linear relationship between x and y. When r is positive, there is a positive relationship between the variables, and consequently, when r is negative, there is a negative, linear relationship between x and y.

3.2.4 Cross-correlation

If one variable typically lags another, the cross-correlation function (R_{xy}) can be used to find at what lag maximum correlation occurs.

$$R_{xy}(\tau) = \frac{1}{N-k} \sum_{i=1}^{N-k} y_i x_{i+k} \tag{3.7}$$

In the above expression, τ indicates the time lag. One should be careful, however, in interpreting correlation estimates for large lags. The averaging becomes based on fewer and fewer samples and will therefore loose statistical reliability as the lag increases (Emery and Thomson, 2001).

3.2.5 Moving average filter

The moving average is a commonly used filter. In spite of its simplicity, it is optimal in reducing random noise or high frequencies, while retaining a sharp step response (Smith et al., 1997). This makes it the premier filter for time domain signals. In case of a symmetrically averaged filter, one has

$$y(t) = \frac{1}{2k+1} \sum_{j=-k}^{k} x(t+j) \tag{3.8}$$

for $t = k+1$, $k+2$,...,$n-k$. In the above expression, x is the original data, y is the filtered data, and $2k+1$ (odd integer) is the number of data points used for the averaging.

Chapter 4

Results

4.1 Climatology in the subpolar gyre

Figure 4.1 illustrates the model-simulated pattern of the averaged sea surface height (SSH) of the North Atlantic (coloured contours), from 1871–2009. The standard deviation (std) of the SSH is shown with black contours, depicting areas of small and large variability. The climatological SSH is low in the cyclonic subpolar gyre (SPG) and high in the anticyclonic subtropical gyre (STG). The largest variability of SSH is found at the border between the two gyres, and represents the position of the North Atlantic current (NAC).

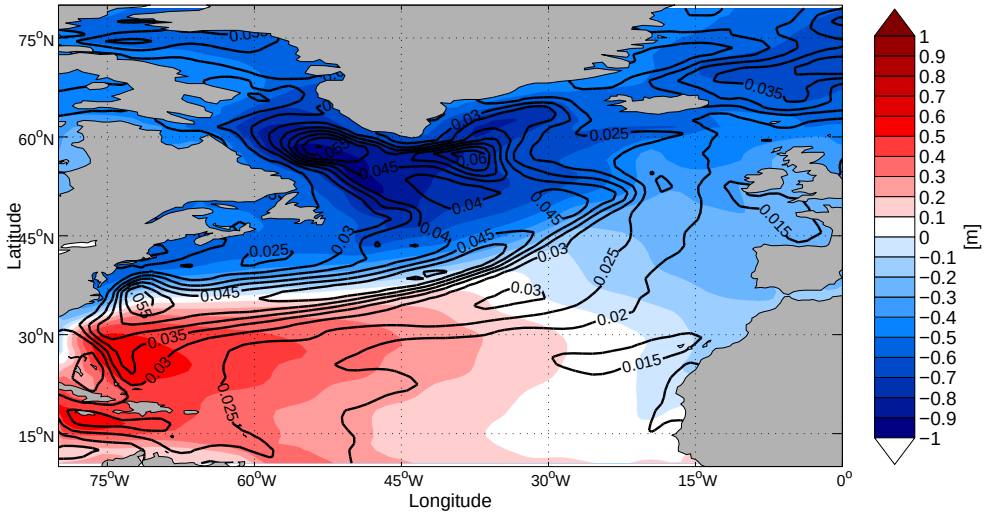

Figure 4.1: Annual mean SSH (colours) and standard deviation of the mean SSH (black contours) for the whole period, 1871–2009. The standard deviation in the centre of the Labrador Sea and Irminger Sea is 5.5 cm and 6.0 cm, respectively.

4.1.1 Definition of the area

The focus of this study is the annual to decedal variability of the ocean properties in the SPG region. To identify an area enrapturing most of the variability in this region, time series of the SSH was extracted from the Labrador Sea (LS; 57°–61° N and 50°–58° W) and the Irminger Sea (IS; 58°–62° N and 32°–39° W), the two main basins of the SPG (in addition to the Iceland basin). The definition of the area defining the basins are based on a topographic map provided by Yashayaev and Clarke (2008). These time series were correlated with annual mean SSH time series at every model grid point in the North Atlantic Ocean (Figure 4.2 **a** and **b**).

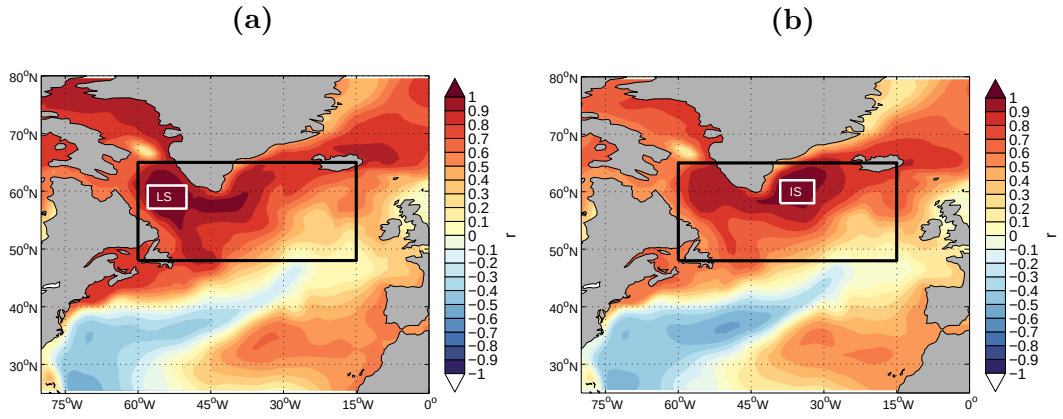

Figure 4.2: Correlation between modelled SSH time series from **(a)** the Labrador Sea (LS; 50°–58° W, 57°—61° N) and **(b)** the Irminger Sea (IS; 58°–62° N and 32°–39° W) and the SSH throughout the North Atlantic region. The LS and IS areas are both marked with white boxes. The black box, constituting the SPG region in this study, is confined to 48°–65° N and 60°–15° W.

The obtained correlations indicate the area of influence by the two chosen locations, and overall similar correlation patterns are obtained. The highest (positive) correlations are, as expected, found close to and within the basins, whereas negative correlations are mainly found near and south of the region occupied by the Gulf Stream/the North Atlantic current (NAC) at the border of the SPG and STG. In an extended area off the coast of North Africa and the Iberian peninsula, positive correlations are also apparent. Thus, an indication of a tripole mode of SSH-variability in the North Atlantic sector is seen (see Deser et al., 2010). Based on this analysis, we hereafter define the SPG region confined to 48°–65° N and from 60°–15° W (black box in Figure 4.2).

4.1.2 Vertical, hydrographic distribution

The vertical hydrographic properties in the SPG area, expressed in terms of the mean ocean temperature T and salinity S and their variability from 60°–15° W, are shown in Figure 4.3. The maximum T and S are 12.3 °C and 35.6 psu, respectively. Maximum values are located close to the surface on the eastern flank of the gyre, decreasing towards west and with depth. In the abyss, the T and S distributions are more homogeneously distributed in the zonal direction. A measure of variations in T and S within the gyre are given by the standard deviation of the mean T and S in the right-hand panels of Figure 4.3. For both T and S, the maximum standard deviations are found between 30°–40° W, extending from the surface down to a depth of approximately 1000 m. Except for this feature, variations are generally found within the upper 500 m at all

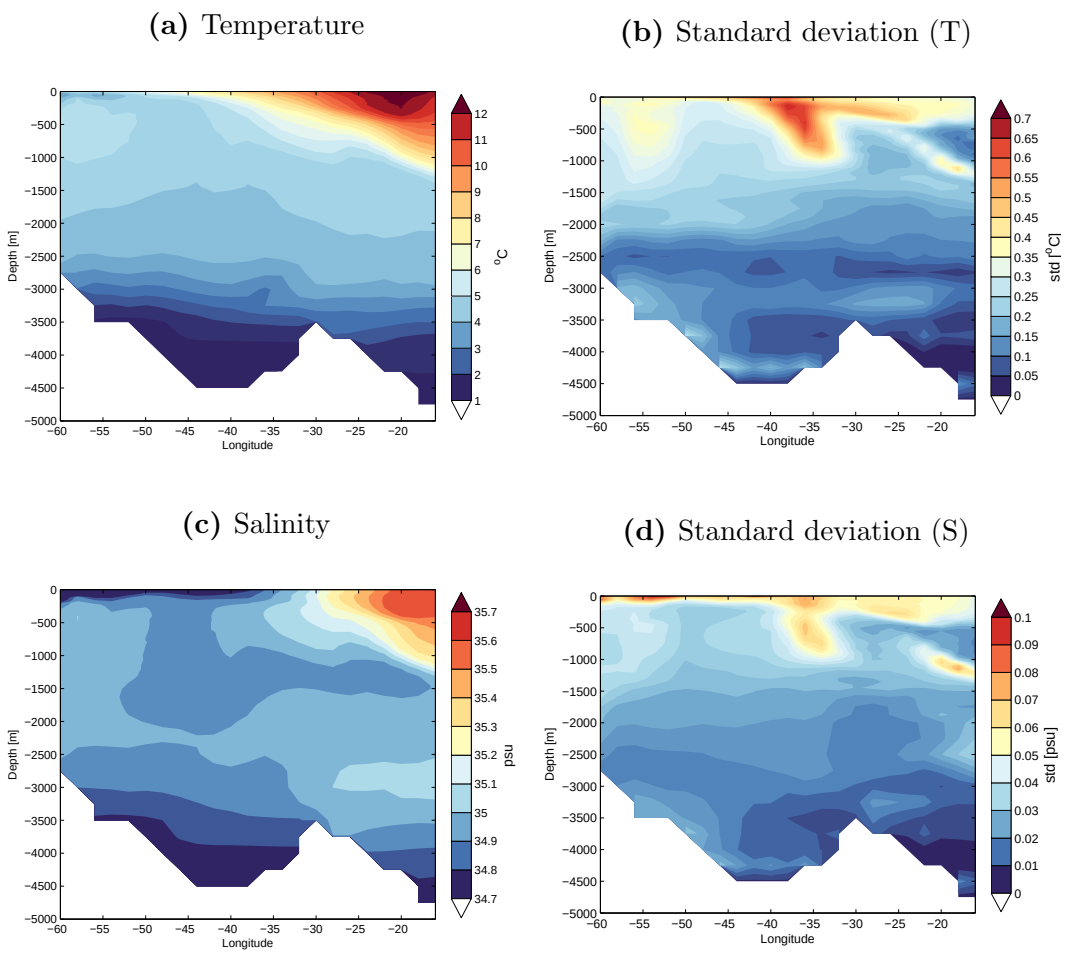

Figure 4.3: Cross section (depth and longitude) of **(a)** mean ocean temperature (T, °C) in the SPG and **(b)** standard deviation of the mean temperature (°C). The values are meridional averages over the latitudes of the SPG region (from 48–65° N) and over time (1871–2009). **(c)** and **(d)** same as **(a)** and **(b)**, but for ocean salinity S (psu).

longitudes. For this reason, much of the forthcoming analysis is confined to the upper 500 m of the water column. Similar analysis covering 0–700 m and 0–1000 m show results similar to the results presented below.

4.1.3 Temporal evolution of the subpolar gyre

Sea surface variability

In the following, the surface variability in the SPG region from 1871 to 2009 is presented. Yearly averages of sea surface height (SSH), the barotropic streamfunction (BSF), sea surface temperature (SST) and salinity (SSS) anomalies, averaged over the SPG area are displayed in Figure 4.4. Both SSH and BSF are measure of the strength of the SPG circulation (note that negative SSH and BSF anomalies correspond to a strong SPG), and the correlation between the two is $r = 0.80$. The SPG index (the strength of the gyre circulation) is in the following defined as the SSH time series. This definition of the index is chosen to compare with available observations (Häkkinen and Rhines, 2004; Hátún et al., 2005), and with analysis (e.g. Lohmann et al., 2009, 2008; Lorbacher et al., 2010).

For SST and SSS, a negative trend is found from the start of the integration until the early 1900s. After 1920, both the SST and SSS raise, whereas SSH is relatively constant. Both the SSH and BSF reach a local maximum value in the early 1940s. Starting from the mid 1990s, a rapid increase in all surface variables is evident. The SST increase starting in the beginning of the 1920s is comparable to the increase starting in the mid 1990s, but with the latter warming being more abrupt. From the beginning of the 1920s to 1940, the SST increases by about 1.0–1.1 °C and from the mid 1990s to 2008, the SST increases by about 1.3–1.4 °C. To investigate these possible trends further, time series of the average temperature and salinity from 0–500 m depth are investigated in the next section.

Top 500 m variability

Figure 4.5 **(a)** shows time series of the top 500 m temperature (T500) and salinity (S500) in the SPG-region. As evident in Figure 4.3, this is the depth range where the majority of the variations in T and S are found. The multidecedal variability in T500 and S500 is large and similar, with the largest deviation between the two time series in the 1960s. There is a tendency for variations in temperature to lead variations in salinity, as can be seen in Figure 4.5 **(b)**

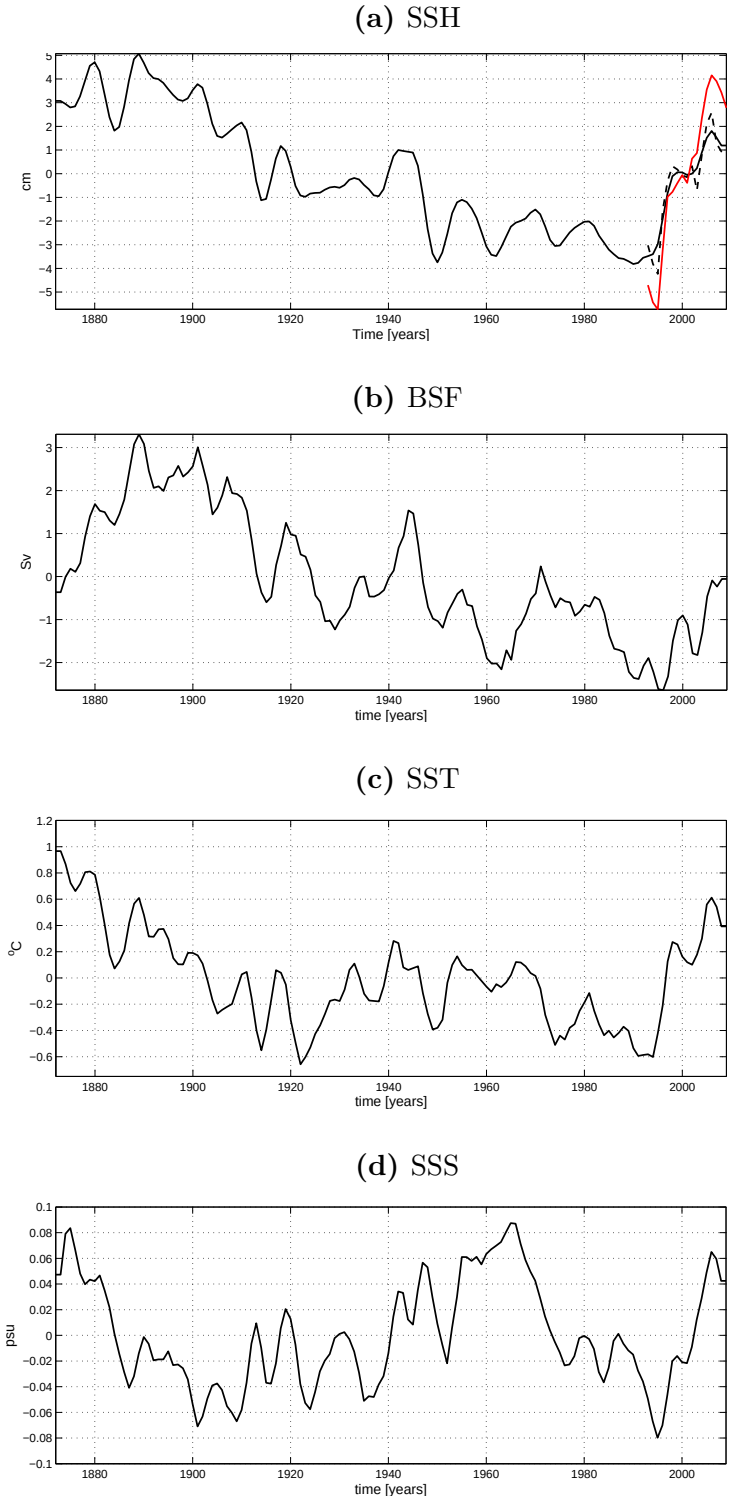

Figure 4.4: Anomalies of **(a)** SSH **(b)** BSF **(c)** SST and **(d)** SSS, all averaged over the SPG region (48–65° N, 60– 15° W). The total means ($\overline{\text{SSH}} = -64.30$ cm, $\overline{\text{BSF}} = -15.45$ Sv, $\overline{\text{SST}} = 8.58$ °C and $\overline{\text{SSS}} = 34.88$ psu) have been subtracted from the time series. The months in the annual averaging are defined from Jul–Jun, where Jan defines the year number. A 3-yr running mean is applied to all time series. The red line in **(a)** represents the corresponding sea level data that is a combination of data from TOPEX/Poseidon, Jason-1 and Jason-2/OSTM), and is available at *http* : *//www.cmar.csiro.au/sealevel/sl_data_cmar.html* The black, dashed line in **(a)** is SSH without a running mean. The correlation between the gyre indices defined as SSH and BSF averaged over the SPG is $r = 0.80$.

showing the cross-correlation between the two quantities. Maximum correlation ($r = 0.88$), is found when T500 leads S500 with one year lag. T500 and S500 reveal similar tendencies as the SST and SSS time series (Figure 4.4 **c** and **d**). The negative trends in the first 50 years of the time series ends around 1922–1923, followed by a period of increasing temperature and salinity. Both quantities increase in phase until the mid 1940s. In the following period, until the end of the 1960s, S500 is generally higher than T500. Thereafter, both T500 and S500 drop until the mid 1990s. Starting from 1995/1996, both temperature and salinity undergo a rapid increase, unprecedented in the presented time series.

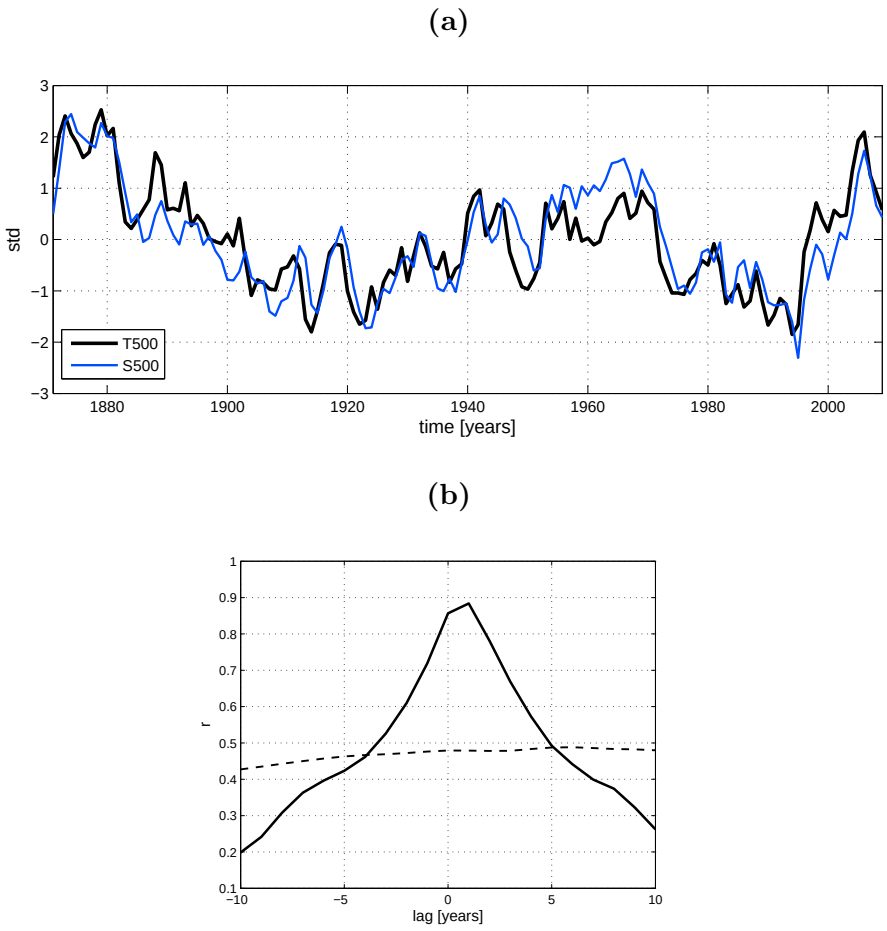

Figure 4.5: **(a)** T and S averaged over the top 500 m (T500, S500) of the SPG region as defined by the black box in Figure 4.2. The mean T500 and S500 for the time period is 7.13 °C and 35.04 psu, respectively. The time series are scaled by the standard deviations; 0.27 °C for T500, and 0.028 psu for S500. **(b)** Cross-correlation between T500 and S500, with maximum correlation of $r = 0.88$ when T500 leads S500 with one year. The dashed line in panel **(b)** indicates the 95% significance of the cross-correlation. The number of degrees of freedom are adjusted at each lag, and auto-correlation has been accounted for.

It is found that there are two periods characterised with a transition from decreasing to increasing values in temperature and salinity; the first starting in the early 1920s and second starting in the mid 1990s. In the following sections, these two periods will be studied. To investigate and compare the two 'warming' events, shorter periods have been selected for further analysis and comparison, to explore possible similarities and differences. In order to investigate the ocean states prior to the warming, preconditioning periods have been chosen for the two events based on Figure 4.5 **(**a). For the 1920s warming, the preconditioning period is chosen as 1920–1925, and for the 1990s warming the preconditioning period is defined as 1990–1995. The choice of the second preconditioning period is more obvious than the first, as the warming in 1995/96 is more abrupt. The mid 1920s warming is more gradual, but as for the mid 1990s shift, there is a clear transition from declining to increasing T and S trends in the beginning of the 1920s (Figure 4.5 **a**). The preconditioning period is defined as to include years of relatively low temperatures compared to the later parts of the 1920s. This choice is supported by the analysis of e.g. Rogers (1985) and Drinkwater (2006), who argue that the warming in the Greenland area (1926) lagged behind that in areas further east, and that especially after 1925, temperatures began to rise rapidly in the North Atlantic.

4.2 Atmospheric forcing of the ocean during the 1920s and 1990s periods

The following sections include analysis of the atmospheric condition and forcing before and during the mid 1920s and the mid 1990s warming events. Variations in the sea level pressure (SLP; Section 4.2.1), the North Atlantic Oscillation (NAO; Section 4.2.2) and the associated wind fields (Section 4.2.3), impact the dynamics of the ocean state (Section 4.3). Particular focus will be given to the preconditioning phases, as explained in Chapter 1.

4.2.1 Sea level pressure

The mean sea level pressure (SLP) distribution from 1871–2009 is displayed in Figure 4.6, providing the climatological SLP of the North Atlantic. The pattern is characterised by a low pressure centred south-west of Iceland and a high pressure centred near the Azores. The anomalous winter (djfm) SLP distribution for the periods before and during the warming events are presented in Figure 4.7.

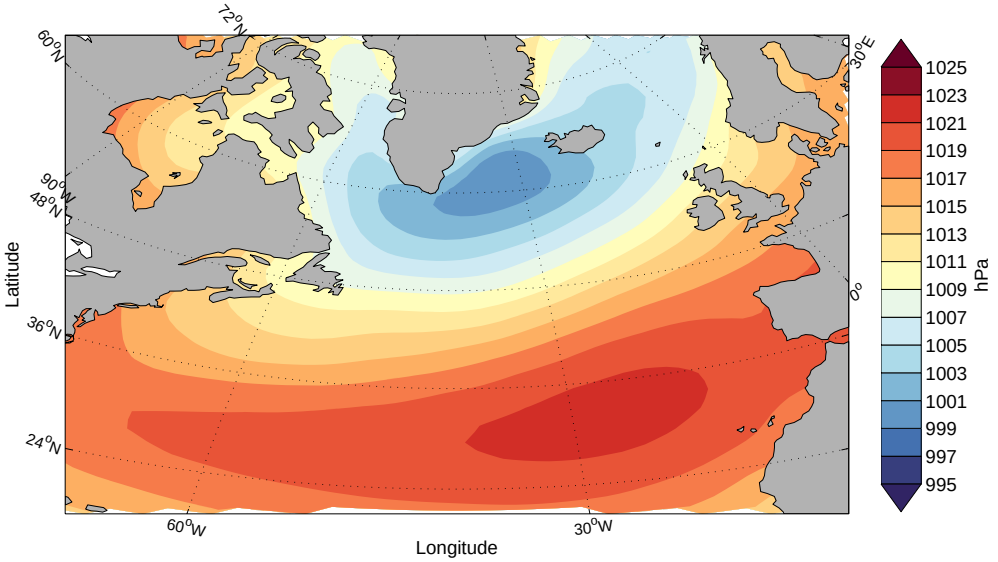

Figure 4.6: Mean winter (djfm) SLP (hPa) for the whole period, 1871–2009.

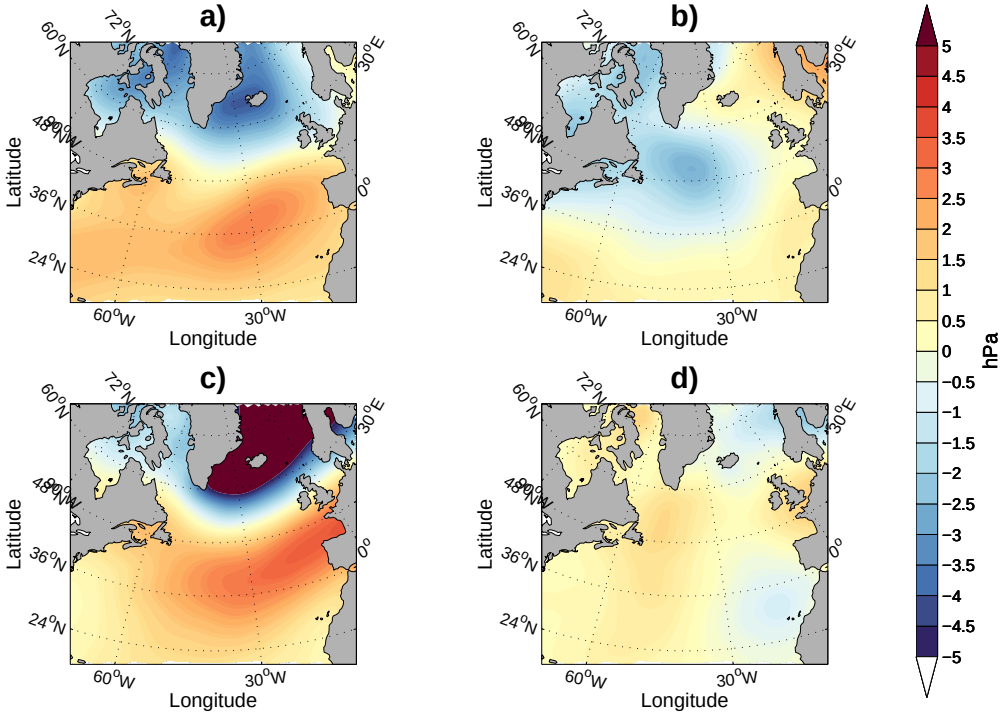

Figure 4.7: Winter (djfm) SLP anomalies (hPa) for the periods **a)** 1920–1925, **b)** 1926–1932, **c)** 1990–1995 and **d)** 1996–2002.

The mean SLP anomalies during the preconditioning periods (Figure 4.7 **a** and **c**), both reveal a deeper than normal Icelandic low and a higher than normal Azores' high, in addition to a north-easterly shift in the low and high pressure centres compared to the climatology (Figure 4.6). The pressure gradients between the two centres are large, and especially so for the second preconditioning period prior to the mid 1990s shift. A pronounced change in the SLP distribution is evident for the two following warm periods (Figure 4.7 **b** and **d**). The gradients have weakened, and the centres have moved. For the 1925–1932 period, the low is located further south-west, and in the 1996–2002 period, the SLP pattern is much more equal to the total average (with two weak lows).

4.2.2 The North Atlantic Oscillation

To investigate possible dominant modes explaining the variability in the SLP and thereby the geostrophic winds, an Empirical Orthogonal Function (EOF) analysis (see Section 2.4) has been performed. The average of the winter (djfm) SLP over the Atlantic sector (20–80° N, 90° W–40° E) from 1871 to 2009, was used in the analysis. Figure 4.8 **(a)** shows the leading EOF mode. It explains 42% of the total variance, and is the dominant SLP mode in the North Atlantic sector. The second, third and fourth EOF modes were also computed (not shown), explaining considerably less of the total variance (14%, 10% and 7%, respectively), and are not further discussed. The time series of the leading EOF mode (the leading Principal Component, PC1) is displayed in Figure 4.8. This time series serves as an alternative index to the commonly used station-based NAO index (see Hurrell, 1995). Climate Data Guide; A. Phillips (2014) performed an EOF analysis on SLP data for the period 1899–2013, and found a correlation of 0.93 between the station-based NAO index and the PC1 component.

The dominant mode of SLP variability (EOF1) is recognized by a dipole structure over the North Atlantic sector. Low SLP values are found over the northernmost parts of the North Atlantic, with higher values in the STG region. This is consistent with the main feature of the winter time NAO (see Section 4.2.2), involving a shift in the atmospheric mass between the subtropics and the polar regions. Thus, the PC1 time series (Figure 4.8 **b**) gives a measure of the sign and amplitude of the NAO. It follows from the time series that four periods are recognised by sustained NAO^+ forcing (with duration of 5 years or more), starting in 1903, 1920, 1972 and 1989, respectively. The preconditioning periods,

1920–1925 and 1990–1995, are thus within a period dominated by positive NAO forcing. The two following periods, 1926–1932 and 1995–2002, are influenced by varying strengths and signs of the NAO index. It is also found that 1996 was a year with relatively large negative NAO index, particularly compared to the previous seven years.

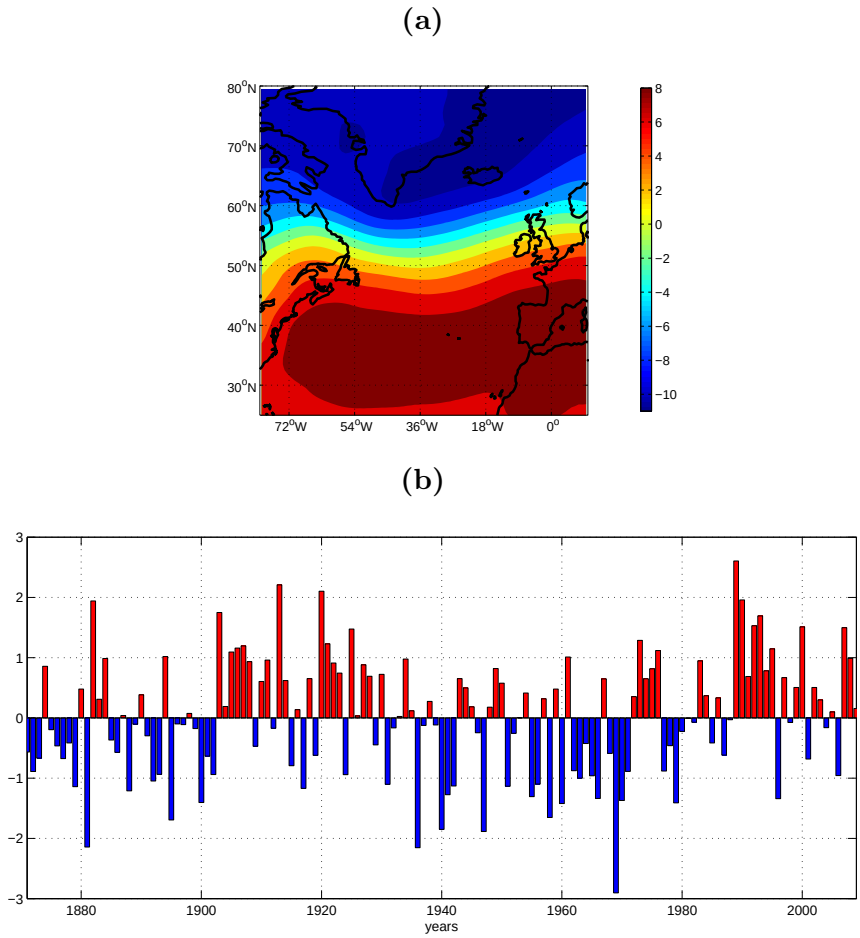

Figure 4.8: **(a)** The dominant EOF mode over the Atlantic sector (20°–80° N, 90° W–40° E) for the normalised winter (djfm) SLP anomalies. The explained variance is 42.1%. **(b)** The PC time series of the leading EOF of winter (djfm) SLP anomalies over the Atlantic sector, which serves as one of several NAO indices (Hurrell, 1995).

4.2.3 Wind stress

The wind stress forcing over the North Atlantic is related to the strength and pattern of the NAO forcing (Section 2.2.2) through geostrophic winds. The mean wind stress distribution, with arrows indicating the wind direction, is displayed in Figure 4.9. The wind systems in the North Atlantic are dominated by near zonally directed flows; the Westerlies north of 30° N and the

North Eastern Trade Winds at lower latitudes. The atmospheric flow vary in magnitude and direction depending on the pressure distribution, influencing the dynamics (through surface drag) and hydrography (through heat and fresh water surface fluxes) in the SPG area. To investigate the transfer of momentum from the atmosphere to the ocean prior to and during the two warming events, anomalies of the absolute wind stress for the four periods are shown in Figure 4.10.

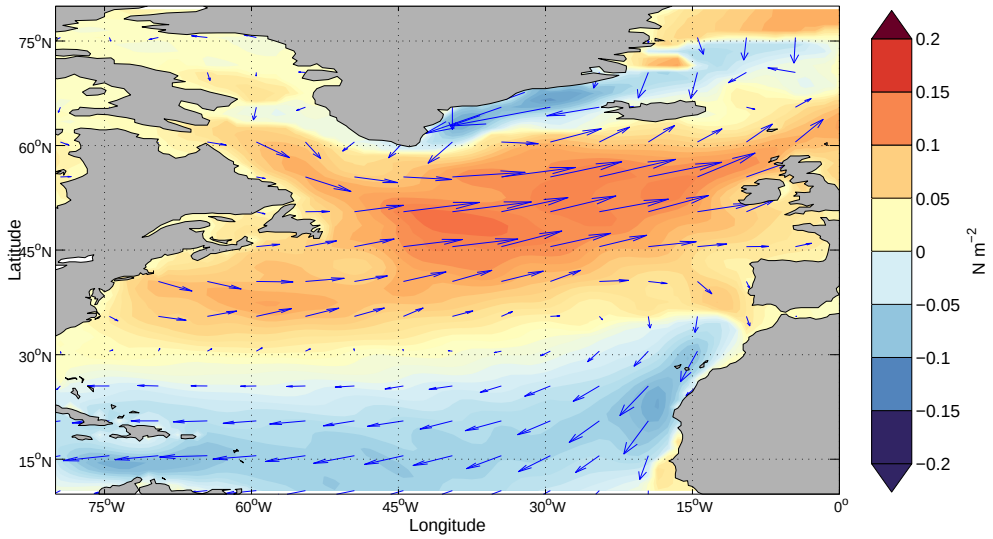

Figure 4.9: Annual mean wind stress (N m^{-2}) from 1871–2009. Arrows indicate the direction of the flow, and the colours show the magnitude.

During both preconditioning periods (Figure 4.10 **a** and **c**), the absolute wind stress is stronger than normal along the mean path of the Westerlies in the central North Atlantic, with a tendency of a northward shift and extension for the second preconditioning phase. These features coincide with the SLP distribution for the corresponding periods (Figure 4.7 **a** and **c**), characterised by stronger than normal SLP gradients. The following warm periods (Figure 4.10 **a** and **d**) reveal different wind stress distributions, with weaker westerly winds compared to the preconditioning phases. During the 1920s warming, negative anomalies are found south-east of Greenland, due to a weakening or a southward shift of the westerlies. For the mid 1990s warming, positive wind stress anomalies dominates the North Atlantic, but considerably weaker than during the preconditioning.

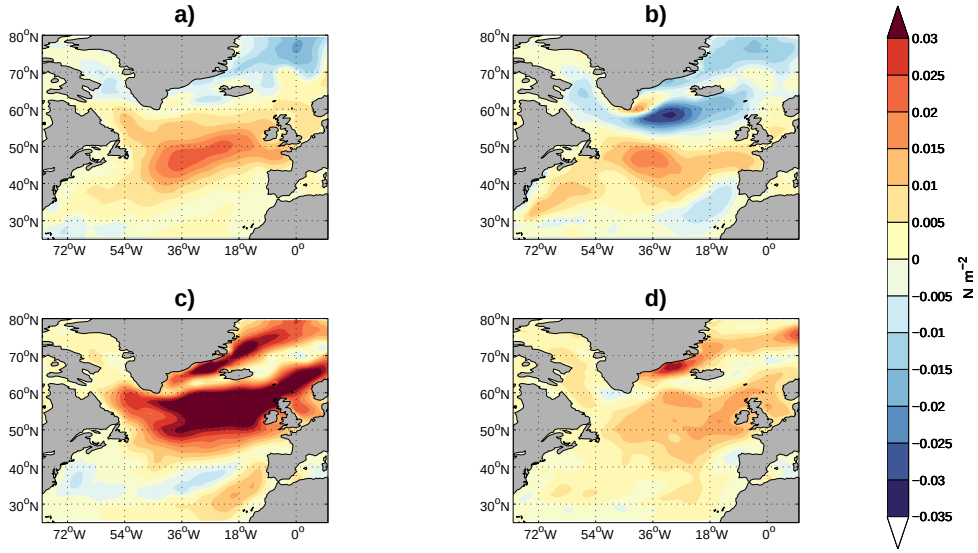

Figure 4.10: Absolute annual wind stress anomalies (N m^{-2}) for the periods **(a)** 1920–1925 **(b)** 1926–1932 **(c)** 1990–1995 and **(d)** 1996–2002.

4.3 Ocean response

4.3.1 Ekman pumping

The Ekman pumping (w_{EK}; see Section 2.3.3) for the four periods are presented in Figure 4.12. The mean pattern of w_{EK}, derived from the surface stress field, is shown in Figure 4.11. The overall distribution is consistent with theory and observations (Marshall and Plumb, 2008), with downwelling in the subtropics and upwelling in the subpolar region, both with typical values of 50 m yr^{-1}. Note the indication of a zero Ekman pumping zone, separating the two ocean gyres along the mean path of the NAC (Figure 4.11). The Ekman pumping field contains a prominent wave pattern, which is a (reanalysis) model artifact and not a real phenomenon. This artifact likely originates from the spectral computation of the wind field in the 20CR reanalysis product (see Section 3.1.4). A related problem with spectral methods is the so-called Gibbs-phenomenon (Gottlieb et al., 2011), giving rise to oscillations near sharp gradients.

Looking at the preconditioning patterns in Figure 4.12 **(a)** and **(c)**, an overall enhancement of the climatological field is found. Anomalous upwelling is seen in the region north of the zero Ekman pumping zone, and anomalous downweling is found in the region south of this zone, both with values of 20–30 m yr^{-1}. The distribution in the warm periods (Figure 4.12 **b** and **d**) differs from thos in the preconditioning.

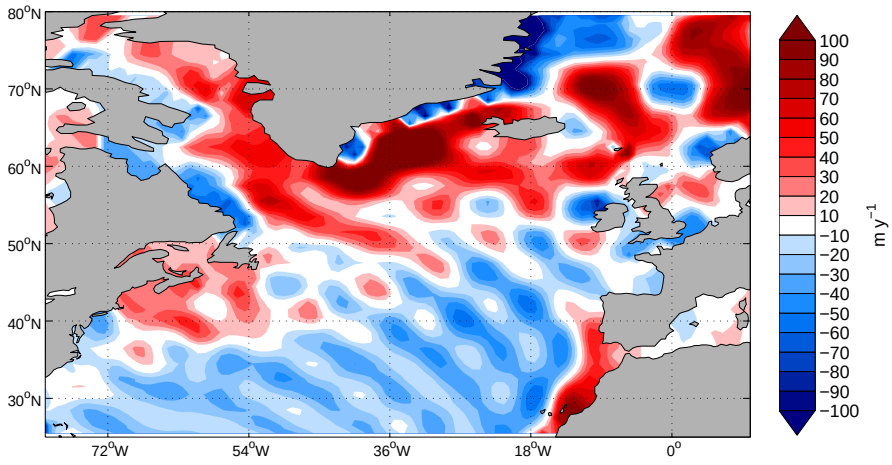

Figure 4.11: Mean Ekman pumping, w_{EK} ($\mathrm{m\,yr^{-1}}$), from 1871–2009. Red colour indicates upwelling and blue colour indicates downwelling.

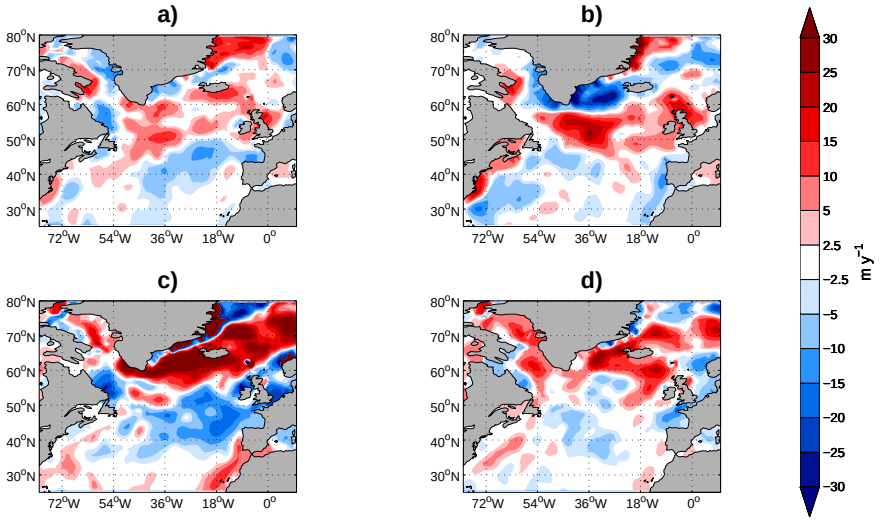

Figure 4.12: Anomalous Ekman pumping ($\mathrm{m\,yr^{-1}}$) for the periods **(a)** 1920–1925 **(b)** 1926–1932 **(c)** 1990–1995 and **(d)** 1996–2002. Red colours indicate positive (upwards) anomalies and blue colours indicate negative (downwards) anomalies.

4.3.2 Thermal and haline contribution to steric height

The steric height and the relative contribution of temperature and salinity to changes in the steric height (see Section 2.3.6) before and during the warming periods, are presented in Figures 4.13–4.15.

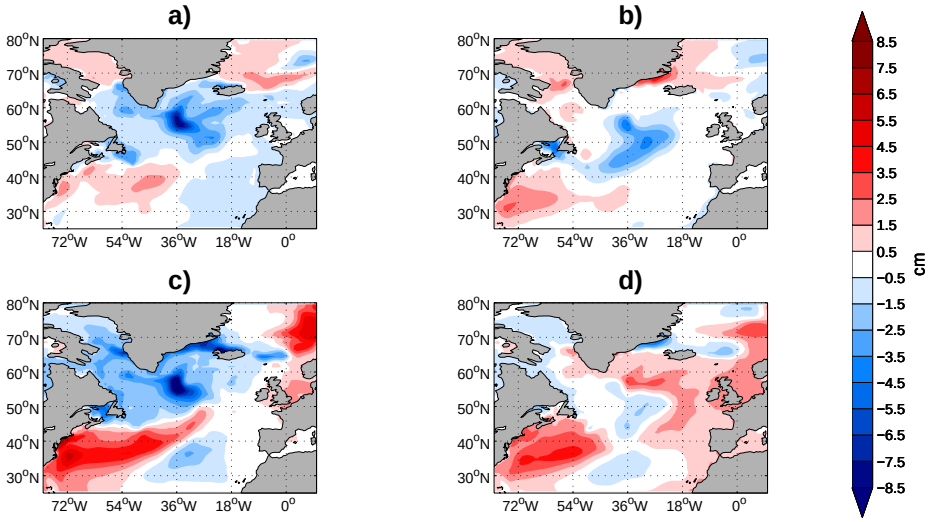

Figure 4.13: Thermal contribution to steric height (cm) for the periods **(a)** 1920–1925, **(b)** 1926–1932, **(c)** 1990–1995, and **(d)** 1996–2002. Red (blue) colours indicate positive (negative) contriution to the steric height.

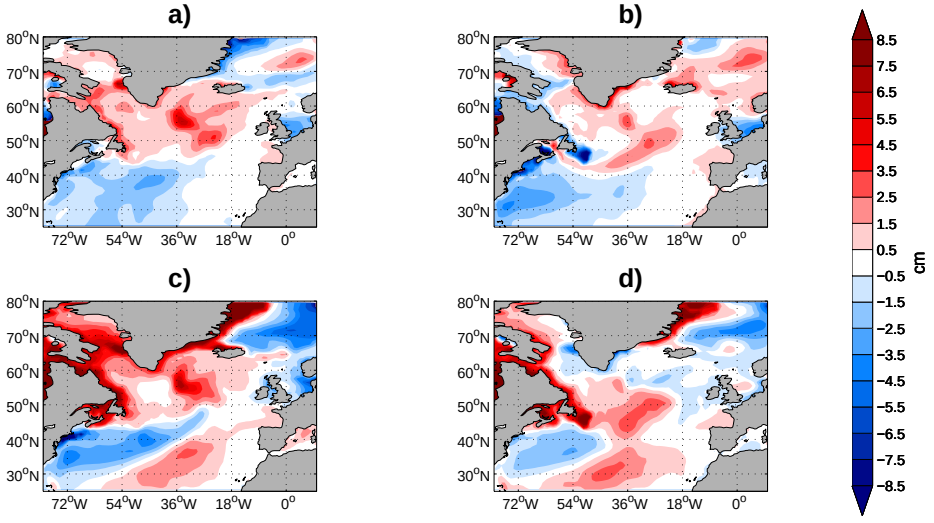

Figure 4.14: Same as Figure 4.13, but for the haline contribution to steric height.

Figure 4.13 shows the mean thermal contribution for the four periods. When comparing the preconditioning periods (1920–1926 and 1990–1996) of the two events (Figure 4.13 **a** and **c**), similarities are found. A tripolar mode with negative amplitudes in the SPG region, positive amplitudes in the area of the NAC and again negative amplitudes in the north-eastern subtropical gyre is found for both periods. This pattern is, however, most prominent in the 1990s preconditioning phase. A negative thermal contribution indicates buoyancy loss due to cooling or advection of cold water, whereas a positive contribution indicates increased temperatures. Negative contributions of 5–8 cm is found in the SPG area for both preconditioning periods.

The haline field (Figure 4.14) is generally opposite to that of the thermal contribution. During the preconditioning phases (Figure 4.14 **a** and **c**), the SPG region is characterised by positive amplitudes, consistent with lower than average salinity. Negative amplitudes are found in the area of the NAC, consistent with higher salinity. The signals are again most prominent for the latest preconditioning. In the eastern part of the subtropical region, the salinity contribution tends to be positive, indicating a negative salinity anomaly. Figure 4.15, showing the combined steric effect, demonstrates that changes in the steric height is dominated by temperature and that it is partly counteracted by salinity. This results in a pattern more similar to that of the thermosteric height. In the SPG area, the combined steric effect results in somewhat smaller amplitudes than that for the thermal contribution.

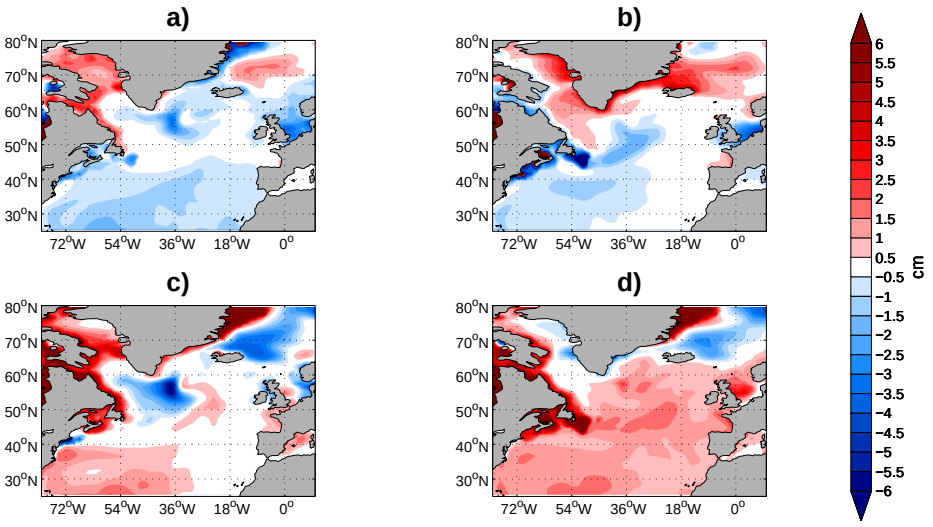

Figure 4.15: Same as Figure 4.13, but for the combined steric effect

The thermal and haline contributions during the warm events (1926–1932 and 1996–2002) are displayed in Figures 4.13 and 4.14 **(b)** and **(d)**, respectively. The increased temperature contributes to increase the steric height (Figure 4.15 **b** and **d**) over most of the North Atlantic compared to the preconditioning phases (Figure 4.15 **a** and **c**). A reversed contribution follows from the enhanced salinity (Figure 4.14 **b** and **d**). For the first warm period, the combined steric effect (Figure 4.15 **b**) reveals positive change along the western and eastern coasts of southern Greenland, and the negative values in the eastern part of the North Atlantic seen in the preconditioning period, disappears. For the second warm period (Figure 4.15 **d**), increased steric heights dominate throughout most of the North Atlantic, south of the Greenland-Scotland Ridge.

4.3.3 Heat flux

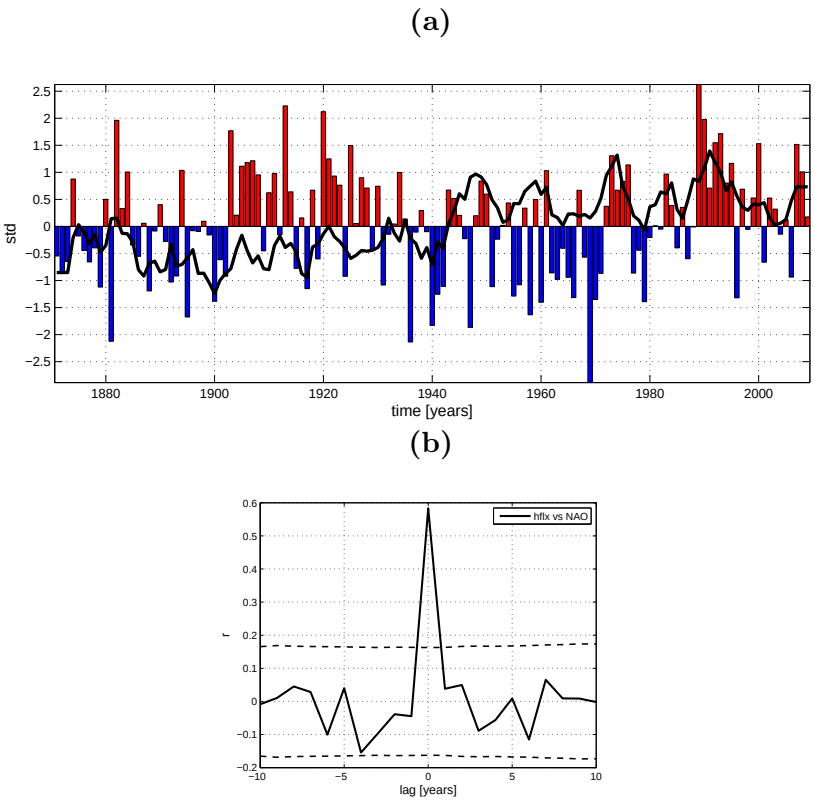

Figure 4.16: **(a)** Winter (djfm) heat flux avereraged over the SPG (black line) and the NAO index (bars). The time series are normalised, and a five year running mean is applied to the heat flux time series. The mean heat flux is 228.3 W m^{-2}, and the standard deviation is 23.5 W m^{-2}. **(b)** Cross-correlation between the heat flux and NAO time series. The maximum correlation of $r = 0.58$ is found at zero lag. The dashed line indicates the 95% significance threshold. The number of degrees of freedom are adjusted at each lag, where auto-correlation has been accounted for.

The winter-averaged heat flux in the SPG is displayed together with the NAO index in Figure 4.16. Positive values of the heat flux corresponds to heat being lost from the ocean. It is found that years dominated by positive NAO forcing coincide with increased loss of heat from the ocean. A trend can be seen in the heat flux time series, being below the long-term mean prior to 1940 and above the mean after 1940. From 1917 into the beginning of the 1920s, the heat flux increases, implying increased loss of heat from the ocean to the atmosphere. Larger heat loss is found prior to the second warming, starting in the mid 1980s. Figure 4.16 **(b)** displays the cross-correlation between the heat flux and the NAO index. The maximum correlation is found at zero lag with $r = 0.58$ (statistically significant at the 95% significance level).

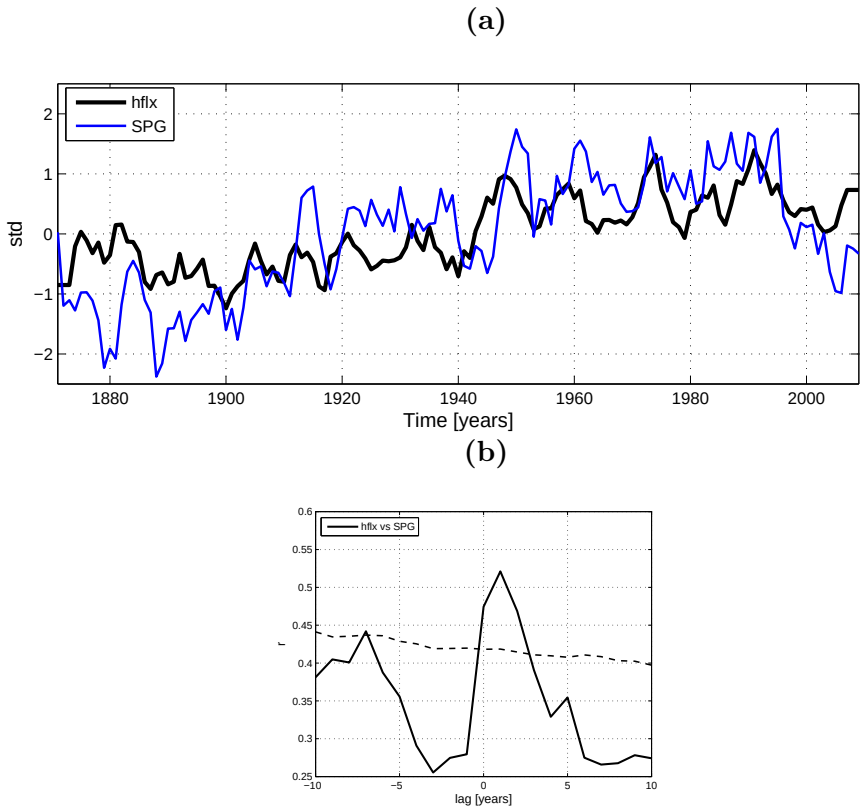

Figure 4.17: **(a)** Normalised winter (djfm) heat flux anomalies averaged over the SPG (black line) and the SPG index (blue), the latter defined as the normalised winter SSH averaged over the SPG region. A 5-yr running mean is applied to the heat flux time series. **(b)** Cross-correlation between the heat flux time series and the SPG index. The heat flux is leading the gyre circulation and maximum correlation is found at one year lag, with $r = 0.52$. The dashed line indicates the 95% significance line. The number of degrees of freedom are adjusted at each lag and auto-correlation has been accounted for.

Figure 4.17 **(a)** shows the corresponding heat flux time series together with the normalised SPG index, defined by means of the SPG SSH (see Section 4.1.3). Note that the sign of the SPG index has been reversed, so that a large heat loss corresponds to a strengthening of the gyre. It is found that the heat flux leads the SPG index by one year (Figure 4.17 **b**), yielding a correlation of $r = 0.52$ (statistically significant at the 95% significance level).

4.3.4 Deep mixing in the subpolar gyre

To investigate the effect of winter mixing in the SPG on the vertical density stratification, isopycnic layers in the SPG region have been averaged over the winter half of the year (djfm), providing time series of the density evolution of the layers in the area (Figure 4.18 **a**). It follows from the figure that layer 31, 32 and 33 are the layers with the largest variations in thickness. The potential densities of these layers vary from $\sigma_2 = 36.728$ kg m^{-3} to 36.843 kg m^{-3}, and the mean thicknesses of the layers are 320.6 m (layer 31), 690.3 m (layer 32) and 386.3 m (layer 33). The depth interval of the layers range from about 800 to 2000 m. Figure 4.18 **(b)** provides time series of the total volume of these three layers. Layer 31 contains the largest volume until the beginning of the 1900s. After this, layer 32 increases its volume, and dominates throughout the remaining time period. Note that layer 33, the densest layer of the three, does not get active until after around 1945. Thereafter this layer experiences relatively large increase in volume, with a maximum value found in the mid 1990s.

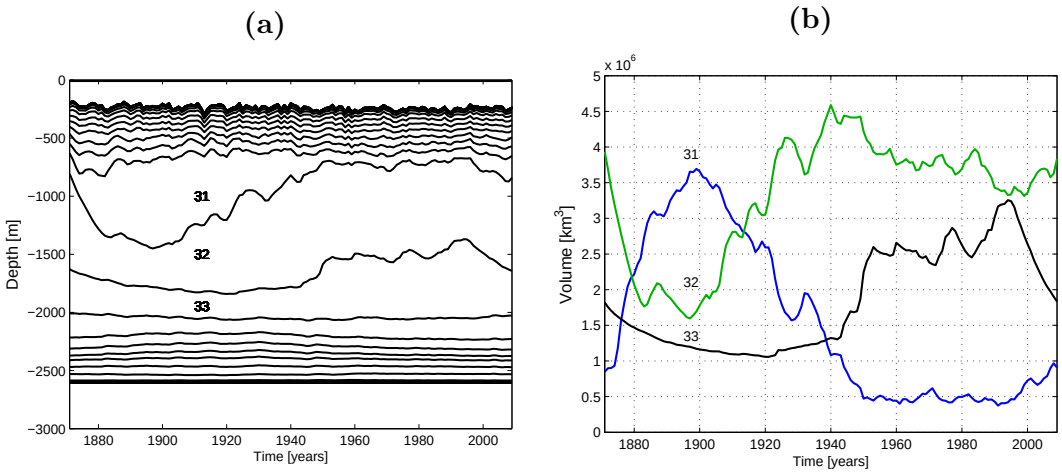

Figure 4.18: **(a)** Winter (djfm) averaged isopycnic layer depths in the SPG and **(b)** volume of the three most active layers in the SPG. The mean volume of layers 31, 32 and 33 are 1.54, 3.31 and 1.85 $\times 10^6$ km^3, respectively.

Deep mixing in the Labrador Sea and the Irminger Sea

As explained in Section 2.3.7, the LS is the most important location for winter mixing. To further investigate the production of intermediate to deep water masses in the SPG area, the isopycnic layers in the LS and the IS have been studied. Figure 4.19 **(a)** shows the average thickness of layer 32 in the North Atlantic, with the area defined as the LS and IS (see Section 4.1) indicated with black boxes. Figure 4.19 **(b)** shows the normalised anomalies of the volumes of layer 32 and 33 in the LS and the IS. The mean thicknesses and variations of the layers in the LS are larger than those found in the IS, see caption to Figure 4.19. As for the convective evolution in the SPG, layer 33 does not get active until after the mid 1940s.

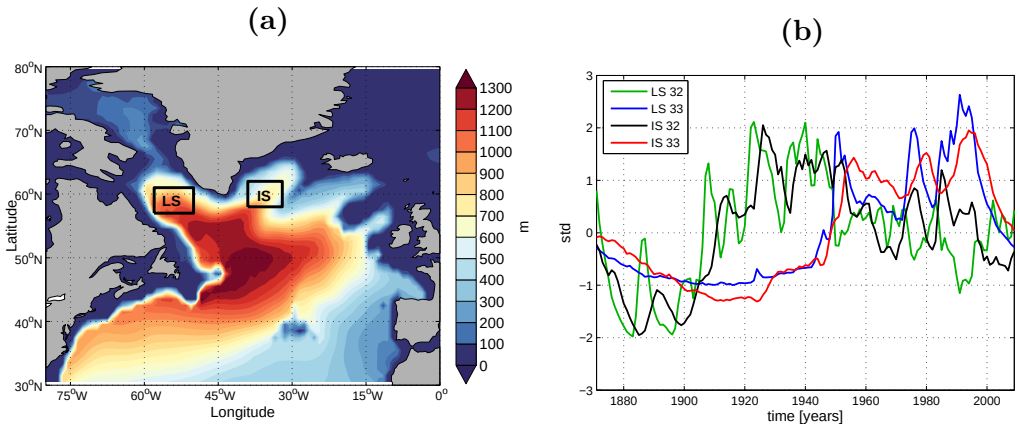

Figure 4.19: **(a)** Mean thickness of the isopycnic layer 32 from 1871–2009. The LS and IS are indicated with black boxes, and the areas are defined as in Section 4.1. **(b)** Normalised thickness anomalies of layer 32 (green) and 33 (blue) in the LS and layer 32 (black) and layer 33 (red) in the IS. Mean thickness of layer 32 is 882.29 m (std = 289.0 m) in the LS and 638.0 m (std = 159.5 m) in the IS, and mean thickness of layer 33 is 550.9 m (std = 276.1 m) in the LS and 562.8 m (std = 179.5 m) in the IS.

During the first preconditioning period (1920–1925), enhanced deep mixing occurs, causing layer 32 to increase its volume in both basins. This is followed by reduced formation of intermediate and deep waters in the subsequent warmer period. For the second preconditioning period (1990–1995), layer 33 increases in volume and reaches it's maximum value in 1995/96. This peak value is observed in both basins, being largest in the LS. After the mid 1990s, the volume of layer 33 decreases rapidly. It furthermore seems that the deep mixing in the IS lags that in the LS. Consistent with this, a cross-correlation of the layers in the two basins (not shown) gave maximum correlation for layer 32 at 3 years

lag ($r = 0.85$), and maximum correlation for layer 33 ($r = 0.95$) at 4 years lag.

4.3.5 Atlantic Meridional Overturning Circulation

The formation of intermediate and deep water masses in the SPG is directly linked to the Atlantic Meridional Overturning Circulation (AMOC; see Section 2.3.8). Figure 4.20 **(a)** shows time series of maximum AMOC in Sverdrup (1 Sv = 10^6 m^3 s^{-1}) between 20° N and 60° N, at 26.5° N and at 45° N. Observation-based values from 2004–2009 at 26.5° N is also included (red line) All three time series reveal a slight decrease in the AMOC during the first 30 years of integration, followed with a gradual increase until around 1960. Looking at AMOC at 26.5° N (dashed line), the magnitudes increase from around 16 Sv in the beginning of the 1900s to above 18 Sv in the 1940s. After 1940, the AMOC strength fluctuates between 18 and 20 Sv. The time series of maximum AMOC between 20° and 60° N is similar to that at 26.5° N, with a correlation of $r = 0.94$. The AMOC at 45° N has a lower correlation with the maximum ($r = 0.80$) and is expected to contain larger variability, as this latitude is in the boarder area between the subpolar and subtropical gyres. Therefore, the AMOC variability at 26.5° N will mainly be the focus in forthcoming analysis.

Since the temporal behavior of the AMOC varies throughout the entire Atlantic ocean, Hovmöller diagrams (Figure 4.20 **b**) are included, displaying AMOC (the maximum value at depth of the AMOC streamfunction) as a function of time and latitude. Due to the above mentioned transition in the AMOC strength (from the 1920s to the 1960s) the time series are divided in two parts; prior to and after 1950. The anomalies in each periods are presented. The AMOC relates to the meridional heat transport (MHT), which is shown in Figure 4.20 **(c)**. Similarities are evident between the MHT anomalies and the AMOC strength anomalies. For the period prior to 1950, small positive anomalies are found in the region between 40°–60° N, around the 1920s. Stronger positive anomalies of the AMOC are found in the mid 1990s reaching the latitudes of the SPG, with corresponding enhancement of the MHT.

(a) AMOC

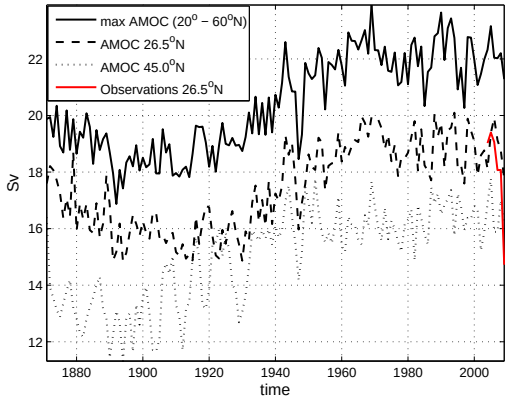

(b) AMOC

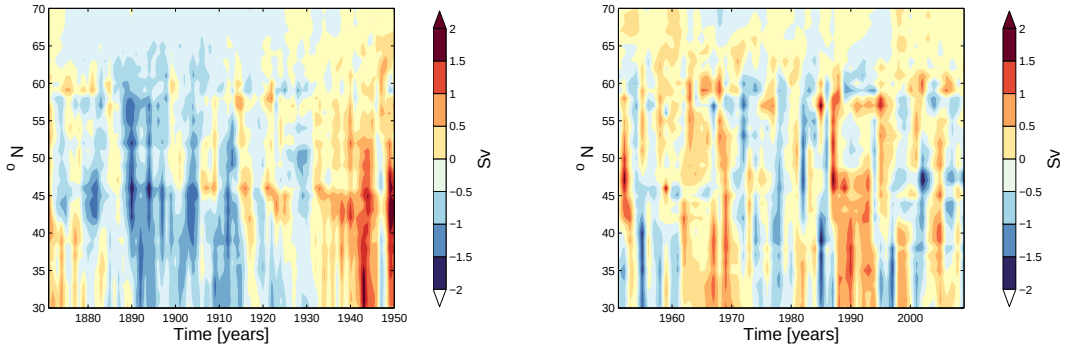

(c) MHT

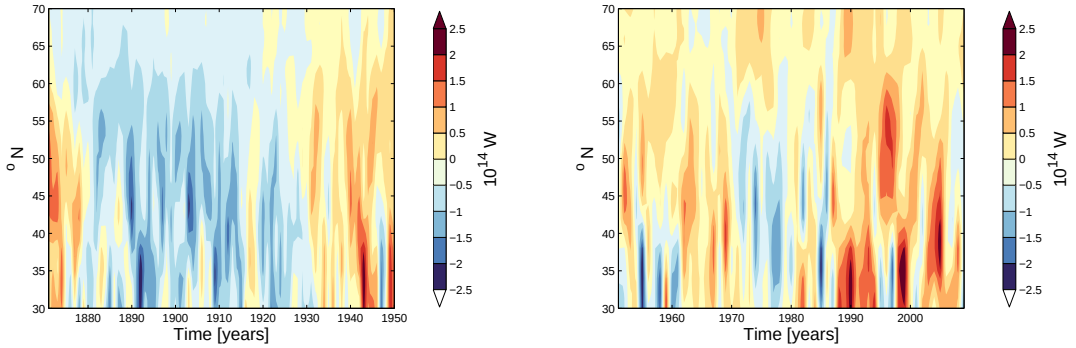

Figure 4.20: **(a)** Maximum AMOC (Sv) between 20° N and 60° N (solid line), at 26.5° N (dashed line), and 45.0° N (dotted line). Correlations between the maximum AMOC and AMOC at 26.5° N and 45.0° N are $r = 0.94$ and $r = 0.80$, respectively. Observation-based values (from april 2004 to 2009) at 26.5° N is indicated in red (data from the RAPID MOC monitoring project, available from www.rapid.ac.uk/rapidmoc). **(b)** Hovmöller diagram of the AMOC strength (the maximum strength with depth) as a function of time and latitude (Sv). The values are zonally averaged across the Atlantic Ocean, and the mean at every latitude has been subtracted. Left panel shows anomalies for the period prior to 1950 and the right panel shows anomalies for the period after 1950. **(c)** Same as **(b)** but for the MHT (10^{14} W). Monthly averages are subtracted before calculating the yearly means.

Chapter 5

Discussion

5.1 Model verification

Due to limited observational records, Ocean General Circulation Models (OGCMs) provide an important tool for investigating long-term climate variability (Griffies et al., 2009). However, uncertainties in atmospheric reanalysis products and OGCM biases based on improper/lacking physics and/or numerical choices may lead to varying degrees of realism among available models (Yeager and Danabasoglu, 2014). Therefore, comparison to available observations is necessary when interpreting model output. To evaluate the model simulations used in this study, comparison to observational records of particular relevance for the SPG is presented. In Chapter 4, altimeter data from 1992–2009 (Section 4.1.3) and the observation-based AMOC strength at 26.5° N from 2004–2009 (Section 4.3.5) are presented, both of which are in general agreement with the corresponding simulated quantities. In the following sections we examine observed, global climatologies of SST and SSS for the period 1955—2006 (Section 5.1.1), time series of observed temperature south-west of Greenland from 1876–2009 (Section 5.1.2), and observed salinity from the Irminger Current for the period 1971–2005 (Section 5.1.3). Observations of the Gulf Stream Index (GSI) are provided in Section 5.4.1.

An apparent change is found around 1945 in the time series of the isopycnic layers in the SPG region (Figure 4.18 and 4.19) and in the time series of the AMOC strength (Figure 4.20). Correspondingly, the hydrographic properties change rapidly around 1945, and a significant long-term increase in the AMOC strength is found (further detains in Section 5.4.7). It is hard to conclude whether this is a real change in nature or a side effect of the quality of the atmospheric reanalysis product. As stated above, comparison to observations is

highly desirable when interpreting output of model simulations. Unfortunately, generally few observations in time and space limit verification on decadal time scales, and then particularly before the 1950s (Cunningham et al., 2007).

5.1.1 Global climatology

Figure 5.1 shows the global, annual mean climatologies of modelled SST and SSS from 1955–2006 (left panels). The difference between simulated and observed SST and SSS are presented in the right panels. As can be seen in Figure 5.1 **(b)**, the model simulates too low SST in the coastal seas of the Arctic and in the Nordic Seas. Warm biases are found adjacent to the east coast of North America, along the Equator and around the southern coast of Greenland. In addition, the SST field in the Southern Ocean is, in general, too high. The largest SSS biases are found in the Arctic Ocean, particularly on the

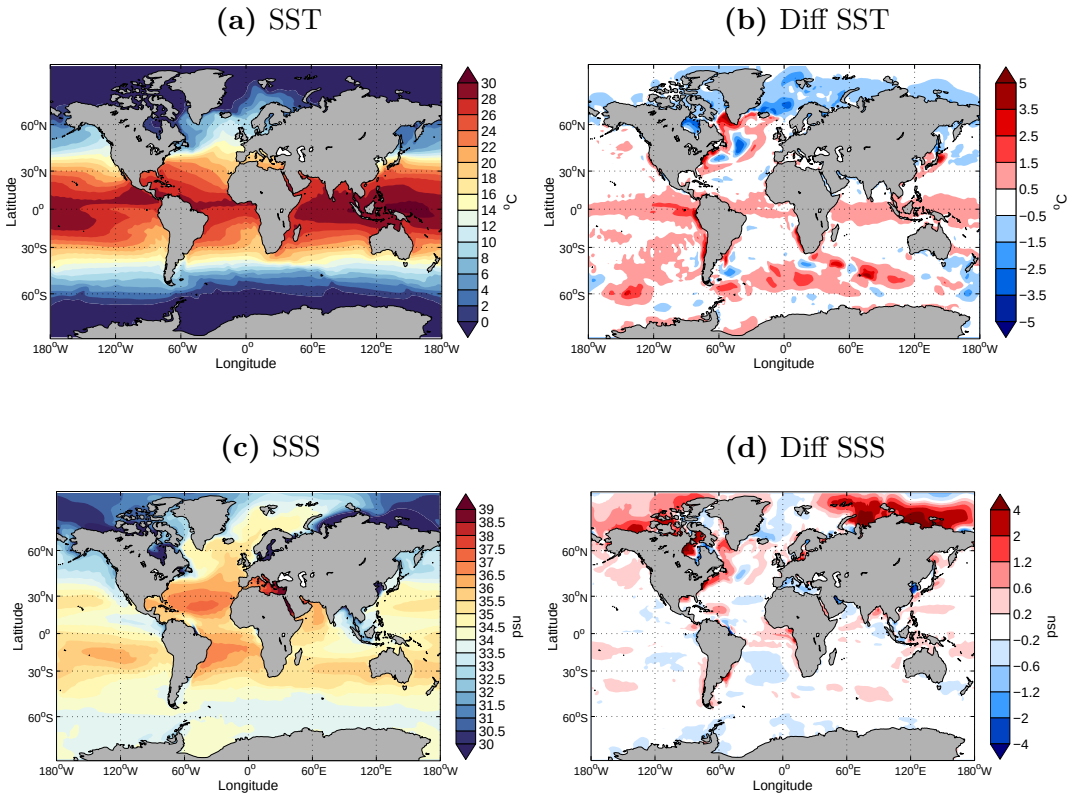

Figure 5.1: Modelled mean SST and SSS fields (left panels), and difference between simulated and observed (model minus observations) SST and SSS (right panels) based on the 1955–2006 climatology. The observational records are are provided from World Ocean Atlas 2009 and obtained from http://www.nodc.noaa.gov/OC5/WOA09/woa09data.html. Further discriptions are found in Locarnini et al. (2010) and Antonov et al. (2010) .

shallow shelf regions. Fresh biases are found in the Nordic Seas. High SST and SSS values are found along the western boundary of the North Atlantic, and Yanchun et al. (2014) argue that boundary currents may not be properly represented in coarse resolution models. They also state that due to the uncertainties in the atmospheric reanalysis products, the utility of these datasets are questionable close to coasts, particularly where large gradients in temperature are present.

Yanchun et al. (2014) compares the 20CR to the CORE-2 (Griffies et al., 2009; Danabasoglu et al., 2014*b*) simulation, the latter extending back to 1948. They find that regarding magnitude and spatial distributions, the two simulations of SST and SSS are generally comparable. Therefore, they argue that the results of the 20CR simulation are consistent to those of the CORE simulations (for the period after 1948).

5.1.2 Observed temperature South-West of Greenland

A long-term verification of the simulated temperature in the region of interest is provided by observed temperature from the Fylla Bank station 2 (Fylla2; see location in Figure 5.2 **b**) off the South-Western (SW) coast of Greenland, extending back to 1950 (Ribergaard, 2013). The time series has been extended further back, using SST anomalies from available observations in the area of SW Greenland (Smed, 1978). Data from overlapping periods show a high correlation ($r = 0.7$; Hanna et al., 2009), giving credence to the extended time series. Figure 5.2 **(a)** displays the normalised observed SST (at Fylla/Smed) from 1876 to 2009, together with normalised modelled SST at a grid cell nearby the Fylla2 station (64.5° N, 53.5° W). The mean observed SST is 0.85 °C and the mean modelled SST is 1.55 °C. The correlation between the two time series is $r = 0.34$. If a 5-yr running mean is applied to the time series, the correlation increases to $r = 0.58$. Although the mean modelled and measured temperature differs by 0.7 °C, the model simulation captures many of the inter-annual to decadal scale variations in the temperature time series. The amplitude of the variations in the observations are, however, somewhat larger, with a standard deviation of 1.1 °C compared to 0.60 °C in the model. After around 1990, the observations show increased temperatures, which is not captured in the model. Despite the latter period, Figure 5.2 shows that the simulated temperature in the northern part of the SPG shears many similarities with the constructed, observed temperature time series.

(a)

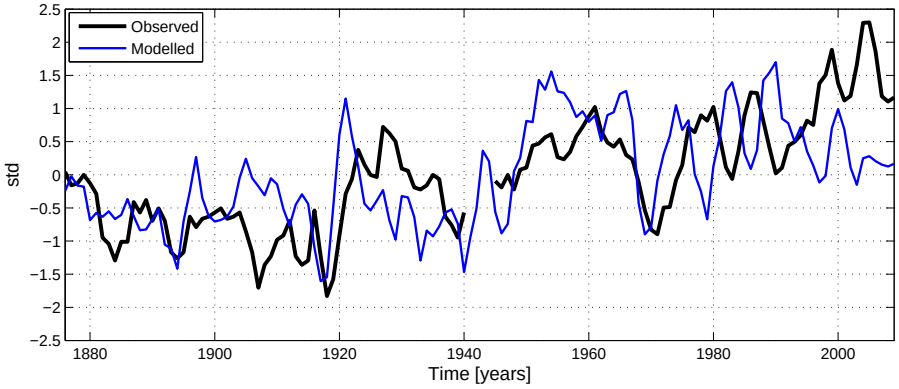

(b)

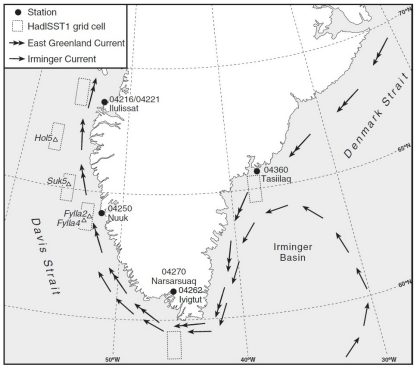

Figure 5.2: **(a)** Normalised anomalies of observed SST (Smed, 1978; Ribergaard, 2013) at Fylla2/Smed SW of Greenland (black line), and modelled SST anomalies (blue line) at a nearby grid cell to the Fylla2 station (64.5° N, 53.5° W), for the period 1876–2009. A 5-yr running mean is applied to the time series. The mean observed SST is 0.80 °C with a standard deviation of 1.1 °C, and the mean modelled SST is 1.56 °C with a standard deviation of 0.60 °C. The correlation between the modelled and observed temperature is $r = 0.34$. The correlation between the 5-yr smoothed lines is $r = 0.50$. **(b)** Map indicating the position of the Fylla2 station off the western coast of Greenland. The Figure is provided from Hanna et al. (2009), and produced by Paul Coles, University of Sheffield. Additional information about the observational record is found in Andresen et al. (2012)

5.1.3 Observed salinity in the Irminger Current

Observed 0–200 m salinity (S200) from a fixed station in the core of the Irminger Currrent (64.2° N, 27.57° W, see Hátún et al., 2005) is presented in Figure 5.3, together with modelled S200 at the same location, for the period 1971–2005. The mean observed (simulated) S200 is 35.07 psu (35.31 psu). Again, the model simulation captures large parts of the observed variability, and the correlation between the time series is $r = 0.64$. The typical amplitude of the variations in the observational record is, however, somewhat larger than the modelled, with a standard deviation of 0.043 psu for the observations compared to 0.031 psu for the simulation. The comparison suggests that the simulated 0–200 m salinity in Irminger Current is in general agreement with the observed salinity.

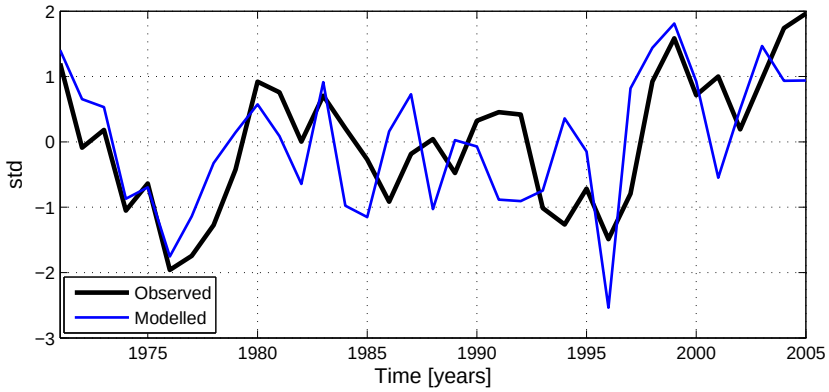

Figure 5.3: Normalised anomalies of observed S200 (Hátún et al., 2005) in the Irminger Current (64.2° N, 27.57° W, black line) and modelled S200 (blue line), for the period 1971–2005. The mean observed S200 is 35.07 psu with a standard deviation of 0.043 psu, and the mean modelled S200 is 35.31 psu with a standard deviation of 0.031 psu. The correlation between the time series is $r = 0.64$.

5.2 Temperature in the 1920s and 1990s

We have seen that the temperature in the North Atlantic SPG has experienced two periods of subsequent temperature decline and increase, one starting in the early 1920s and the other starting in the mid 1990s (Figure 4.4). The warming in the 1920s lasts until around 1940, with the most profound warming taking place in the 1920s. This is in agreement with surface marine observations from the Comprehensive Ocean-Atmosphere Data Set (COADS; Woodruff et al., 1987) presented in Fu et al. (1999). As evident in Figure 4.5, both T500 and S500 show an increase in the beginning of the 1920s. As argued by Müller et al.

(2014), lower salinity at higher latitudes prior to the 1920s is likely related to Arctic freshwater export. Different theories on the cause of the warming have been presented (e.g. Rogers, 1985; Fu et al., 1999; Bengtsson et al., 2004; Drinkwater, 2006), but, as mentioned in Chapter 1, most focus has been given to the mid 1990s warming.

In the mid 1990s, the SPG warmed significantly, as illustrated in Figure 4.4 and 4.5. Robson et al. (2012) found an increase in SST by about 1 °C in just 2 years in the North Atlantic SPG. The mid 1990s warming occurred more abruptly than that in the 1920s, but both periods have been characterised as a regime shift (Drinkwater, 2006; Alheit et al., 2014). As seen in Figure 4.5, both T500 and S500 increase rapidly after 1995/96. A high correlation between the T500 and S500 is found ($r = 0.88$) at one year lag, revealing a tendency of T to lead S. The high correlation between the two suggests advection to be an important contribution to the hydrographic changes in the SPG region.

In the following sections, the atmospheric forcing mechanisms (Section 5.3) and the ocean response to this forcing (Section 5.4) in the 1920s and 1990s, will be compared and discussed. As stated in Section 4.2, particular emphasis will be given to the preconditioning of the ocean. In Section 5.5 and 5.6, the warming and declining gyre circulation are discussed.

5.3 Atmospheric forcing

5.3.1 The North Atlantic Oscillation

The intensity of the NAO forcing influences both the buoyancy forcing and the wind stress curl in the SPG region (Häkkinen and Rhines, 2004). The warming of the SPG in both the 1920s and 1990s followed periods of fairly persistent positive NAO forcing (Figure 4.8). Consistent with the warming, it is proven for the 1990s warming and likely for the 1920s warming that a slowdown of the gyre circulation took place (Figure 4.4, Häkkinen and Rhines, 2004; Lohmann et al., 2009)

In both preconditioning periods, the Icelandic low is intense and has a northerly position centered at approximately 65° N (Figure 4.7 **a** and **c**). The strength of the pressure systems are especially prominent for the 1990s preconditioning phase. As explained in Section 2.2.2, a prolonged phase with NAO^+ forcing

will gradually make the European winters become milder, whereas cold north-westerly winds over the SPG region will cool the surface waters and enhance the buoyancy loss in the area (Section 2.2.2). During the warm periods (Figure 4.7 **b** and **d**), however, the pressure difference between the Icelandic low and the Azores high, and thereby the NAO index (Figure 4.8), weakens. For the 1920s warming (Figure 4.7 **b**), a south-westward shift in the position of the Icelandic low is found, consistent with observed SLP for the same period (Rogers, 1985). Rogers (1985) also report a weakening of the Azores-Iceland pressure gradient with about 5 hPa from 1925 into the 1930s and 1940s. The 20CR reanalysis fields suggest a weakening of about 3 hPa between the SLP gradient in the period 1920–1925 and the period 1926–1932. For the mid 1990s warming event, the shift in the NAO intensity, from extreme large values in the beginning of the 1990s to a low index in 1996 influences the climate in the North Atlantic (Häkkinen and Rhines, 2004).

Even though the Azores-Iceland pressure gradient is stronger in the preconditioning of the early 1990s compared to the early 1920s, it is found that the atmospheric pressure distribution prior to the two warming events share significant similarities.

5.3.2 Wind stress

The circulation of the SPG is related to the overlying cyclonic wind system, with westerlies to the south and a general tendency for easterlies to the north, as seen in Figure 4.9. In Section 4.2.3, the anomalous absolute wind stress distribution for the four periods were presented (Figure 4.10). The westerlies are stronger than normal in both of the preconditioning periods (Figure 4.10 **a** and **c**), and weaker in the following years (Figure 4.10 **b** and **d**), consistent with the SLP distribution. Rogers (1985) suggest that the shift in the position of the low in the period after 1925 may have been accompanied by an intensification of meridional flow originating from lower latitudes causing increased, southerly advection of warm air over Greenland and Baffin Bay. He further argues that this was the reason that the warming around Greenland started somewhat later (1926) than the more gradual warming of Europe, starting already in the mid 1890s. It should be noted that Rogers only analysed the changing atmospheric forcing in the 1920s–30s, with no attention to possible changes in the ocean circulation and the ocean heat content in the northern North Atlantic.

A possible reason for the weakening of the westerlies after the intense NAO winters of the two preconditioning periods may be related to the fact that high latitudes warmed more than lower latitudes. Fu et al. (1999) explains that in the late 1920s and into the 1930s (Figure 4.8), this caused a decrease in atmospheric baroclinicity, reducing the mean meridional thermal gradient, and thereby the geostrophic pressure gradient.

5.4 Ocean response

The variability of the circulation in the SPG can be linked, among other forcing mechanisms, to the NAO (Visbeck et al., 2003). Figure 5.4 **(a)** displays the SPG index (defined as SSH) together with the NAO index and the top 500 m temperature in the SPG. An indication of the gyre spin-up time scale is obtained by the time lag of maximum correlation between the NAO index and the gyre index (Figure 5.4 **b**), yielding 1 year (significant at the 95% significance level). A similar delayed response (1 year) was found in Bellucci et al. (2008), who correlated the NAO index to the barotropic streamfunction. As expected, the SSH correlates positively ($r = 0.65$) with T500 (higher temperature causes a higher SSH) and the maximum correlation is found at zero lag.

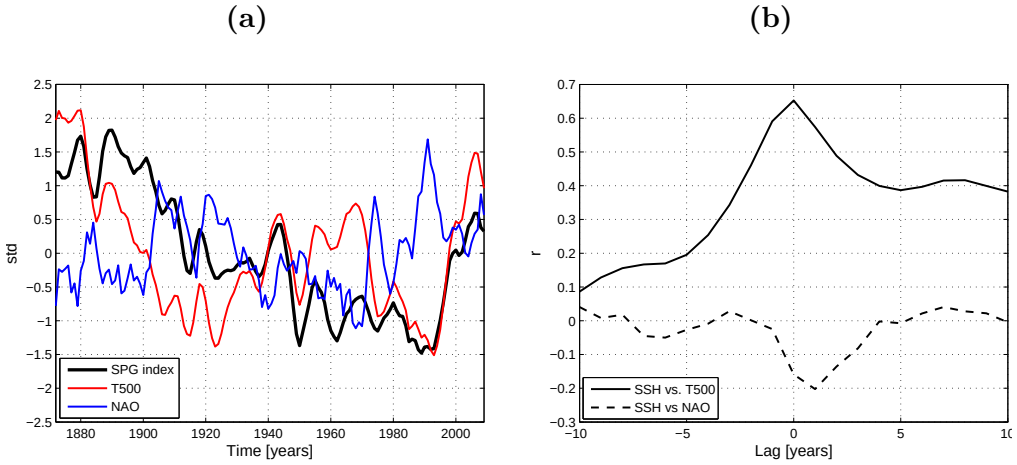

Figure 5.4: **(a)** The SPG index (defined as SSH, black line), T500 (red line), and the NAO index. A five year running mean and scaling by the associated standard deviations have been applied to all time series. The values are averages from Jul–Jun, where Jan indicates the year number. **(b)** Cross-correlation between the SPG index and T500 (solid line) and the NAO index (dashed line). Positive lag means that the corresponding variable is leading. Max correlation between the SPG index and T500 and the NAO index is 0.65 and -0.20, respectively. Both correlations are statistically significant.

5.4.1 NAO and the Gulf Stream

To investigate and emphasise the importance of the NAO on the large scale ocean dynamics, the Gulf Stream index (GSI; Taylor and Stephens, 1998) has been analyzed and compared to the NAO index. The Gulf Stream plays an important role in distributing heat in the Northern Hemisphere, thus it is important to understand the processes determining the mean path of the current. The GSI is a measure of the latitude of the 'north wall' of the Gulf Stream, a region recognised by a sharp fall in temperature. Since 1966, monthly charts of the path of the north wall of the Gulf Stream have been available from surface, aircraft and satellite observations. More information about the data can be found in Taylor and Stephens (1998).

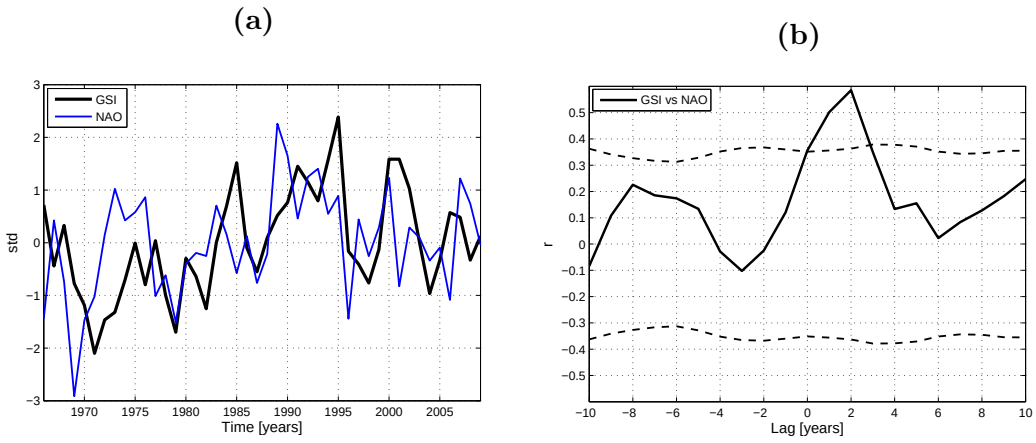

Figure 5.5: **(a)** Normalised anomalies of the GSI index (black line) and the NAO index (blue line), from 1966–2009. **(b)** Cross-correlation between the NAO index and the GSI. The NAO is leading, and the maximum correlation ($r = 0.59$) is found at two years lag. The dashed lines indicate the 95% significance thresholds. The number of degrees of freedom are adjusted at each lag, where auto-correlation has been accounted for.

Figure 5.5 **(a)** presents the GSI together with the NAO index from 1966 to 2009. The co-variability is evident, and the cross-correlation between the two time series (Figure 5.5 **b**) shows a value of $r = 0.59$, with a delay of about two years. This means that high values of the NAO index with a corresponding strengthening of the westerlies and trade winds, result in a more northerly path of the Gulf Stream about two years later. This is consistent with what was found in Taylor and Stephens (1998) who correlated the NAO index with the GSI from 1966 to 1996 and found a correlation of $r = 0.62$ at two years lag. An increase of the GSI until 1995 is seen, followed by a rapid drop from 1995 to 1997. This indicates that prior to the mid 1990s warming, the Gulf Stream

had an anomalously northward path. This was caused by the highly positive NAO forcing dominating the years from the late 1980s to the mid 1990s, and possibly the long-term, positive trend starting in the mid 1960s (Figure 4.8). In 1996, a sudden drop in the NAO index occurred, contributing to a more southward path of the Gulf Stream/North Atlantic Current.

The position of the Gulf Stream/North Atlantic Current system and by that the front between the subtropics and subpolar region, is determined by the region of zero Ekman pumping, i.e., where there is no wind-induced convergence or divergence of water in the upper surface layer (Taylor and Stephens, 1998). The anomalous Ekman pumping of the four investigated periods will be discussed in Section 5.4.3.

5.4.2 Initial cooling of the gyre

As mentioned in Section 5.3.1, under persistent NAO^+ forcing, strong, cold winds over the area leads to large heat loss from the ocean (see Figure 4.17 **a**), causing cooling of the surface waters by as much as several hundred Watts per square meter (Häkkinen and Rhines, 2004). Studies indicate that during several winters with NAO $^+$ forcing, the SPG will undergo an initial strengthening (e.g. Lohmann et al., 2008, 2009). It is found in Figure 4.16 (showing time series of the winter heat flux and the NAO index), that increased positive NAO forcing, corresponds to increased heat loss from the ocean. Especially in the period prior to the mid 1990s warming, large heat flux anomalies are found consistent with the highly positive NAO winters these years. From the late 1910s to the beginning of the 1920s, the heat loss also increased, but did not exceed the average value. This is probably due to the long-term, positive linear trend in the time series. However, prior to both warming events, the cooling leads to reduced surface buoyancy in the SPG area.

An initial cooling of the gyre can be seen in Figure 4.13 **(a)** and **(c)** (Section 4.3.2), displaying the thermal contribution to the steric height. Negative temperature anomalies are found in the SPG region during both preconditioning periods, due to the cooling associated with the positive NAO forcing. The initial cooling is also seen in the time series of SST variability in Figure 4.4 **(b)**. From the end of the 1910s to the beginning of the 1920s, a decrease in SST of about 0.9 °C is seen, and during the late 1980s to the beginning of the 1990s, the SST drops about 0.5 °C. This cooling leads to an initial strengthening of the gyre circulation (further discussed in Section 5.4.4).

5.4.3 Ekman pumping

In Section 4.3.1, the anomalous Ekman pumping before and during the warming were presented (Figure 4.12). In the two preconditioning periods, anomalously positive vertical velocities were found north of the zero-Ekman pumping zone, whereas negative anomalies were seen south of the zone. As explained in Chapter 2, this is a result of the positive NAO forcing dominating these periods, causing increased divergence in the subpolar region and increased convergence in the subtrobics, thus enhancing the climatological Ekman pumping.

Larger differences are found between the two warm periods (Figure 4.12 **b** and **d**). This is explained by differences in the mechanical wind forcing these periods (Figure 4.10 **b** and **d**) leading to differences in the ocean response. However, it is evident that similarities in the atmospheric forcing in the preconditioning of the warming events resulted in overall similar patterns of the Ekman pumping.

5.4.4 Deep winter mixing in the subpolar gyre

The reduced surface buoyancy in the SPG due to the cooling associated with the NAO^+ forcing, as seen in the preconditioning of the two warming events, will ultimately result in deep mixing and formation of intermediate to deep water masses (see Section 4.3.4). In addition, the enhanced upwelling (discussed in the previous section) of mid-depth waters in the interior of the basins will reduce the density difference between the surface and deeper layers, making the region more prone to deep convection (Yashayaev and Clarke, 2008, Section 2.3.7).

Deep mixing causes an increase in the volumes of the dynamically active layers in the SPG region (Figure 4.18). In the first part of the time series, until approximately 1945, only layer 31 and 32 are the most dynamically active layers. In the latter period, water dense enough to intrude layer 33 are produced, and layer 32 and 33 occupies the largest volumes in the gyre. However, as explained in Section 5.1, limited observational records makes it challenging to conclude whether this is a real change in nature, or a side effect of the quality of the reanalysis product or the applied OGCM.

The stratification just before deep mixing takes place (the preconditioning) determines the penetration depth of deep and convective surface mixing (Yashayaev and Clarke, 2008). A series of winters with formation of dens waters imply that the isopycnals raise and by that reduce their resistance to deep vertical mixing in the succeeding winter(s). As explained by Lohmann et al. (2008), the thickening of these intermediate layers and the raised isopycnals creates an upward doming density structure in the SPG, leading to the previously discussed initial strengthening of the gyre.

The years following 1900 are predominantly influenced by positive NAO forcing and includes four subsequent NAO^+ winters from 1920 (Figure 4.8). This may explain that layer 32 ($\sigma_2 = 36.789\ \mathrm{kg\,m^{-3}}$), experiences a large increase in volume starting from 1900, with a local maxima in the beginning of the 1920s. Between the mid 1980s and mid 1990s, the most exceptional event with deep mixing occurs (Figure 4.18), with dense water reaching layer 33 (Figure 4.18 **b**). This gives rise to a maximum occurrence of deep mixing throughout the integration in the mid 1990s. Yashayaev and Clarke (2008) argue that this increased convective production was caused by the severity of all the winters from the late 1980s.

5.4.5 Deep winter mixing in the Labrador Sea and Irminger Sea

Deep surface mixing in LS and in the IS were presented in Section 4.3.4 (Figure 4.19). As mentioned in Section 2.3.7, the LS is favorable of deep winter mixing and thus formation of the relatively dense LSW. Hydrographic observations indicate that surface waters in the region may become sufficiently dense to convectively mix to depths of 1500–2200 m (Yashayaev and Clarke, 2008). However, Bentsen et al. (2004) disagree with the classical picture that the IS is not a favourable location for deep convection, only the LS. They found convective mixing in both basins in their model study (using the MICOM OGCM), consistent with what is found here.

Time series of layer 32 and 33 in the LS and IS are presented in Figure 4.19 **(b)**, Section 4.3.4. It is evident both in the LS and IS, that the volume of layer 32 increases rapidly in the early 1920s. The rapid and large increase of layer 33 from the mid 1980s to to the mid 1990s is also found in both basins, but is most prominent in the LS. Yashayaev and Clarke (2008) states that the production of LSW in the mid 1990s was the coldest, densest, deepest, and volumetric

largest of their entire analyzed observational record covering the time period 1950–2007. As seen in Figure 4.19, deep mixing decays in both basins after 1996, in accordance with analyses of *in situ* data from the LS (Häkkinen and Rhines, 2004).

5.4.6 NAO and deep winter mixing

The cross-correlation between time series of the NAO index and the volumes of the intermediate layers provides information about the coupling between the atmosphere and ocean. Figure 5.6 **(a)** presents the NAO index and the time series of the volumes of layer 32 and 33 in the LS and in the IS. The cross-correlation between the NAO index and the layer volumes are presented in Figure 5.6 **(b)**. The time series are divided in two parts because of the transition in convective mixing prior to and after 1945. The deepest of the active layers has been chosen in the cross-correlation analysis, as these layers represent the most extreme mixing events. In the first period, large variability is found in layer 32, whereas in the latter period intermediate and deep water masses reach into the potential density value of layer 33. By dividing the time series in 1945, the short term variability is emphasised for both periods, without being influenced by the 1945 shift.

The largest correlations are found between the NAO and deep mixing in the LS (being statistically significant both prior to and after 1945, not shown). The correlations between the NAO and convection in the IS and the SPG area are, however, all below the 95% significance threshold (not shown), with the exception of layer 33 in the SPG region after 1945. Lu et al. (2007) used a coarse-resolution OGCM driven by surface forcing obtained from the NCAR/NCEP reanalysis, and found that changes in LSW properties could be explained by the winter NAO forcing. Similarly, Bentsen et al. (2004) argue that formation of LSW is tightly linked to the NAO forcing, but that a different forcing mechanism drives the convective mixing in the IS. They explain that a local increase of northerly winds associated with lower than normal SLP over the southern part of the Nordic Seas drives the convective mixing in the IS area.

The response of convection in the LS lags behind the NAO index by about 1–2 years (Figure 5.6 **b**). The positive correlation between the NAO index and layer 32 prior to 1945 indicates that for this period, a strengthened NAO index will cause a two year lagged increase of layer 32 in the LS. After 1945, enhanced

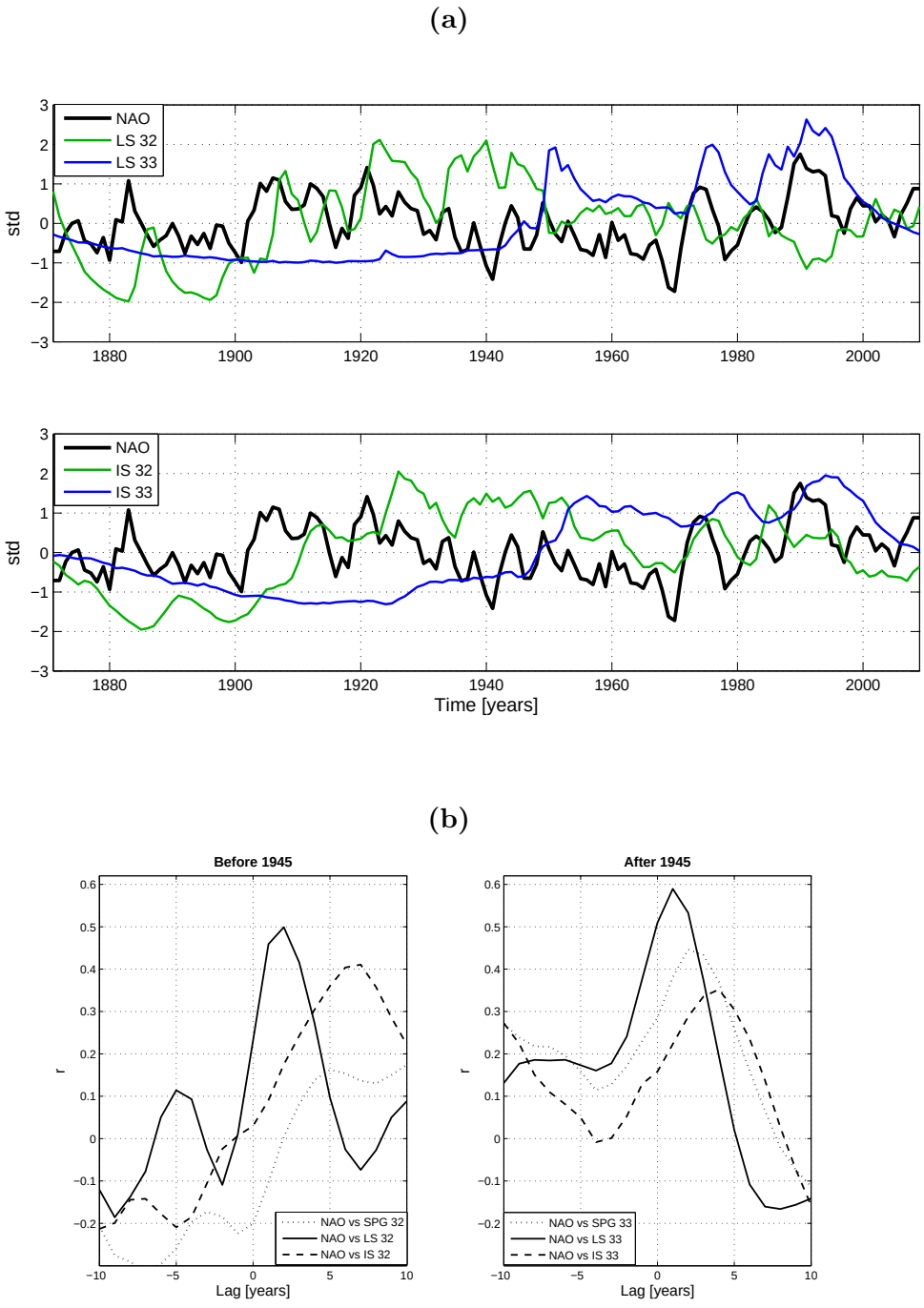

Figure 5.6: **(a)** Normalised anomalies of the NAO index (black line) and the volume of layer 32 (green line) and 33 (blue line) in the LS (top panel) and in the IS (lower panel). A 3-yr running mean is applied to the NAO time series. **(b)** Left panel shows the cross-correlations between the NAO index and the normalised (winter) volumes of layer 32 in the LS (solid line), the IS (dashed line) and the SPG (dotted line) for the period before 1945, when layer 33 is not active. Right panel displays the corresponding cross-correlations, but for layer 33 after 1945. Only the correlations between NAO and the layers in the LS (and between NAO and layer 33 in the SPG after 1945), are significant at the 95% significance level. Max correlation between NAO and layer 32 in the LS before 1945 ($r = 0.50$) occurs at two years lag and max correlation between NAO and layer 33 after 1945 ($r = 0.59$) occurs at one year lag. Correlations at positive lags means that the NAO is leading.

NAO forcing will increase the volume of layer 33 with a one year lag. Layer 32, however, correlates negatively with the NAO in this period (not shown). This implies that after 1945, strong positive NAO forcing leads to a transfer of water from layer 32 to layer 33. However, it should be noted that it is always an oversimplification to try to identify a 'normal' ocean response to an associated pattern of NAO forcing. Visbeck et al. (2003) argue that during years of positive NAO forcing, small shifts in the associated SLP pattern can locally cause large variations in the ocean response. An extended overview of different types of atmospheric circulation regimes in the North Atlantic and their influence on the ocean circulation is provided in (Barrier et al., 2013).

5.4.7 Atlantic Meridional Overturning Circulation

It is a well-established correspondence between formation of intermediate to deep water masses in the North Atlantic and the AMOC (Bentsen et al., 2004; Lohmann et al., 2008, 2009; Robson et al., 2012). In line with this, periods of positive NAO forcing and deep mixing will cause a strengthening of the overturning circulation. The latter occurs with a time lag as indicated in Figure 4.18 **(b)**, showing the cross-correlation between the strength of the AMOC and deep mixing. The changing sea water properties prior to and after the 1920s, and prior to and after the mid 1990s, imply considerable change in the SPG and subsequently in AMOC, as the latter is one of the major processes redistributing heat and salt in the North Atlantic (Bentsen et al., 2004). An acceleration of the AMOC typically increases the poleward heat transport (Robson et al., 2012), as seen in Figure 4.20 **(b)** and **(c)**, Section 4.3.5.

As described in Section 4.3.5, the AMOC undergoes a significant increase from the 1900s into the 1960s. Over this period, the AMOC at 45° N increases by about 3 Sv. This change is considerably larger than the typical variability of the time series (standard deviation of 1.6 Sv). A similar increase in the AMOC strength was found in the model study by Müller et al. (2014). They investigated the change in AMOC (at 45° N, 1000m depth) and found an increase of 3–4 Sv from 1880–1910 to 1930–1960. Müller et al. (2014) argue that the transition in AMOC strength is related to the applied atmospheric forcing. However, as argued in Section 5.1, the reliability of this increase is uncertain to to limited observational records.

Yanchun et al. (2014) compared the simulated AMOC from the dataset used

here to the CORE simulation (extending back to 1948, see Section 3.1.4), and found significant differences, especially in the 1950s–70s. They suggest that the difference originates from deviations in the wind field between the 20CRv2 and COREv2, affecting both the mechanical and the buoyancy forcing. However, by comparing the two simulations to observations (ICOADS; the International Comprehensive Ocean-Atmosphere Data), it is implied that the 20CRv2 dataset is relatively closer to the observations and that the simulated variations of AMOC in the 20CR simulations are possibly more reliable. However, this comparison/verification only extends back to 1948.

5.4.8 Deep mixing and AMOC

Since the convective mixing in the LS and the IS are hypothised to be driven by different forcing mechanisms (Section 5.4.4; Bentsen et al., 2004), they may act together and enhance the strength of the AMOC or act oppositely to reduce the net overturning strength. Therefore, the formation of intermediate and deep water masses throughout the SPG region, which includes both the LS and IS, have been cross-correlated with the AMOC (Figure 5.7 **b**). Again, the time series are divided in two parts, prior to and after 1945. The left panel shows the cross-correlation between AMOC at 26.5° N and at 45.0° N and layer 32 before 1945. The right panel displays the corresponding cross-correlations between AMOC and layer 33 after 1945, when layer 33 becomes active.

The highest correlations are found prior to 1945, with a maximum correlation between AMOC at 45° N and layer 32 at zero lag ($r = 0.70$). AMOC at 26.5° N lags behind the volume of the intermediate layer with about 0–2.5 years. Both correlations are statistically significant at the 95% significance level. After 1945, correlations at similar lags are found, but with correlation values considerably smaller than those in the first period. However, the correlation with AMOC at 45.0° N is statistically significant, indicating that input of water into this layer will enhance the AMOC. The difference in correlation between the two time periods could be linked to the long-term weakening and subsequent strengthening of both AMOC and the thickness of layer 32 prior to 1945. The time series show weaker long-term variations after 1945. In addition, the contribution of convectively mixed water masses into layer 32, is not included in the correlations after 1945. Summing up the contributions from the different layers, reduces the short term variability. Bentsen et al. (2004) correlated the AMOC with the convective mixing in the LS and IS, and found a delayed intensification of the AMOC after 0–5 years, which is comparable to what is found here.

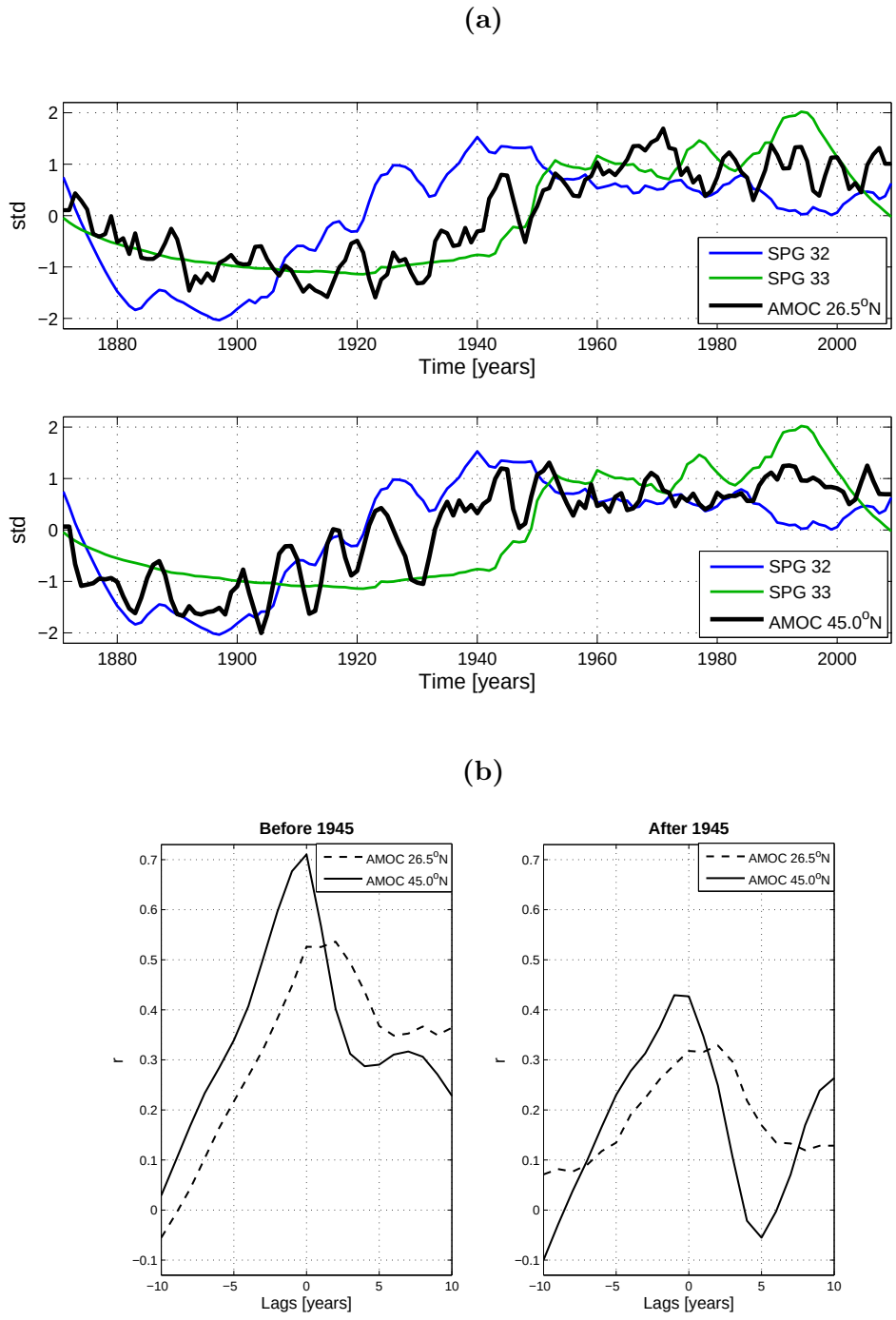

Figure 5.7: **(a)** Winter (djfm) normalised volume anomalies in the SPG and maximum AMOC at 45.0°N (top panel) and maximum AMOC at 26.5°N (lower panel). A 3-yr running mean is applied to the AMOC time series, and the yearly averages are from Jul to Jun, where Jan indicates the year number. **(b)** Left panel displays the cross-correlation between layer 32 in the SPG and AMOC at 45.0° N (solid line) and AMOC at 26.5° N (dashed line) for the period before 1945. Right panel is as the left one, but compares the AMOC time series and layer 33 after 1945. Positive lags means that the convection is leading. All correlations are statistically significant (not shown), except AMOC at 26.5° N and layer 33, after 1945. Max correlation between the layers and AMOC at 45.0° N is found at zero lag, whereas max correlation between AMOC at 26.5° N and the layers is found at 0–2.5 years lag.

This analysis implies that a strengthening of the AMOC requires surface waters with sufficiently high density to intrude layer 32 and 33. As previously discussed, densification of the surface waters in the SPG region is a response of positive NAO forcing, through cooling and reduced buoyancy. It should be mentioned that other source waters for the AMOC, like the overflow waters across the Greenland-Scotland Ridge may, in addition, contribute to the AMOC. However, this contribution is typically on longer time scales than for the water mass transformation in the LS and IS (Olsen et al., 2008).

5.4.9 Short summary

The atmospheric forcing in the 1920s and 1990s and the ocean's response to this forcing have been discussed in the previous sections. The main focus has been given to the preconditioning of the ocean prior to the two warming events. In the following sections, the warm periods, including the decline in circulation strength are discussed.

Before continuing, the main findings so far can be summarised as follows: Similarities in the preconditioning of the ocean for the two warming events are found, albeit not identical. Both preconditioning phases were dominated by prolonged periods of positive NAO forcing (Figure 4.8). Enhanced Icelandic low and Azores' high (Figure 4.7) caused a strengthening of the prevailing westerlies (Figure 4.10), leading to cooling in the SPG-region and warmer conditions in the eastern parts of the North Atlantic. The negative buoyancy forcing in the SPG region (Figures 4.16 and 4.17) leads to increased formation of intermediate to deep water masses (Figure 4.18 and 4.19), and to an initial strengthening of the gyre (e.g. Figure 4.13 **a** and **c**). In addition, increased Ekman transport causes anomalous upwelling in the SPG-region during both preconditioning periods (Figure 4.12), contributing to reducing the stratification, thus making the region more susceptible to deep mixing (Figure 4.12). In the beginning of the 1920s, these factors enhances production of water masses entering layer 32, whereas in the 1990s, surface water masses becomes sufficiently dense to intrude layer 33. As discussed in the previous section, this enhanced water mass formation leads to a spin-up of the AMOC (being more pronounced at 45.0° N than at 26.5° N). For both periods, the max correlation with AMOC at 45.0° N is found at zero lag, whereas correlation with AMOC at 26.5° N is found with a delay of 0–2.5 years.

5.5 The mid 1920s and mid 1990s regime shifts

Dynamic variations in the gyre circulation strength are expected on a variety of time scales in response to changes in the NAO, but the prime driver for variability in the SPG circulation is uncertain (Robson et al., 2012). However, recent findings suggest that variations in the heat flux (buoyancy forcing) and the wind stress curl over the northeastern North Atlantic are main factors for the variability in the SPG (e.g. Häkkinen and Rhines, 2004; Lohmann et al., 2009). The warm periods, including the decline in the SPG circulation, are discussed in the following sections.

Influence of variations in the wind forcing

NAO^- forcing will contribute to increase the temperature in the SPG region through reduced ocean heat loss in winter (see Figure 4.16 and Section 2.3.3). After the late 1920s and since the mid 1990s, the NAO has been largely neutral (Figure 4.8 **b**), hence the warming of the SPG could potentially be explained by a reduction in the NAO index. Studies by e.g. Herbaut and Houssais (2009) and Häkkinen et al. (2011) suggest that variations in the wind forcing dominates changes in the eastern SPG. Robson et al. (2012) argue, however, that for the mid 1990s warming and collapse in gyre circulation, the wind forcing only accelerated the change, but was not the primary cause.

In addition to the reduced ocean heat loss, NAO^- forcing will cause a sudden reduction in the southward Ekman transport between ∼30–60° N, contributing to a positive anomaly in the poleward branch of the AMOC and the MHT. Robson et al. (2012) found a surge in MHT after the drop in the NAO in 1995/96, but argue that this did not overcome the enhanced MHT due to the preceding buoyancy forced deep convection associated with winters with NAO^+ forcing. To investigate whether the warming was a direct response to the NAO or a delayed response of the ocean preconditioning, sensitivity experiments have been performed in which the atmospheric forcing is changed to (predominantly) NAO^- conditions in 1920 and 1990, respectively. These experiments are presented in Section 5.6.

Influence of dynamical changes in the ocean

The preconditioning of the ocean may have contributed to the warming and weakening of the gyre circulation starting in the mid 1920s and the mid 1990s,

with the latter change being the most prominent. A spin-up of the AMOC, as discussed in Section 5.4.8, is hypothised to result in increased advection of warm and saline water from the STG towards the eastern rim of the SPG region (Lohmann et al., 2008). Enhanced inflow of warm waters will counteract the effect of local buoyancy forcing, thus reducing the formation of intermediate and deep waters, and hence the gyre circulation strength.

A strengthening of the AMOC at 26.5° N, starting in the beginning of the 1920s, is seen in e.g. Figure 5.7. Due to the time lag between deep mixing and AMOC, this may have been a delayed response of the prolonged NAO^+ forcing dominating the beginning of the 1900s and 1910s. From the late 1980s, an enhancement in the AMOC strength is also found (Figure 5.7). More extreme events of deep winter mixing occurs in the 1980s, reaching a maximum value in the mid 1990s. As previously argued, this is likely caused by the positive NAO forcing following the winter of 1989 (Figure 4.8; Yashayaev and Clarke, 2008). Evidence of advective signals for both warming periods were provided in Section 4.3.2, where the thermal and haline contributions to steric height for the warm periods were presented (Figure 4.13 and Figure 4.14 **b** and **d**). These figures show positive anomalies in thermosteric height due to increased temperatures in the SPG region, as well as decreased halosteric heights due to increased salinity in the area (note the negative sign in the haline contribution to steric height). The analysis by e.g. Häkkinen and Rhines (2004), Lohmann et al. (2009), and Robson et al. (2012) suggest that it was the resulting enhanced AMOC strength and the corresponding enhanced MHT that was the primary reason for the warming of the SPG in the mid 1990s.

It is indicated that the weakening of the gyre in both periods followed a decay in the domed structure of the isopycnals in the SPG, caused by a decrease in the volume of the intermediate layers. Layer 32 experiences a large decrease in volume in the mid 1920s in the SPG region, and after the mid 1990s, a rapid decrease of layer 33 is found (Figures 5.6 **a** and 5.7 **a**). In both cases, this is assumed to be a delayed response to the shift from prevailing NAO^+ winters to a NAO^- winter, and the associated enhanced inflow of waters of subtropical origin. The following section presents model sensitivity experiments, to further investigate the importance of the atmospheric forcing before and during the two events.

5.6 The response of the SPG to a different atmospheric forcing

The ocean sensitivity to variations in the atmospheric forcing, or the role the ocean initial conditions may have on the evolution of the ocean state, can be addressed by performing idealised sensitivity experiments. The variability or strength of certain fluxes (e.g. wind and buoyancy) can selectively be altered or turned off, and the result can be compared to the original run to identify the influence of the individual forcing components. To investigate the significance of the atmospheric forcing during the two warming events, sensitivity experiments have been performed for the periods 1920–1932 and 1990–2002. During the experiments, the ocean is forced by the atmospheric state from 1955–1967 which is dominated by NAO^- conditions (see Figure 4.8). First, sensitivity experiments for the two periods were performed with the initial ocean states extracted from the original model run in 1919 and 1989, respectively. These integrations are in the following named the Early Warming Experiment 1 (EWE1) and the Recent Warming Experiment 1 (RWE1), respectively. Starting from the end state of the EWE1 and RWE1 these experiments were rerun and are called EWE2 and RWE2, respectively. See Figure 5.8 for the experimental design.

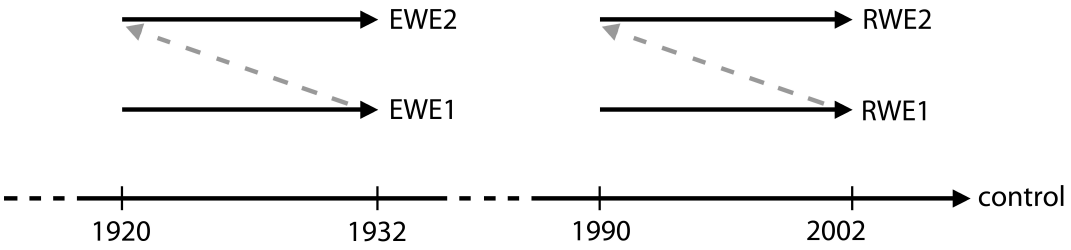

Figure 5.8: Experimental design. The initial condition in EWE1 and RWE1 is extracted from the control run (1919 and 1989, respectively). The end state of the EWE1 and RWE1 is the initial condition in EWE2 and RWE2, respectively.

An asymmetric SPG response to the sign of persistent NAO forcing has been suggested (e.g. Lohmann et al., 2008; Robson et al., 2012). As explained in Lohmann et al. (2008), subsequent winters with NAO^+ forcing may involve a reversal of the circulation strength of the SPG: First, the gyre is initially strengthened due to the strong loss of surface buoyancy. After a few years, deep mixing leads to an intensification of AMOC, and by that a strengthening of poleward advection of warm and saline surface waters of subtropical origin. These processes were discussed in Section 5.4.8. The advective heat input may

be sufficiently large to overcome the buoyancy loss in winter to generate dense surface waters, thus the SPG circulation strength is reduced. With a persistent negative NAO forcing, however, a gradual warming and weakening of the SPG is expected (Barrier et al., 2013), with no reversal of the gyre circulation strength. In this case, both the heat flux and the wind stress curl over the northern North Atlantic will act to weaken the SPG (Lohmann et al., 2009).

5.6.1 Temporal evolution of the subpolar gyre

Figure 5.9 presents main, integrated results from the sensitivity runs: The anomalous gyre strength (represented by SSH), T500, and S500 in the SPG, together with the control run (black line). EWE1 and RWE1 are presented with red solid lines, and EWE2 and RWE2 in red dashed lines. The initial condition for the experiments is also included in the sensitivity time series.

The simulated SPG index (SSH) for RWE1 (Figure 5.9 **a**) reveals a rapid increase during the first two years of integration, indicating a sudden slowdown of the gyre circulation. This slowdown is comparable to that of the control run starting in 1995. In RWE1, a similar rapid increase is found in T500 (Figure 5.9 **b**) and S500 (Figure 5.9 **c**), the latter increase starting after the first year of integration. Such a rapid increase in SSH, T500 and S500 is not, however, found in EWE1. Since the atmospheric forcing in the two experiments (EWE1 and RWE1) are identical, the different SPG responses indicate a significant role of the ocean initial states. In addition, this initial increase is not found in RWE2 (where the initial condition is the end state of RWE1), supporting the claimed importance of a preconditioning phase. To further investigate the rapid change during the first years of integration in RWE1, the distributions of T500 and S500 for the years 1990–1993 are presented in Figure 5.11 and 5.12, respectively. Positive T500 and S500 anomalies appear in the eastern part of the SPG region in 1990, being amplified until 1993. Large scale, spatial co-variability in T500 and S500 along the main path of the Gulf Stream/the North Atlantic Current and in the SPG region indicates an advective signal, i.e. enhanced inflow of warm, saline waters of subtropical origin.

After the second year of integration, the year-to-year variability in SSH is similar across all sensitivity experiments (Figure 5.9). The gyre strengthens until 1927 (EWE)/1997 (RWE), the year corresponding to the forcing field of 1962. Thereafter, a slow weakening of the gyre throughout the integration is found

(a) SSH

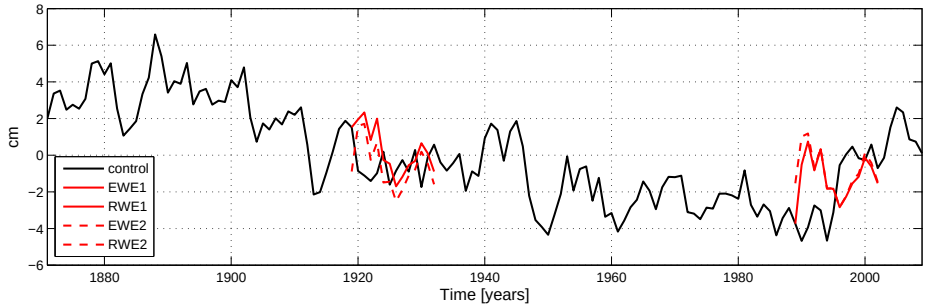

(b) T500

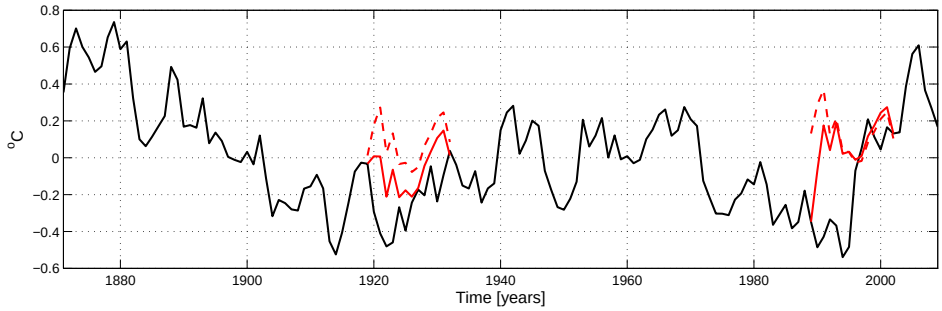

(c) S500

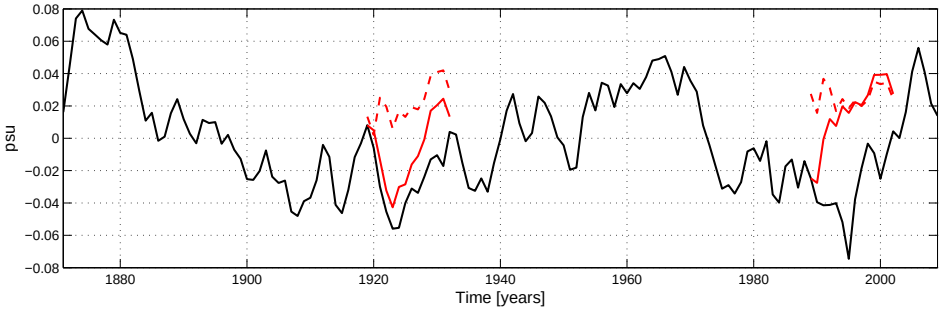

Figure 5.9: **(a)** SSH anomalies from the control integration (black), EWE1 (red, solid line), RWE1 (red, solid line), EWE2 (red, dashed line) and RWE2 (red, dashed line) averaged over the SPG. The time series are relative to the mean of the control run. **(b)** and **(c)** Same as **(a)**, but for T500 and S500, respectively.

for all experiments. In Figure 5.10, the normalised anomalies of the gyre index (note that the sign is reversed) for all four experiments, are presented together with the corresponding NAO index for the applied forcing period (1955–1967). Co-variability between the NAO index and the variability in SSH is evident, with an indication of a one year lagged response in the SSH after a change in the NAO. Therefore, the weak strengthening starting after the second integration year in all experiments, may partly be explained by winters with NAO^+ forcing in the atmospheric field (1957, 1959 and 1961). The five subsequent years with NAO^- forcing from 1962, causes a gradual weakening of the gyre.

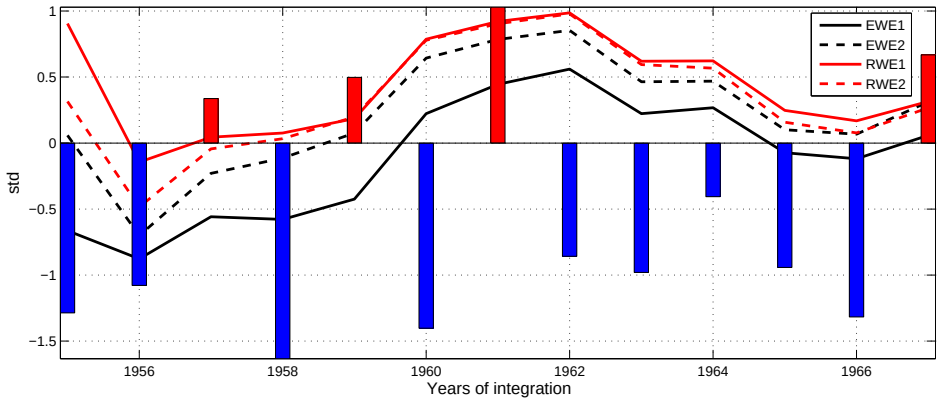

Figure 5.10: Normalised anomalies of the gyre index from EWE1 (black, solid line), EWE2 (black, dashed line), RWE1 (red, solid line) and RWE2 (black, dashed line). The anomalies are averaged form Jul–Jun, and scaled by the standard deviation of the control run. To ease visual inspection, the sign has been reversed in the time series. The bars show the NAO index for the forcing period 1955–1967.

Except the first two years in RWE1, the variability in T500 also evolves similarly in all experiments, especially the evolution in EWE2 and RWE2. Similarities between EWE2 and RWE2 are expected, since the atmospheric forcing during the preconditioning, as well as during the experiments, are identical for the two experiments. Cooling until integration year 6 (1925/1995) is in accordance with the NAO index and the strengthening of the gyre circulation (Figure 5.9 **a**), and the following warming is in accordance with a weakening of the circulation strength. Larger differences are found in S500 between EWE1 and RWE1. In EWE1, a rapid freshening during the first 3 years is found, similar to that for the control run. This indicates a freshwater source independent of the applied atmospheric forcing. To detect this freshwater source, the S500 distribution have been examined for the first 4 years of integration (not shown), indicating advective input of fresh water along both coasts of South Greenland. The S500

in EWE2 does not contain an initial freshening, and evolves similarly to the RWE2. The mean T500 and S500 distributions prior to and during the two warming events for the control run and the first sensitivity experiment (EWE1 and RWE1), are presented in the appendix (Figures A.1 and A.2). The difference between the control integration and the experiments is also included, revealing especially large values for the 1990–1995 period.

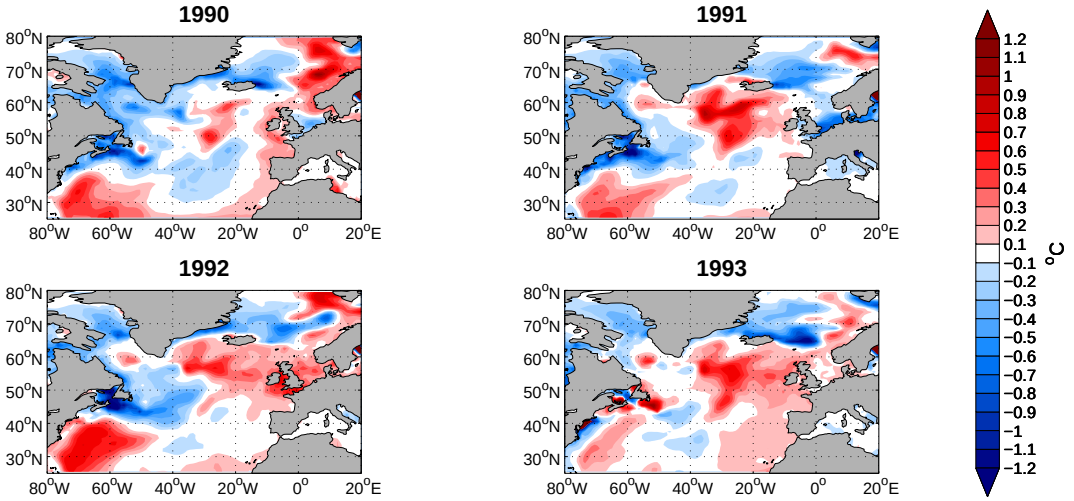

Figure 5.11: T500 anomalies for the years 1990–1993 for RWE1. The anomalies are relative to the mean of the control run.

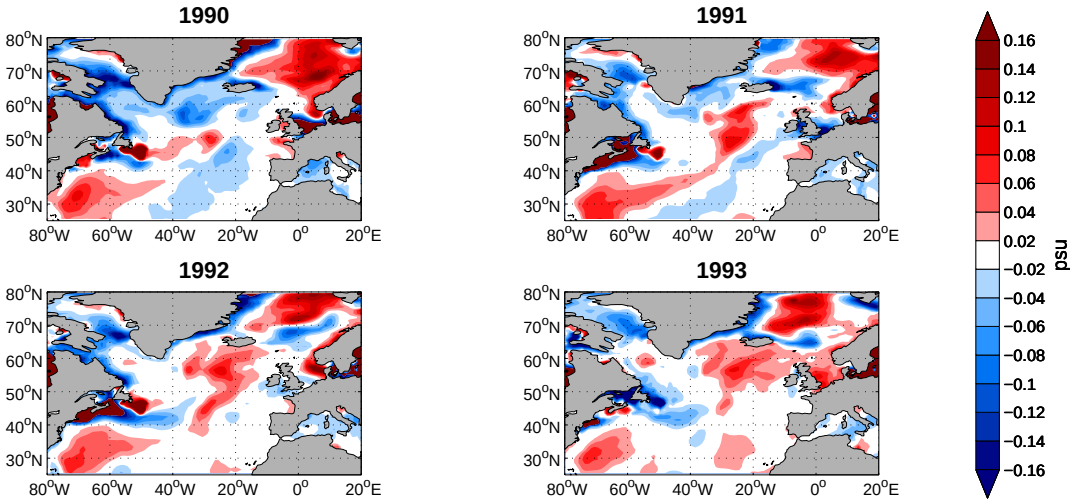

Figure 5.12: Same as Figure 5.11, but for S500.

5.6.2 Atlantic Meridional Overturning Circulation

The anomalous AMOC strength at 26.5° N is presented in Figure 5.13 **(a)**. To obtain a direct comparison of the AMOC responses among the different experiments, all time series are plotted together as anomalies relative to their initial value in Figure 5.13 **(b)**. The year-to-year variability shares similarities for all experiments. The negative peak anomaly in integration year 4 (forcing field of 1958) may be associated with a change in the Ekman transport since the anomaly is particularly profound, it is found in all experiments and the NAO index is largely negative this year (see Figure 5.10). As explained in Section 2.3.3, negative NAO forcing will result in a weakening of the northward Ekman transport south of about 30° N, thus weakening the AMOC at 26.5° N. Oppositely, north of about 30° N, a strengthening in the AMOC due to a weakening of the southward Ekman transport is expected. The AMOC strength at 45.0° N reveals positive peak anomalies in integration year 4 for all experiments (not shown), in support of an Ekman induced contribution.

(a) AMOC 26.5° N

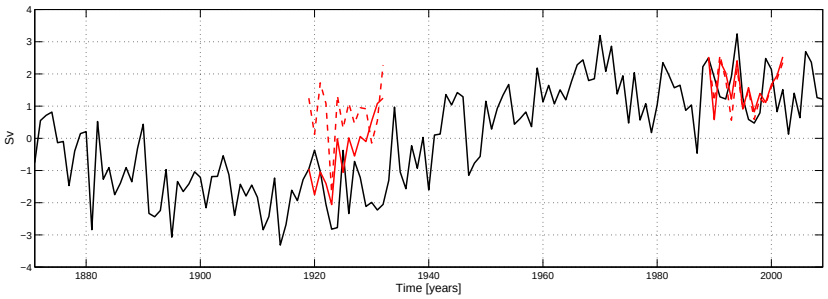

(b) AMOC 26.5° N

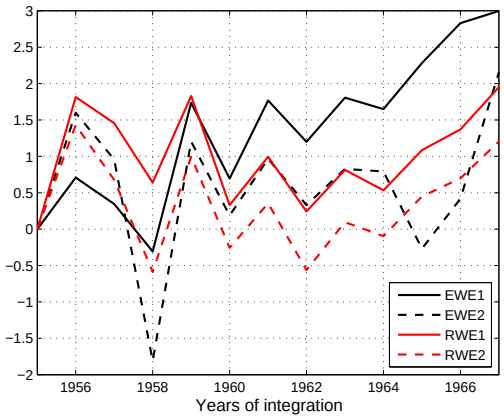

Figure 5.13: **(a)** Same as Figure 5.9, but for the AMOC strength at 26.5° N. **(b)** All experiments are plotted together as anomalies relative to their initial value. The anomalies are averages from Jul-Jun, where Jan indicates the year number.

As previously mentioned, in the case of NAO^- forcing, a steady decrease in AMOC strength is expected with a time lag of a few years. In the EWE1, however, a steady increase in the AMOC strength of 2–3 Sv is instead found. The strengthening of the gyre circulation (Figure 5.9 **a**) during the first years of integration, may have been enough to cause a delayed strengthening of the AMOC at lower latitudes. The initial strengthening may, similarly, be a delayed response to the positive NAO forcing dominating prior to the switch in atmospheric forcing. This long-term increase is not prominent in the RWE1 integration. This may be explained by the initial strength of the AMOC, being much stronger in the latter period (over 2 Sv above average) than the earlier period (1.5 Sv below average). Due to the strong AMOC in the 1990s (Figure 4.20 **a**), the AMOC may already have been close to (or at) it's maximum value, possibly prohibiting further increase.

5.6.3 The initial gyre response

The conducted sensitivity experiments suggest that a change in the atmospheric forcing to (predominantly) NAO^- conditions in 1920 and 1990 will result in a sudden slowdown of the gyre circulation in the beginning of the 1990s period, but not in the 1920s period. The different initial gyre response in the two periods indicate differences in the ocean preconditioning of the two periods. Therefore, the strong weakening of the SPG in the RWE1 might not be explained by the actual atmospheric forcing alone. In 1990, the gyre appears to be sufficiently strong and developed, so that a change in the atmospheric forcing field may results in a collapse, similar to that in 1995 of the control run. It is evident from the SPG index (Figure 5.9 **a**) that the gyre was significantly stronger in 1990 (-3.5 cm) compare to in 1920 (1.9 cm).

Deep winter mixing associated with a strong gyre will cause a lagged increase of the AMOC strength. The latter is seen in the control run in Figure 5.13 **(a)**, revealing an ongoing strengthening in the AMOC (3 Sv) starting in the end of the 1980s and lasting until the beginning of the RWE1. Eden and Willebrand (2001) further explains that during phases with low NAO, the ocean response is a cyclonic circulation anomaly centred at the subpolar front, which may lead to the mixing of warm and salty water across the front in the eastern part of the gyre. The result of the strengthened AMOC and the NAO^- induced wind stress curl is enhanced inflow of warm, saline waters as seen in Figures 5.11 and 5.12. Deep mixing withing the SPG region decreases due to both weak-

ened air-sea buoyancy forcing by the negative NAO forcing and the enhanced inflow of warm subtropical waters (Häkkinen and Rhines, 2004; Lohmann et al., 2009). The reduced deep mixing weakens the doming structure of the subpolar isopycnals, thus reducing the geostrophic flow in the SPG region. These factors may be responsible for the sudden (simulated) slowdown of the gyre circulation in RWE1. In the 1920s period, the preconditioning was not sufficient to govern a similar collapse.

A collapse in the gyre circulation already in 1990 is opposing the results in Lohmann et al. (2009) who did a similar, albeit not identical experiment. Lohmann et al. (2009) used the post 1995 atmospheric forcing on the ocean initial condition in years both prior to and after 1995. They found that the preconditioning of the ocean in 1994 (but not for the preceding years) was sufficient to govern a similar collapse of the gyre circulation as the one in 1995. It is difficult to conclude whether the response in nature had been similar to those in the experiments presented here, with a change in the NAO forcing in 1920/1990. However, model verifications presented in Section 5.1 show that the model captures large parts of the variability in the presented observations, in support of the reliability in the experiments.

5.7 Future perspectives

To further investigate the importance of the ocean initial state in the mid 1920s and in the mid 1990s for the weakening of the SPG, valuable insight would likely be obtained from a series of sensitivity experiments. First of all, the type of sensitivity experiments done by Lohmann et al. (2009) should be repeated, particularly the experiments in which the post 1995-forcing was run from the (1st July) ocean states for the years 1900–1994. For the 1920 warming, the 1989–1995 forcing (positive NAO winters) could also be applied to the ocean initial states during the period 1915–1925 to examine the (possible) uniqueness to the 1990s warming. Also the change in SSH and BSF (Figure 4.4) between 1938–1946 would be interesting to examine. The influence of changes in the fresh water budget (precipitation, evaporation, river runoff) should also be included in a more thorough analysis. Related to this, the rapid fresh water anomalies depicted in Figure 4.5 should be examined, particularly the formation, propagation and decay of these (e.g., Sundby and Drinkwater, 2007; Glessmer et al., 2014). See also the end paragraphs in the Summary chapter.

Chapter 6

Summary

In this thesis, possible mechanisms responsible for the warming and weakening of the North Atlantic SPG in the mid 1920s and mid 1990s have been investigated by analysing output from a state-of-the-art OGCM. For this, a control integration covering the time period 1871–2009 is used. In addition, sensitivity experiments have been run in order to examine the role of the atmospheric forcing for the two warming events. The main findings are as follows:

- The atmospheric forcing prior to the two warming events share similarities: Both are characterised by positive NAO forcing and by that cooling of the surface waters, plus an anomalous upwelling caused by Ekman transport. This, in turn, increases the formation rate of intermediate to deep water masses. The net effect is a lowering of the sea surface height, upward dooming of the sub-surface ispopycnals, and a strengthening of the SPG circulation

- The production of intermediate and deep waters in the SPG region lead to a lagged (some years) intensification of AMOC. The latter is associated with enhanced, simultaneous poleward transport of heat and salt in the upper portion of the water column by the Gulf Stream/North Atlantic Current.

- The additional heat transported by the Gulf Stream/North Atlantic Current into the SPG region tends to oppose the ocean cooling induced by positive NAO forcing. The result is reduced formation of intermediate and deep waters. If, in addition, the atmospheric state switches from positive to negative NAO, also the atmospheric forcing contributes to reduce water transformation rates in the SPG. The net effect is that the SPG weakens, becomes warmer, and the SSH increases.

- The preconditioning of the two warming periods differs in the following ways: Prior to the mid 1990s warming, the SLP gradient over the North Atlantic was anomalously large as a result of several, highly positive NAO winters. The density of the transformed water masses was unprecedentedly high, leading to an anomalously strong gyre circulation. The situation prior to the 1920s warming was less dramatic.

- The 1990s warming, caused by both advection of warm surface waters and a sudden shift in the NAO forcing during the winter 1995/96, lead to an abrupt and strong warming in the SPG region. In comparison, the 1920s warming occurred more gradual.

- By artificially changing the atmospheric forcing to (predominantly) negative NAO forcing from and including 1920 and 1990, the gyre responses for the two periods were significantly different. It is found that negative NAO forcing is important for the onset of the warming, but that the ocean preconditioning determines the magnitude of the shift in the ocean climate in the SPG region. In 1990–91, the response was similar to that in 1995, with a sudden slowdown, warming and salinification of the SPG. This collapse of the SPG was not seen for the 1920s period, indicating differences in the two ocean preconditioning states.

- It can be concluded that the preconditioning of the ocean was essential for the observed warming and decline in SPG circulation in the mid 1920s and mid 1990s. More specifically, the two events can partly be explained as delayed responses to prolonged phases with positive NAO forcing, in combination with the reduced NAO forcing following from the mid 1920s and the mid 1990s.

The above findings are based on analysis of one OGCM forced with observation-based atmospheric reanalysis fields. It is demonstrated that the OGCM simulates several features of the ocean hydrography in the region of interest. Likewise, the reanalysis compares well with available observations (although deviations exist as shown by comparison with satellite-based observations). Nevertheless, neither the OGCM nor the reanalysis fields represent nature in all aspects. This is particularly the case during the first half of the integration period due to the sparseness of available observations.

Appendix A

Supplementary figures

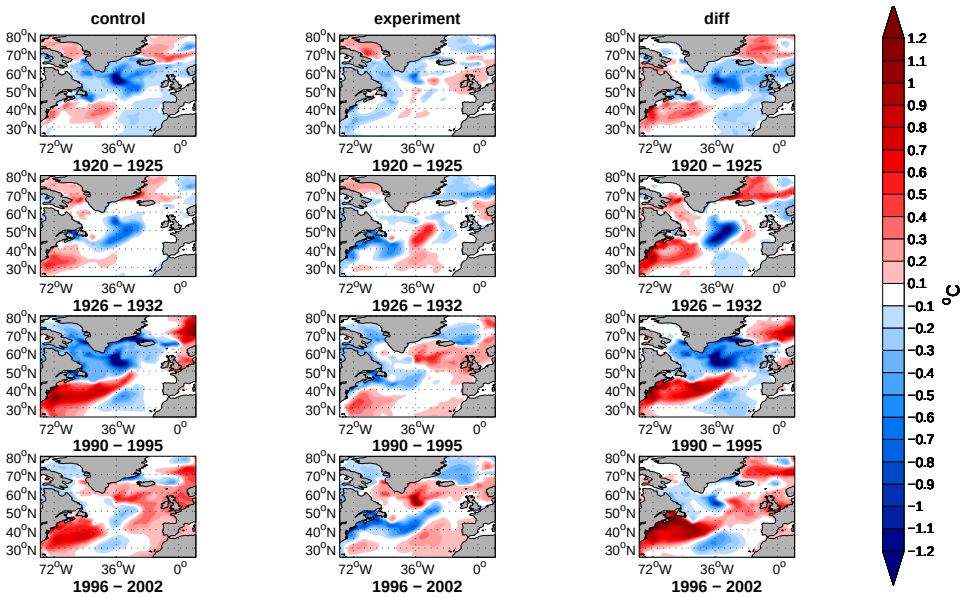

Figure A.1: T500 anomalies for the control run (left panels), EWE1 and RWE1 (middle panels) and the difference, control−sensitivity (right panels). The anomalies are relative to the mean of the control run. Each row represents one of the four periods, indicated under the panel. See Section 5.6. for additional information about the sensitivity experiments.

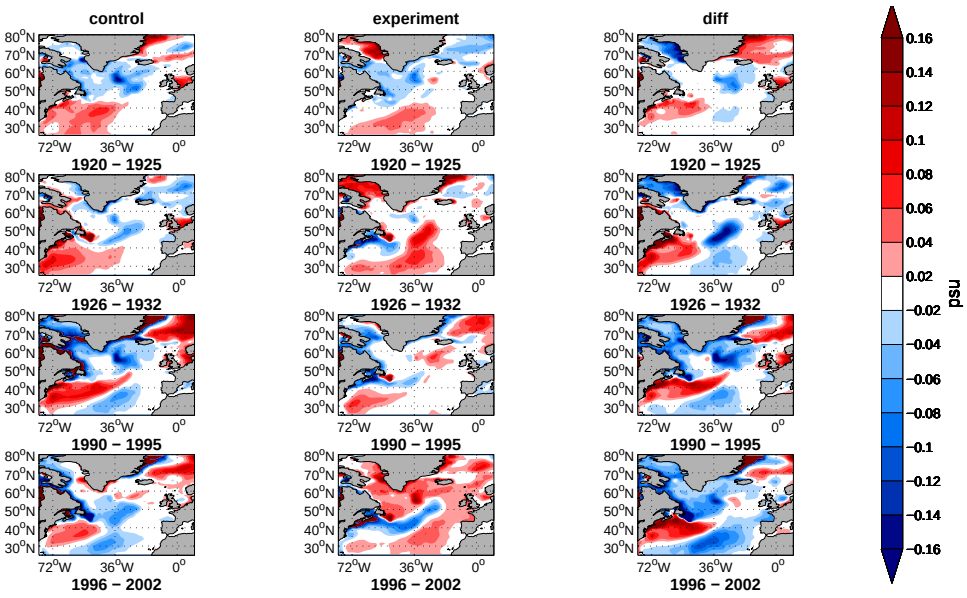

Figure A.2: Same as Figure A.1, but for S500.

Bibliography

Alheit, J., Licandro, P., Coombs, S., Garcia, A., Giráldez, A., Santamaría, M. T. G., Slotte, A. and Tsikliras, A. C. (2014), 'Reprint of "Atlantic Multidecadal Oscillation (AMO) modulates dynamics of small pelagic fishes and ecosystem regime shifts in the eastern North and Central Atlantic"', *Journal of Marine Systems* **133**, 88–102.

Andresen, C. S., Straneo, F., Ribergaard, M. H., Bjørk, A. A., Andersen, T. J., Kuijpers, A., Nørgaard-Pedersen, N., Kjær, K. H., Schjøth, F., Weckström, K. et al. (2012), 'Rapid response of Helheim Glacier in Greenland to climate variability over the past century', *Nature Geoscience* **5**(1), 37–41.

Antonov, J. I., Seidov, D., Boyer, T. P., Locarnini, R. A., Mishonov, A. V., Garcia, H. E., Baranova, O. K., Zweng, M. M. and Johnson, D. R. (2010), 'World Ocean Atlas 2009, Volume 2: Salinity', *NOAA Atlas NESDIS* **69**, 184.

Antonov, J., Levitus, S., Boyer, T., Conkright, M., O'Brien, T. and Stephens, C. (1998), 'World Ocean Atlas 1998, Volume 1: Temperature of the Atlantic Ocean', *NOAA Atlas NESDIS* **27**, 166.

Assmann, K., Bentsen, M., Segschneider, J. and Heinze, C. (2010), 'An isopycnic ocean carbon cycle model', *Geosci. Model Dev* **3**(1), 143–167.

Balmaseda, M. A., Smith, G. C., Haines, K., Anderson, D., Palmer, T. N. and Vidard, A. (2007), 'Historical reconstruction of the Atlantic Meridional Overturning Circulation from the ECMWF operational ocean reanalysis', *Geophysical Research Letters* **34**(23).

Barrier, N., Cassou, C., Deshayes, J. and Treguier, A.-M. (2013), 'Response of North Atlantic Ocean Circulation to Atmospheric Weather Regimes', *Journal of Physical Oceanography* **44**(1), 179–201.

Bellucci, A., Gualdi, S., Scoccimarro, E. and Navarra, A. (2008), 'NAO–ocean circulation interactions in a coupled general circulation model', *Climate dynamics* **31**(7-8), 759–777.

Bengtsson, L., Semenov, V. A. and Johannessen, O. M. (2004), 'The early twentieth-century warming in the Arctic-A possible mechanism', *Journal of Climate* **17**(20), 4045–4057.

Bentsen, M., Bethke, I., Debernard, J., Iversen, T., Kirkevåg, A., Seland, Ø., Drange, H., Roelandt, C., Seierstad, I., Hoose, C. et al. (2013), 'The Norwegian Earth System Model, NorESM1-M-Part 1: Description and basic

evaluation of the physical climate', *Geoscientific Model Development* **6**, 687–720.

Bentsen, M., Drange, H., Furevik, T. and Zhou, T. (2004), 'Simulated variability of the Atlantic meridional overturning circulation', *Climate Dynamics* **22**(6-7), 701–720.

Bleck, R., Rooth, C., Hu, D. and Smith, L. T. (1992), 'Salinity-driven thermocline transients in a wind-and thermohaline-forced isopycnic coordinate model of the North Atlantic', *Journal of Physical Oceanography* **22**(12), 1486–1505.

Boyer, T., Levitus, S., Antonov, J., Conkright, M., OBrien, T. and Stephens (1998), 'Salinity of the Atlantic Ocean. Volume 4, World Ocean Atlas 1998', *NOAA Atlas NESDIS* **30**, 166.

Brauch, J. P. and Gerdes, R. (2005), 'Response of the northern North Atlantic and Arctic oceans to a sudden change of the North Atlantic Oscillation', *Geophys. Res* **110**.

Brönnimann, S., Grant, A. N., Compo, G. P., Ewen, T., Griesser, T., Fischer, A. M., Schraner, M. and Stickler, A. (2012), 'A multi-data set comparison of the vertical structure of temperature variability and change over the Arctic during the past 100 years', *Climate dynamics* **39**(7-8), 1577–1598.

Brown, E., Colling, A., Park, D., Phillips, J., Rothery, D. and Wright, J. (2001), *Ocean circulation*, Vol. 3, Butterworth-Heinemann.

Chassignet, E. P., Smith, L. T., Bleck, R. and Bryan, F. O. (1996), 'A model comparison: numerical simulations of the north and equatorial Atlantic oceanic circulation in depth and isopycnic coordinates', *Journal of Physical Oceanography* **26**(9), 1849–1867.

Cheng, W., Chiang, J. C. and Zhang, D. (2013), 'Atlantic meridional overturning circulation (AMOC) in CMIP5 models: RCP and historical simulations', *Journal of Climate* **26**(18), 7187–7197.

Climate Data Guide; A. Phillips (2014), 'The climate data guide: Hurrell north atlantic oscillation (nao) index (pc-based)'.
URL: *https://climatedataguide.ucar.edu/climate-data/hurrell-north-atlantic-oscillation-nao-index-pc-basedl*

Compo, G. P., Whitaker, J. S., Sardeshmukh, P. D., Matsui, N., Allan, R., Yin, X., Gleason, B., Vose, R., Rutledge, G., Bessemoulin, P. et al. (2011), 'The twentieth century reanalysis project', *Quarterly Journal of the Royal Meteorological Society* **137**(654), 1–28.

Cunningham, S. A., Kanzow, T., Rayner, D., Baringer, M. O., Johns, W. E., Marotzke, J., Longworth, H. R., Grant, E. M., Hirschi, J. J.-M., Beal, L. M. et al. (2007), 'Temporal variability of the Atlantic meridional overturning circulation at 26.5 N', *science* **317**(5840), 935–938.

Curry, R. G. and McCartney, M. S. (2001), 'Ocean Gyre Circulation Changes Associated with the North Atlantic Oscillation*', *Journal of Physical Oceanography* **31**(12), 3374–3400.

Danabasoglu, G., Yeager, S. G., Bailey, D., Behrens, E., Bentsen, M., Bi, D., Biastoch, A., Böning, C., Bozec, A., Canuto, V. M. et al. (2014*a*), 'North Atlantic simulations in coordinated ocean-ice reference experiments phase ii (CORE-II). Part I: Mean states', *Ocean Modelling* **73**, 76–107.

Danabasoglu, G., Yeager, S. G., Bailey, D., Behrens, E., Bentsen, M., Bi, D., Biastoch, A., Böning, C., Bozec, A., Canuto, V. M. et al. (2014*b*), 'North Atlantic simulations in coordinated ocean-ice reference experiments phase ii (CORE-II). Part I: Mean states', *Ocean Modelling* **73**, 76–107.

Deser, C., Alexander, M. A., Xie, S.-P. and Phillips, A. S. (2010), 'Sea surface temperature variability: Patterns and mechanisms', *Annual Review of Marine Science* **2**, 115–143.

Drinkwater, K. F. (2006), 'The regime shift of the 1920s and 1930s in the North Atlantic', *Progress in Oceanography* **68**(2), 134–151.

Eden, C. and Willebrand, J. (2001), 'Mechanism of interannual to decadal variability of the North Atlantic circulation', *Journal of Climate* **14**(10), 2266–2280.

Emery, W. J. and Thomson, R. E. (2001), *Data Analysis Methods in Physical Oceanography*, Elsevier.
URL: *http://books.google.no/books?id=gYc4fp_ixmwC*

Fu, C., Diaz, H. F., Dong, D. and Fletcher, J. O. (1999), 'Changes in atmospheric circulation over Northern Hemisphere oceans associated with the rapid warming of the 1920s', *International Journal of Climatology* **19**(6), 581–606.

Gao, Y. and Yu, L. (2008), 'Subpolar gyre index and the North Atlantic meridional overturning circulation in a coupled climate model'.

Glessmer, M. S., Eldevik, T., Våge, K., Nilsen, J. E. Ø. and Behrens, E. (2014), 'Atlantic origin of observed and modelled freshwater anomalies in the Nordic Seas', *Nature Geoscience* .

Gottlieb, S., Jung, J.-H. and Kim, S. (2011), 'A review of David Gottlieb's work on the resolution of the Gibbs phenomenon', *Commun. Comput. Phys* **9**(3), 497–519.

Greatbatch, R. J. (2000), 'The North Atlantic Oscillation', *Stochastic Environmental Research and Risk Assessment* **14**(4-5), 213–242.

Griffies, S. M., Biastoch, A., Böning, C., Bryan, F., Danabasoglu, G., Chassignet, E. P., England, M. H., Gerdes, R., Haak, H., Hallberg, R. W. et al. (2009), 'Coordinated ocean-ice reference experiments (COREs)', *Ocean Modelling* **26**(1), 1–46.

Häkkinen, S. and Rhines, P. B. (2004), 'Decline of subpolar North Atlantic circulation during the 1990s', *Science* **304**(5670), 555–559.

Häkkinen, S., Rhines, P. B. and Worthen, D. L. (2011), 'Warm and saline events embedded in the meridional circulation of the northern North Atlantic', *Journal of Geophysical Research: Oceans (1978–2012)* **116**(C3).

Hanna, E., Cappelen, J., Fettweis, X., Huybrechts, P., Luckman, A. and Ribergaard, M. (2009), 'Hydrologic response of the Greenland ice sheet: the role of oceanographic warming', *Hydrological Processes* **23**(1), 7–30.

Hannachi, A. (2004), 'A primer for EOF analysis of climate data', *Departement of Meteorology, University of Reading. UK* .

Hátún, H., Sandø, A. B., Drange, H., Hansen, B. and Valdimarsson, H. (2005), 'Influence of the Atlantic subpolar gyre on the thermohaline circulation', *Science* **309**(5742), 1841–1844.

Herbaut, C. and Houssais, M.-N. (2009), 'Response of the eastern North Atlantic subpolar gyre to the North Atlantic Oscillation', *Geophysical Research Letters* **36**(17).

Holland, D. M., Thomas, R. H., De Young, B., Ribergaard, M. H. and Lyberth, B. (2008), 'Acceleration of Jakobshavn Isbrae triggered by warm subsurface ocean waters', *Nature Geoscience* **1**(10), 659–664.

Holland, M. M., Bailey, D. A., Briegleb, B. P., Light, B. and Hunke, E. (2012), 'Improved sea ice shortwave radiation physics in CCSM4: the impact of melt ponds and aerosols on Arctic sea ice*', *Journal of Climate* **25**(5), 1413–1430.

Hunke, E. and Lipscomb, W. (2008), CICE: The Los Alamos Sea Ice Model, documentation and software, version 4.0, Tech. Rep., Technical Report LA-CC-06-012, Los Alamos National Laboratory, Los Alamos, New Mexico, USA.

Hurrell, J. W. (1995), 'Decadal Trends in the North Atlantic Oscillation: Regional Temperatures and Precipitation', *Science* **269**(5224), 676–679.
URL: *http://www.sciencemag.org/content/269/5224/676.abstract*

Hurrell, J. W. (1996), 'Influence of variations in extratropical wintertime teleconnections on northern hemisphere temperature', *Geophysical Research Letters* **23**(6), 665–668.
URL: *http://dx.doi.org/10.1029/96GL00459*

Iversen, T., Bentsen, M., Bethke, I., Debernard, J., Kirkevåg, A., Seland, Ø., Drange, H., Kristjansson, J., Medhaug, I., Sand, M. et al. (2013), 'The Norwegian Earth System Model, NorESM1-M-Part 2: Climate response and scenario projections', *Geoscientific Model Development* **6**, 389–415.

Levitus, S., Antonov, J. I., Boyer, T. P. and Stephens, C. (2000), 'Warming of the world ocean', *Science* **287**(5461), 2225–2229.

Locarnini, R. A., Mishonov, A. V., Antonov, J. I., Boyer, T. P., Garcia, H. E., Baranova, O. K., Zweng, M. M., and Johnson, D. R. (2010), 'World Ocean Atlas 2009, Volume 1: Temperature', *NOAA Atlas NESDIS* **68**, 184.

Lohmann, K., Drange, H. and Bentsen, M. (2008), 'Response of the North Atlantic subpolar gyre to persistent North Atlantic oscillation like forcing', *Climate dynamics* **32**(2-3), 273–285.

Lohmann, K., Drange, H. and Bentsen, M. (2009), 'A possible mechanism for the strong weakening of the North Atlantic subpolar gyre in the mid-1990s', *Geophysical Research Letters* **36**(15).

Lorbacher, K., Dengg, J., Böning, C. W. and Biastoch, A. (2010), 'Regional Patterns of Sea Level Change Related to Interannual Variability and Multidecadal Trends in the Atlantic Meridional Overturning Circulation*', *Journal of Climate* **23**(15), 4243–4254.

Lu, Y., Wright, D. G. and Yashayaev, I. (2007), 'Modelling hydrographic changes in the Labrador sea over the past five decades ', *Progress in Oceanography* **73**(3–4), 406 – 426. Observing and Modelling Ocean Heat and Freshwater Budgets and Transports.
URL: *http://www.sciencedirect.com/science/article/pii/S0079661107000808*

Lynn, R. J. (1971), 'On potential density in the deep South Atlantic Ocean', *Journal of Marine Research* **29**(2), 171–7.

Marshall, J. and Plumb, R. A. (2008), *Atmosphere, ocean and climate dynamics: an introductory text*, Vol. 93, Elsevier Academic Press.

Marzeion, B., Levermann, A. and Mignot, J. (2010), 'Sensitivity of North Atlantic subpolar gyre and overturning to stratification-dependent mixing: response to global warming', *Climate dynamics* **34**(5), 661–668.

Mendenhall, W., Beaver, R. and Beaver, B. (2012), *Introduction to probability and statistics*, Cengage Learning.

Müller, W. A., Matei, D., Bersch, M., Jungclaus, J. H., Haak, H., Lohmann, K., Compo, G. P., Sardeshmukh, P. D. and Marotzke, J. (2014), 'A twentieth-century reanalysis forced ocean model to reconstruct the North Atlantic climate variation during the 1920s', *Climate Dynamics* pp. 1–21.
URL: *http://dx.doi.org/10.1007/s00382-014-2267-5*

Olsen, S. M., Hansen, B., Quadfasel, D. and Østerhus, S. (2008), 'Observed and modelled stability of overflow across the Greenland–Scotland ridge', *Nature* **455**(7212), 519–522.

Polyakov, I., Bhatt, U., Simmons, H., Walsh, D., Walsh, J. and Zhang, X. (2005), 'Multidecadal variability of North Atlantic temperature and salinity during the twentieth century', *Journal of Climate* **18**(21), 4562–4581.

Ribergaard, M. H. (2013), 'Oceanographic Investigations off West Greenland 2012', *NAFO Scientific Council Documents, 13/003* .

Robson, J., Sutton, R., Lohmann, K., Smith, D. and Palmer, M. D. (2012), 'Causes of the rapid warming of the North Atlantic Ocean in the mid-1990s', *Journal of Climate* **25**(12), 4116–4134.

Roeckner, E. and Arpe, K. (1996), 'Coauthors, 1996: The atmospheric general circulation model ECHAM-4: Model description and simulation of present-day climate', *Max-Planck-Institut für Meteorologie Rep* **218**, 90.

Rogers, J. C. (1985), 'Atmospheric circulation changes associated with the warming over the northern North Atlantic in the 1920s', *Journal of Climate and Applied Meteorology* **24**(12), 1303–1310.

Rogers, J. C. (1990), 'Patterns of low-frequency monthly sea level pressure variability (1899-1986) and associated wave cyclone frequencies', *Journal of Climate* **3**(12), 1364–1379.

Schiller, A. and Brassington, G. (2011), *Operational Oceanography in the 21st Century*, Springer.
URL: *http://books.google.no/books?id=rcjbUaNi4HIC*

Schmittner, A., Chiang, J. and Hemming, S. R. (2007), 'Introduction: The ocean's meridional overturning circulation', *Geophysical Monograph Series* **173**, 1–4.

Shampine, L. F. (2009), 'Stability of the leapfrog/midpoint method', *Applied Mathematics and Computation* **208**(1), 293–298.

Simmons, A., Wallace, J. and Branstator, G. (1983), 'Barotropic wave propagation and instability, and atmospheric teleconnection patterns', *Journal of the Atmospheric Sciences* **40**(6), 1363–1392.

Smed, J. (1978), 'Fluctuations in the temperature of the surface water in areas of the northern North Atlantic, 1876 to 1975', *On Climate Changes and Related Probl. (SEE N 80-27009 17-47)* pp. 205–210.

Smith, S. W. et al. (1997), 'The scientist and engineer's guide to digital signal processing'.

Steele, M., Morley, R. and Ermold, W. (2001), 'PHC: A global ocean hydrography with a high-quality Arctic Ocean', *Journal of Climate* **14**(9), 2079–2087.

Stewart, R. H. (2004), *Introduction to physical oceanography*, Texas A & M University.

Stommel, H. (1948), 'The westward intensification of wind-driven ocean currents', *Trans. Amer. Geophys. Union* **29**(2), 202–206.

Sundby, S. and Drinkwater, K. (2007), 'On the mechanisms behind salinity anomaly signals of the northern North Atlantic', *Progress in Oceanography* **73**(2), 190–202.

Talley, L. D., Pickard, G. L., Emery, W. J. and Swift, J. H. (2011), *Descriptive physical oceanography: an introduction*, Academic Press.

Taylor, A. H. and Stephens, J. A. (1998), 'The North Atlantic Oscillation and the latitude of the Gulf Stream', *Tellus A* **50**(1), 134–142.
URL: *http://dx.doi.org/10.1034/j.1600-0870.1998.00010.x*

Thompson, D. W. J. and Wallace, J. M. (1998), 'The Arctic oscillation signature in the wintertime geopotential height and temperature fields', *Geophysical Research Letters* **25**(9), 1297–1300.
URL: *http://dx.doi.org/10.1029/98GL00950*

Tomczak, M. and Godfrey, J. S. (2001), *Regional Oceanography, an Introduction (PDF version 1)*.
URL: *http://www.es.flinders.edu.au/ mattom/regoc/pdffiles/colour/single/04P-Ekman.pdf*

Tréguier, A.-M., Theetten, S., Chassignet, E. P., Penduff, T., Smith, R., Talley, L., Beismann, J. and Böning, C. (2005), 'The North Atlantic subpolar gyre in four high-resolution models', *Journal of Physical Oceanography* **35**(5), 757–774.

Visbeck, M., Chassignet, E. P., Curry, R. G., Delworth, T. L., Dickson, R. R. and Krahmann, G. (2003), 'The ocean's response to North Atlantic Oscillation variability', *The North Atlantic Oscillation: climatic significance and environmental impact* pp. 113–145.

Walker, G. (1924), *Correlation in Seasonal Variations of Weather, IX: Further Study of World-weather*, Memoirs of the India Meteorological Department, Meteorological Office.
URL: *http://books.google.no/books?id=jqgXNQAACAAJ*

Walker, G. T. and Bliss, E. (1932), 'World weather', *V. Mem. Roy. Meteor. Soc.* **4**, 53–84.

Woodruff, S. D., Slutz, R. J., Jenne, R. L. and Steurer, P. M. (1987), 'A comprehensive ocean-atmosphere data set', *Bulletin of the American meteorological society* **68**(10), 1239–1250.

Yanchun, H., Yongqi, G., Drange, H. and Bentsen, M. (2014), 'Simulated Atlantic Meridional Overturning Circulation in the 20th century with ocean model forced by reanalysis-based atmospheric dataset'. Unpublished.

Yashayaev, I. and Clarke, A. (2008), ' Evolution of North Atlantic water masses inferred from Labrador Sea salinity series.', *Oceanography* **21**.

Yeager, S. and Danabasoglu, G. (2014), 'The Origins of Late-Twentieth-Century Variations in the Large-Scale North Atlantic Circulation', *Journal of Climate* **27**(9), 3222–3247.

Zhang, R., Delworth, T. L. and Held, I. M. (2007), 'Can the Atlantic Ocean drive the observed multidecadal variability in Northern Hemisphere mean temperature?', *Geophysical Research Letters* **34**(2).